

## Old-Aged Stellar Population Distance Indicators

Rachael L. Beaton, Giuseppe Bono, Vittorio  
Francesco Braga, Massimo Dall'Ora,  
Giuliana Fiorentino, In Sung Jang, Clara E.  
Martínez-Vázquez, Noriyuki Matsunaga,  
Matteo Monelli, Jillian R. Neeley, and  
Maurizio Salaris

the date of receipt and acceptance should be inserted later

**Abstract** Old-aged stellar distance indicators are present in all Galactic structures (halo, bulge, disk) and in galaxies of all Hubble types and, thus, are immensely

---

Rachael L. Beaton  
Hubble Fellow

Department of Astrophysical Sciences, Princeton University, 4 Ivy Lane, Princeton, NJ 08544,  
The Observatories of the Carnegie Institution for Science, 813 Santa Barbara Street, Pasadena  
CA 91101, E-mail: rbeaton@princeton.edu

Giuseppe Bono  
Department of Physics, University of Rome Tor Vergata  
INAF-Osservatorio Astronomico di Roma,

Vittorio Francesco Braga  
Department of Physics, University of Rome Tor Vergata  
ASDC

Massimo Dall'Ora  
INAF-Osservatorio Astronomico di Capdoimonte,

Giuliana Fiorentino  
INAF-Osservatorio di Astrofisica & Scienza dello Spazio di Bologna,

In Sung Jang  
Leibniz-Institut für Astrophysik Potsdam, D-14482 Potsdam, Germany,

Clara E. Martínez-Vázquez  
Cerro Tololo Inter-American Observatory, National Optical Astronomy Observatory, Casilla  
603, La Serena, Chile,

Noriyuki Matsunaga  
Department of Astronomy, School of Science, The University of Tokyo, Japan,

Matteo Monelli  
IAC- Instituto de Astrofísica de Canarias, Calle Vía Lactea s/n, E-38205 La Laguna, Tenerife,  
Spain  
Departamento de Astrofísica, Universidad de La Laguna, E-38206 La Laguna, Tenerife, Spain

Jillian R. Neeley  
Department of Physics, Florida Atlantic University, 777 Glades Rd, Boca Raton, FL 33431

Maurizio Salaris  
Astrophysics Research Institute, Liverpool John Moores University 146 Brownlow Hill, L3 5RF  
Liverpool, UK

---

powerful tools for understanding our Universe. Here we present a comprehensive review for three primary standard candles from Population II: (i) RR Lyrae type variables (RRL), (ii) type II Cepheid variables (T2C), and (iii) the tip of the red giant branch (TRGB). The discovery and use of these distance indicators is placed in historical context before describing their theoretical foundations and demonstrating their observational applications across multiple wavelengths. The methods used to establish the absolute scale for each standard candle is described with a discussion of the observational systematics. We conclude by looking forward to the suite of new observational facilities anticipated over the next decade; these have both a broader wavelength coverage and larger apertures than current facilities. We anticipate future advancements in our theoretical understanding and observational application of these stellar populations as they apply to the Galactic and extragalactic distance scale.

---

**Contents**

1	Introduction . . . . .	4
2	The RR Lyrae variables . . . . .	7
2.1	A physical description of RR Lyrae . . . . .	10
2.2	RR Lyrae as Standard Candles . . . . .	12
2.2.1	The visual magnitude–metallicity relation . . . . .	12
2.2.2	The FOBE method . . . . .	17
2.2.3	The NIR period–luminosity relations . . . . .	18
2.2.4	The RR Lyrae period–luminosity slopes . . . . .	22
2.2.5	Reddening-free relations . . . . .	24
2.3	Case studies using RR Lyrae . . . . .	25
2.3.1	An optical study of RR Lyrae in Sculptor . . . . .	25
2.3.2	A near-IR study of the RRLs in M4 . . . . .	28
2.3.3	A MIR study of RR Lyrae in M4 . . . . .	31
2.4	Summary . . . . .	34
3	The type II Cepheids . . . . .	35
3.1	Overview . . . . .	35
3.2	Observed pulsational properties . . . . .	36
3.3	Theoretical pulsation predictions . . . . .	37
3.4	Optical and near-IR period–luminosity and period–Wesenheit relations . . . . .	41
3.5	T2Cs in context with RRLs and CCs . . . . .	46
3.6	Summary and final remarks . . . . .	49
4	The Tip of the Red Giant Branch . . . . .	50
4.1	Physical Description . . . . .	51
4.2	Detecting the TRGB . . . . .	54
4.2.1	Edge-Detection Techniques . . . . .	56
4.2.2	Techniques to “Sharpen” the Tip Edge . . . . .	59
4.2.3	Contamination to the LF . . . . .	61
4.3	Case Study for the Optical TRGB . . . . .	62
4.4	Developments for the IR-TRGB as a Distance Indicator . . . . .	64
4.5	Summary . . . . .	67
5	Systematics and the Absolute Scale . . . . .	68
5.1	Comparison Case Study in IC1613 . . . . .	68
5.2	Absolute Scale through Primary Calibration Techniques . . . . .	71
5.2.1	The Methods . . . . .	71
5.2.2	Primary Calibration of the RRLs . . . . .	72
5.2.3	Primary Calibration of the T2Cs . . . . .	74
5.2.4	Primary Calibration of the TRGB . . . . .	75
5.3	The Absolute Scale via Secondary Calibration . . . . .	76
5.3.1	Methods for Secondary Calibration . . . . .	76
5.3.2	Secondary Calibration of the RRLs . . . . .	78
5.3.3	Secondary Calibration of the T2C . . . . .	78
5.3.4	Secondary Calibration of the TRGB . . . . .	78
5.4	Metallicity . . . . .	79
5.4.1	Metallicity Impacts in RRL: . . . . .	80
5.4.2	Metallicity Impacts in T2Cs: . . . . .	81
5.4.3	Metallicity Impacts in TRGB: . . . . .	81
5.5	Other Systematics . . . . .	82
6	Summary and Future Prospects . . . . .	83

## 1 Introduction

Standard candles drawn from old stellar populations have a significant advantage for distance scale as, with the exception of young Galactic star clusters, old stellar populations are found in every galactic structural component (disk, halo, bulge), galaxies of all Hubble types, and galaxies of all luminosities (from ultra-faint to ultra-luminous). Most importantly, from these distance indicators it is possible to map both Galactic and extra-galactic objects using tracers pulled from the same underlying stellar population, if not the same class of star. Moreover, due to the presence of old stars in most structural components of galaxies, it is possible to study nearby galaxies in three dimensions (e.g., measuring depths, orientations, etc.) and then to evaluate if there systematics in mean distances due to these complex structures (see e.g., Kunder et al, 2018). In turn, this helps us to better understand how projection effects and line-of-sight depth could bias mean distances. Thus, by virtue of being “old” standard candles have immense potential.

The goal of this chapter is to provide a comprehensive review for the primary standard candles drawn from Population II stars. The term Population II (Pop II) is an old one that originated from Baade (1944) in which the nebulous central regions of the Andromeda, M32, and NGC 205 were first resolved into individual stars. Baade (1944) realized that these stars more closely resembled those in Galactic globular clusters (GGCs) than the “slow moving” stars in the solar neighborhood (e.g., disk stars). Later work would frame the differences as a function of age and metallicity, as Baade (1958a) concisely summarized at the Vatican conference. Interestingly, the nature of the variable stars and their proper classification into Pop I or Pop II was intimately entwined (Baade, 1958b). We focus our attention in this chapter to relatively luminous tracers that can be used for a broad range of distances and can be considered “primary”, in that there exist some absolute calibrations using parallaxes for these standard candles from before the onset of progressive *Gaia* data releases (DR1 and DR2 at the time of writing). These considerations result in three distance indicators: (i) the RR Lyrae (RRL), (ii) the Type II Cepheids (T2C), and (iii) the tip of the red giant branch (TRGB) stars. The basic properties of these standard candles are given in Table 1.

Both the RRL and the T2C are pulsational variables that occur when specific Pop II sequences cross the classical instability strip and these stars adhere to specific period–luminosity (PL) relationships from which distances can be determined to individual stars. In contrast, the stars that comprise TRGB are non-variable in nature<sup>1</sup> and as a result, the distance measurement is performed using a population of stars, which makes it statistical in nature.

Figures 1a and 1b show the relative positions of the Classical Cepheids (blue), RRLs (green), T2Cs (red), and TRGB (orange arrow) for the Large and Small Magellanic Clouds (LMC, SMC) using variable star identifications from OGLE-III<sup>2</sup> (Soszyński et al, 2008, 2015, 2016b) overplotted on a color magnitude density diagram from Magellanic Clouds Photometric Survey<sup>3</sup> (greyscale Zaritsky et al, 2002, 2004). Figures 1a and 1b keenly demonstrate how the T2Cs could have been

<sup>1</sup> These stars likely have some intrinsic variability – as most stars do, but it is on a much smaller scale than the pulsational variables that have amplitudes  $\sim 0.3$  to  $>1$  mag.

<sup>2</sup> The full variable star catalog can be queried here: <http://ogledb.astrouw.edu.pl/~ogle/OCVS/>

<sup>3</sup> Data is available here: <http://djuma.as.arizona.edu/~dennis/mcsurvey/>



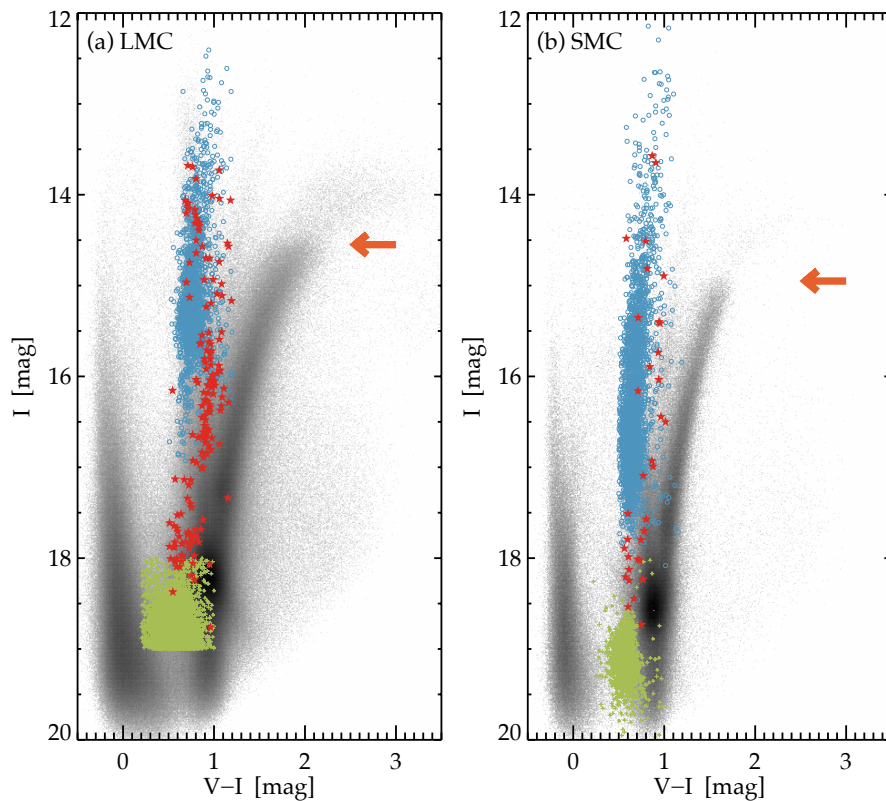


**Fig. 1** Optical color magnitude diagrams for the (a) LMC and (b) SMC from the Magellanic Clouds Photometric Survey (black; MCPS Zaritsky et al, 2002, 2004) with variable star identifications from OGLE-III as follows RRLs (green pluses), T2Cs (red five-pointed stars), and the Classical Cepheids (blue open circles) over plotted (Soszyński et al, 2016b, 2008, 2015, respectively). The approximate location of the TRGB is indicated with a thick orange arrow. The axes for both panels are identical for ease of comparison. **We note that no corrections for extinction (Galactic or internal to the LMC) have been applied and, thus, the color widths of the populations may be broader, to the red, than their intrinsic range.**

confused with the Classical Cepheids, as the two populations overlap in magnitude. The three sub-classifications for the T2Cs are also visible by the distinct clumps in the LMC (Figure 1a) with these distinctions being less clear in the lower-metallicity SMC (Figure 1b). The difference in the population size for the three variable star classes is also apparent, with the T2Cs being less abundant than either the Classical Cepheids or the RRLs. Figures 1a and 1b reinforce the mean magnitude differences given in Table 1, with the TRGB being more luminous than the bulk of the T2Cs and the T2Cs being brighter than the RRLs.

As a class, the RRL have a long history in the optical, having been discovered in the 19th century in cluster diagrams, but recognition of their great potential in the infrared has come only recently (most notably, Longmore et al, 1986). The short period of RRLs make identifying them relatively simple with observations spanning only a few nights and with numerous Globular Clusters being sufficiently

**Table 1** Basic Properties of Population II Distance Indicators.

Star	Sub-Type	$M_V$ [mag]	$M_K$ [mag]	$P$ [days]
RR LYRAE (RRL)				
	Fundamental Mode (RRab)	$\sim +0.6$	$\sim -0.6$	$0.3 < P < 1.0$
	First Overtone Mode (RRc)	$\sim +0.6$	$\sim -0.4$	$0.2 < P < 0.5$
TYPE II CEPHEIDS (T2C)				
	BL Herulis (BL Her)	$\sim -0.5$	$\sim -1.0$	$1 < P < 4$
	W Virginis (W Vir)	$\sim -1.0$	$\sim -4.0$	$4 < P < 20$
	RV Tauri (RV Tau)	$\sim -2.5$	$\sim -5.0$	$20 < P < 80$
TIP OF THE RED GIANT BRANCH STARS (TRGB)				
	Metal-Poor	$\sim -4.0$	$\sim -5.5$	
	Metal-Rich	$\sim -3.9$	$\sim -6.5$	

nearby for them to have been readily discovered by early photometric monitoring campaigns (a detailed history is given in Smith, 1995). In contrast, the T2Cs were only separated from the classical Cepheids in 1956 by Baade and, despite being a solution to a difficulty in reconciling  $H_0$  from the distance ladder and cosmological theory, have received little attention until the long-term monitoring from the OGLE project unveiled them *en masse* in the LMC (Figure 1a, Soszyński et al, 2008). The recognition of the TRGB as a luminosity indicator came later still when the work of Da Costa and Armandroff (1990) provided high quality homogeneous photometry for a number of Galactic globular clusters (GGCs) transformed into absolute units by their RRL distances. The TRGB was first used to determine distances for galaxies by Lee et al (1993), who developed the analysis techniques necessary to detect the tip from color-magnitude diagrams.

Each of these distance indicators, thus, has a different volume of literature accompanying them and, as a result, have different depths of both theoretical understanding and observational applications. Often these vary not only by distance indicator, but also by wavelength regimes and objects (field stars, star clusters, galaxies) in which the techniques have been employed. Thus, the depth and breadth of information provided in this review varies for each distance indicator.

Generally, a single book chapter cannot fully describe any one of these standard candles. Thus, we refer the reader to more detailed discussions that are in the literature. Of particular note are the following books: Smith (1995) on RRLs and Catelan and Smith (2015) on pulsational variables of all kinds, including both RRLs and T2Cs. Additionally, McWilliam (2011) is a set of online conference articles that present reviews of many aspects of RRL beyond those that will be discussed here, as well as other discussions relating to metal-poor, old stellar populations. Salaris and Cassisi (2005) is an excellent resource on stellar evolution and stellar populations that provides insight into all three of our distance indicators, but most especially the TRGB. Lastly, Beaton et al (2016) provides comparison of RRL and TRGB methods with Cepheids in terms of the extragalactic distance scale that may help the reader understand the recent resurgence of interest Pop II standard candles.

Our goal in this chapter is to place these Population II standard candles into the context of the distance scale by providing a sense of the current theoretical understanding and observational application of these tools. Where possible, we take a multi-wavelength approach discussing optical, near-infrared, and mid-infrared characteristics and applications. In the sections that follow we discuss each of the

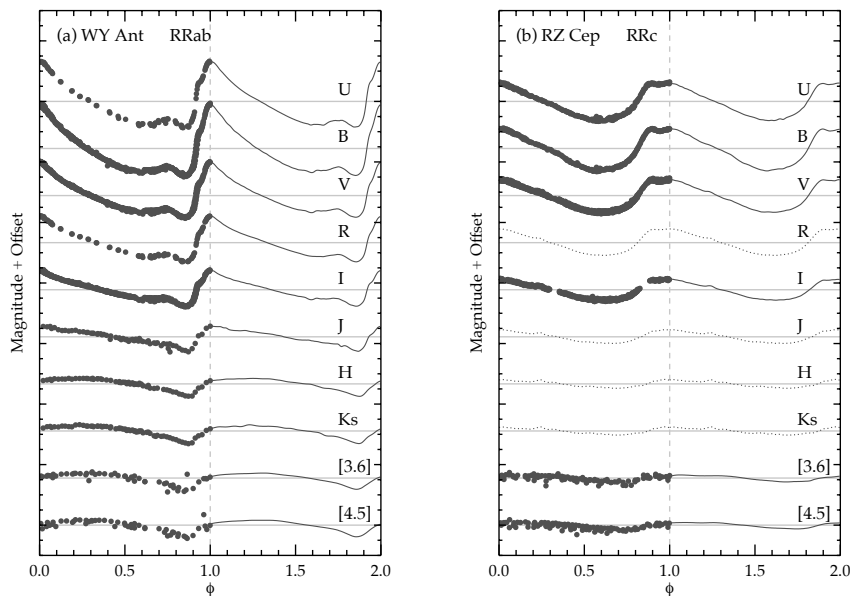


**Fig. 2** (a) Example multi-wavelength light curves for an RRab RRL, WY Ant and (b) Example multi-wavelength light curves for an RRc RRL, RZ Cep (data from Monson et al, 2017). In each panel, the light curves are shown in ten photometric bands, which are from bottom to top  $U$ ,  $B$ ,  $V$ ,  $R$ ,  $I_c$ ,  $J$ ,  $H$ ,  $K$ ,  $[3.6]$ , and  $[4.5]$ . The optical bands are the Johnson-Cousins system, the near-infrared bands are in the 2MASS system, and the mid-infrared bands are in the *Spitzer*-IRAC system; a detailed discussion of the photometry homogenization is given in Monson et al (2017). In addition to the raw data points, a smoothed light curve is shown in black and a template light curve is shown in gray, if no data is present. The horizontal line indicates the mean magnitude and the dashed vertical line indicates maximum light in the optical ( $\phi = 1$ ).

distance indicators in turn, with parallel discussions of theory and practice for the RRL in Section 2, a description and homogeneous PL relations for T2C in Section 3, and both a physical description and application of the TRGB is given in Section 4. The absolute scale for each distance indicator and inter-comparisons are described in Section 5. We conclude in Section 6 with an outlook for the future, in particular improvements to our physical understanding from *Gaia* and the observational application with future large-aperture facilities.

## 2 The RR Lyrae variables

The first variable in a GGC was discovered by Williamina Fleming and reported in Pickering (1889). In 1893, Solon Bailey initiated a large scale program for imaging GGCs from the Harvard College Observatory in Arequipa, Peru with Williamina Fleming serving as his assistant. Very quickly several variables were discovered in the brightest GGCs in the Southern sky, in particular for  $\omega$  Centauri ( $\omega$  Cen). By the end of this project, Bailey had discovered over 500 variables in GGCs, which was equal in number to that found over the entire remainder of the sky!

A more detailed story of the discovery of RRLs is given in the introduction to Smith (1995).<sup>4</sup> RR Lyrae, itself, was discovered by W. Flemming prior to 1899 and reported in Pickering et al (1901).

The observations reported in Bailey (1902) define the nomenclature for RRLs that is used to this day. RRLs come in two primary types; more specifically, those that pulsate in the fundamental mode (FU) known as RRab (a combination of the original Bailey types of a and b) and those that pulsate in the first overtone (FO) known as RRc (the Bailey type c stars). The connection between the modes of pulsation and their Bailey types was first inferred by Schwarzschild (1940) using high quality photometric-plate light curves in the cluster M3; more specifically, Schwarzschild (1940) concluded that the ‘c’ stars needed to pulsate in a different mode to account for the strong deviation of this class from the period-density relation for the ‘a’ and ‘b’ type variables. Schwarzschild (1940) further defined the color-edges of the instability strip concluding that no non-pulsating stars could exist in this temperature-luminosity range. Additionally, there are the RRd type stars that show two pulsation modes and an ensemble of stars discovered from the OGLE program have more complex or atypical pulsation behavior (e.g., Soszyński et al, 2016a, and references therein). The mean magnitudes of the RRL place them on the horizontal branch (HB) of GGCs, whereas at any given epoch, they will scatter above or below based on their amplitudes.

Some RRLs show an amplitude-modulation phenomenon known as the Blazhko effect (first identified in Blažko, 1907) that currently has no consensus for its physical origin, though its impacts on the light curve are well documented. A particularly interesting demonstration of the complexity of the Blazhko phenomenon can be found in Chadid et al (2014, see also references therein) that presents data at very high cadence tracing a single star during Antarctic winter for 150 days. The periods of the Blazhko effect can be from tens to hundreds of pulsation cycles for a given star (see for instance, the study of Skarka, 2014). The effect is well known and studied in the optical, but has recently been shown to persist into the  $K$  band (Jurcsik et al, 2018). The impact of the Blazhko effect on distances is that these stars have more uncertainty with respect to both their periods and mean magnitudes, with the impact being proportional to the level of amplitude-modulation. Thus, these stars, when identified, are not always used for PL fitting.

Bailey et al (1919) paved the road for use of RRLs as both tracers for old stellar population (Pop. II) and as distance indicators. Subsequent investigations demonstrated that the RRL visual mean magnitude, within a given cluster, was nearly constant. The first strong evidence that RRL visual mean magnitude and the metallicity were correlated came in Baade (1958c), in which the populations of variables were compared between disk and halo star clusters and the Galactic Bulge. Additional evidence accumulated over the next few years; in particular, (i) additional probes of the HB magnitude for GGCs with metallicity estimates by Sandage and Wallerstein (1960) and (ii) comparisons between variables found in more environments, in particular the Draco dwarf Spheroidal that showed both similarities and differences to stellar sequences in the GGCs (Baade and Swope,

---

<sup>4</sup> We also refer the reader to Sobel (2016) for a description of the role of Williamina Fleming in these discoveries. More specifically, Williamina Fleming was first E. C. Pickering’s maid, became the first of the Harvard ‘computers,’ and was involved in a large number of projects at the Harvard Observatory. Her accomplishments were honored when she became the first American woman elected to the Royal Astronomical Society.

1961). Since those realizations, RRLs have been commonly used to estimate distances by means of a calibrated  $V$ -band magnitude versus metallicity relation (e.g., Sandage, 1982, and references therein), subsequently rediscussed and calibrated several times, that is still widely used. The mean magnitude of RRLs in the  $V$ -band is nearly constant ( $M_V \sim 0.6$  mag), with a dependence on their chemical composition, thus making RRLs solid standard candles.

Observations of RRLs in a number of GGCs supported the evidence that the topology of the Instability Strip (IS) changes with metallicity. In particular, the first overtone blue edge (FOBE) is virtually independent of the metallicity as originally suggested by linear radiative models (Baker and Kippenhahn, 1965; Cox, 1963; Iben, 1971). This finding and observations brought forward the opportunity to use the FOBE vs period relation as both a reddening and a distance indicator. The theoretical scenario concerning the red edge of the IS was more complex, because it is caused by the increased efficiency of the convective transport when moving toward cooler effective temperatures. Pioneering nonlinear models that included a time dependent treatment of the convective transport (Deupree, 1977b; Stellingwerf, 1982), suggested that the red edge becomes cooler (redder) as the metallicity increases.

The use of RRLs as distance indicators has had a quantum jump thanks to the empirical discovery by Longmore et al (1986) that RRLs obey a linear PL relation at near-infrared wavelengths. This discovery was later soundly supported by nonlinear convective models Bono et al (1994, 2001). More recently, the advent of mid-infrared facilities on board of space telescopes, like *WISE* and *Spitzer*, led to the derivation of empirical PL relations at longer wavelengths (e.g.,  $\lambda \gtrsim$  than  $3.6\mu\text{m}$ ; Section 2.2.3). Another popular diagnostic used to derive distances is the Wesenheit function (van den Bergh, 1975; Madore, 1982), which is a reddening-free formulation of the less common PL-color relations (or PLC), to be discussed in Section 2.2.5.

RRLs are readily recognizable from their light variation. Figure 2 presents an example light curve for each of the two dominant sub-classes of RRL, an RRab (Figure 2a) and an RRC (Figure 2b) in ten photometric broadband filters from Monson et al (2017). Figure 2 illustrates the large amplitudes and unique shapes in the optical for both types of stars, while also demonstrating how the amplitudes decrease strongly as a function of wavelength. Indeed, the amplitude for RZ Cep is 0.1 mag in the IR compared to  $\gtrsim 0.5$  mag in the optical. The RRab stars, in particular, have a “sawtooth” shape in the optical, but become more sinusoidal at longer wavelengths as the impact of the temperature changes become less important. The RRC stars (right), in contrast, have a shape that changes comparatively little as a function of wavelength.

RRLs are nearly ubiquitously present in Local Group galaxies. Indeed, they have been identified in all the stellar systems that host an old ( $\geq 10$  Gyr) stellar component. This evidence makes them excellent probes to investigate the structure and the old stellar populations at the early epochs of galaxy formation. They can be used to trace the components of our Galaxy (bulge, halo, thick disk) and to determine the distance and characterize the old population in Local Group (LG, distances within  $\sim 1$  Mpc) galaxies. Thus, RRLs provide a crucial first step to the extragalactic distance scale for Pop II stellar systems, letting us control possible systematics affecting the commonly used distance scale based on classical Cepheids.

In the following sections, we focus our attention on the theoretical and semi-empirical background for the use of RRLs as distance indicators, with a special attention to some recent developments. Despite great progress in the determination of the RRL PL over the past decade, theoretical PL relations are often used for distance determination due to the lingering uncertainties associated with the absolute zero-point and, in particular, the effect of metallicity. Thus, the sections to follow describing theoretical efforts are quite detailed to motivate the strengths and weaknesses of the theoretical PLs.

## 2.1 A physical description of RR Lyrae

RRLs are radially pulsating low-mass ( $0.6 - 0.8M_{\odot}$ ) stars in their central helium-burning phase. The radial oscillations are an envelope phenomenon that takes place in a well-defined range of effective temperatures, therefore, they populate a relatively narrow region in the Hertzsprung-Russell diagram, which is the intersection between the so called *Cepheid* IS and the HB. We will shortly describe the physical mechanisms driving the radial pulsation and we will analyze with some detail the different approaches to estimate distances using RRLs, highlighting their advantages and disadvantages.

The idea of a pulsating gaseous sphere was developed for the first time by Ritter (1879)<sup>5</sup>, who found a simple relation between pulsation period and mean density, but it was only in Shapley (1914) that the radial pulsation hypothesis was advocated for Cepheid-like stars. The dispute between binarity and radial oscillations was settled in favor of the latter by the so-called Baade-Wesselink method. Radial pulsation is a phenomenon that involves the stellar envelope for certain values of the surface effective temperature ( $T_{eff}$ ) and defines in the color magnitude diagram (CMD) a region in which the stars are unstable to pulsation, the IS. It is worth mentioning that a star radially pulsates only during its crossing(s) of the IS. As a result, the most numerous pulsators are those that have long evolutionary lifetimes within the IS, such as  $\delta$  Scuti (central hydrogen burning) or RR Lyrae and Cepheids (central helium burning).

The physical mechanisms underlying this phenomenon are related to the cyclic variations of the opacity and of the equation of state for regions in which H and He are partially ionized, which are referred to as the  $\kappa$  and  $\gamma$  mechanisms. The physics of radial oscillations was introduced by Eddington (1926) and in the early models by Cox (1958) and Zhevakin (1959). Contrary to what happens in the rest of the envelope, these regions trap energy during the contraction and lose energy during the expansion, thus acting similar to a mechanical valve. The initial perturbation may originate from a stochastic fluctuation in the external layers of the envelope. The mechanical work can either be driven, if the envelope mass located on top of the ionization regions is large enough (below a critical effective temperature that defines the blue edge of the IS) and it can be quenched by the efficiency of convective transport that penetrates deep into the stellar envelope, toward effective temperatures lower than the red edge of the IS.

<sup>5</sup> Several authors also cite Ritter's work from a series of papers published between 1878 and 1883 in Wiedemann's *Annalen* 5-20 that the authors of the present manuscript have been unable to find. Such references begin as early as Shapley (1914) and are cited as recently as Smeyers and van Hoolst (2010).

Simple linear adiabatic models, such as the one developed by Eddington (1918), can predict the pulsation period and the pulsation mode, but they cannot predict the other observables such as the mean magnitudes, amplitudes, shapes of the light curve, and edges of the IS. This implies that non-adiabatic effects have to be considered to properly model the growth of the pulsational instability and the blue edge of the IS (Baker and Kippenhahn, 1965; Cox, 1963; Iben, 1971). The other fundamental pulsation observables, such as the pulsation amplitudes, the morphology of the light curves, and the topology of the instability strip (modal stability), can only be predicted with accuracy with the inclusion of non-linear terms in the hydrodynamical equations (Christy, 1966; Stellingwerf, 1974) and by taking into account the coupling between pulsation and convection (Stellingwerf, 1982, 1983; Feuchtinger et al, 1993).

Current state-of-the-art models adopt a non-linear, time dependent formalism, which also takes into account the effects of convection and its non-linear coupling with the pulsation (e.g., Bono and Stellingwerf, 1994; Bono et al, 1997b; Marconi et al, 2003; Di Criscienzo et al, 2004; Szabó et al, 2004; Marconi et al, 2015). These models assume a spherical envelope (with no rotation or magnetic fields) and then solve the hydrodynamical equations; these are the conservation of mass and momentum plus a treatment for the radiative transfer that includes convection. These equations are solved as a function of time until they approach the limit cycle stability. Although this is one of the most comprehensive approaches, we need to highlight that there is still room for improvement. In particular, the treatment of the convective transfer is non-local and time dependent. Despite this limitation, these models can account for all the observables, including the red boundary of the IS. Moreover, they appear capable of explaining more complicated observables including the double-mode pulsators and the Blazhko effect (Szabó et al, 2014).

For the sake of the subsequent discussion, we note that van Albada and Baker (1971) formalized the relation between the pulsation periods and the structural parameters of mass ( $M$ ), luminosity ( $L$ ), effective temperature ( $T_{eff}$ ), to which Marconi et al (2015) adds composition ( $Z$ ). The relations take the following form:

$$\log P = \mathfrak{F}\{\log(M/M_{\odot}), \log(L/L_{\odot}), \log T_{eff}, \log Z\}. \quad (1)$$

The most recent physical pulsation relations are given in Marconi et al (2015) and are as follows:

$$\begin{aligned} \log P_F = & 11.347(\pm 0.006) + 0.860(\pm 0.003) \log\left(\frac{L}{L_{\odot}}\right) - 0.58(\pm 0.02) \log\left(\frac{M}{M_{\odot}}\right) \\ & - 3.43(\pm 0.01) \log T_{eff} + 0.024(\pm 0.002) \log Z \quad (2) \end{aligned}$$

$$\begin{aligned} \log P_{FO} = & 11.167(\pm 0.006) + 0.822(\pm 0.004) \log\left(\frac{L}{L_{\odot}}\right) - 0.56(\pm 0.02) \log\left(\frac{M}{M_{\odot}}\right) \\ & - 3.40(\pm 0.03) \log T_{eff} + 0.013(\pm 0.002) \log Z \quad (3) \end{aligned}$$

for FU (Equation 2) and FO pulsators (Equation 3), respectively. These physical relations are the basis for all the theoretically-determined pulsation relations (e.g.,

those projected into observable quantities), which are discussed in the following subsections.

We conclude here highlighting that recent theoretical investigations (e.g., Marconi et al, 2011, 2016) have shown that the pulsation properties of RRLs are also affected by the helium content. The Helium abundance impacts RRL evolutionary properties, like the total bolometric luminosity and the evolutionary timescales, which in turn impact the pulsation properties and the the interpretation of observed quantities. Figure 3 shows theoretical HB models in color-magnitude space from “a Bag of Stellar Tracks and Isochrones” (BaSTI) (most recently, Pietrinferni et al, 2004, with earlier works referenced therein)<sup>6</sup> for a fixed total metal content ( $Z = 0.001$ ), but with different Helium contents of  $Y = 0.24$  (solid hashing),  $Y = 0.30$  (dotted hashing), and  $Y = 0.40$  (dashed hashing). The First Overtone Blue Edge (FOBE) is shown for reference. From Figure 3, the impact on the mean absolute magnitude ( $M_V$ ) is demonstrated, with those stars having greater Helium enrichment being systematically brighter and having a slightly different temperature distribution. Beyond this, at fixed metal abundance, the pulsation period is expected to increase and the pulsation amplitude to decrease as the helium abundance increases. The width of the IS, however, is minimally affected.

## 2.2 RR Lyrae as Standard Candles

This subsection focuses on the origin of various relationships that can be used to determine distances using RRL. First, optical relationships are explored, these being (i) the  $M_V$ -Metallicity relationship is explained in Section 2.2.1 and (ii) the FOBE method in Section 2.2.2. Then the, relatively new, NIR and MIR relationships are explained in Section 2.2.3. The multi-wavelength slopes are explored in Section 2.2.4. Lastly, reddening-free relationships constructed from multi-band observations are explored in Section 2.2.5.

### 2.2.1 The visual magnitude–metallicity relation

The original idea of a relation between the mean luminosity of RRLs and their metallicity dates back to Baade and Swope (1955) and Sandage (1958), who discovered a correlation between the mean periods and iron abundances for cluster variables (see also Arp, 1955). These studies were driven by the evidence of a well defined dichotomy among the RRLs belonging to GGCs (Oosterhoff, 1939). Oosterhoff (1939) found two groupings of fundamental mode RRLs, one with mean periods  $P(\text{RR}_{\text{ab}}) \sim 0.55$  days and  $[\text{Fe}/\text{H}] \gtrsim -1.5$  and one with  $P(\text{RR}_{\text{ab}}) \sim 0.65$  days and  $[\text{Fe}/\text{H}] \lesssim -1.5$ . These two groups were later christened the Oosterhoff I (Oo I) and II (Oo II) groupings, respectively. Subsequently, this effect was also confirmed for field stars by Preston (1959). Figure 4 demonstrates the Oosterhoff dichotomy for GGCs using data from Catelan (2009). Figure 4 demonstrates two groupings of clusters in  $P$ - $[\text{Fe}/\text{H}]$  space that separated by a region known as as the “Oosterhoff gap.” The dichotomy is explained as the *intrinsic luminosity* for the RRLs in two Oo groups being different, with the higher metallicity Oo I clusters being

<sup>6</sup> The models are publicly available: <http://basti.oa-teramo.inaf.it/>



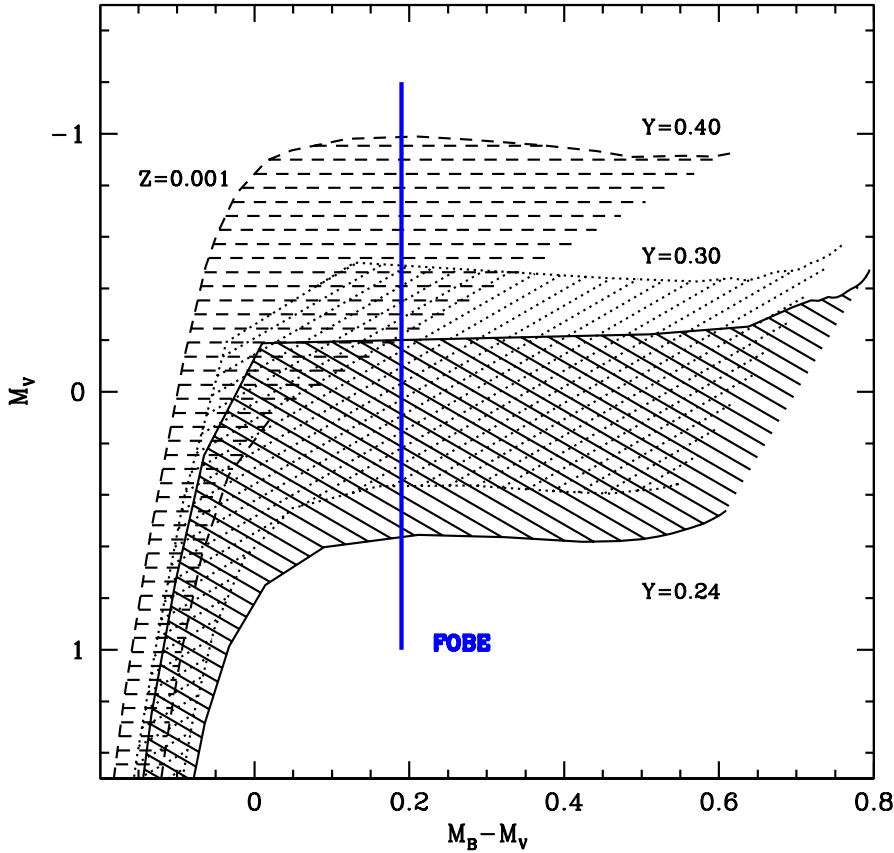


**Fig. 3** Theoretical HB models from in the color-magnitude diagram. Solid, dotted and dashed regions indicate different assumptions of the helium content for a fixed overall metallicity abundance. The vertical, blue line shows the color of the First Overtone Blue Edge (FOBE) that is almost constant for the metallicity range of the RRLs. All the theoretical models used here are taken from BaSTI (Pietrinferni et al, 2004).

fainter (Sandage, 2006). This physical understanding is largely supported by stellar evolutionary models (e.g., Cassisi and Salaris, 2013), where higher metallicity stars have both a lower helium-core mass (main parameter that setting the HB luminosity) and a higher opacity in the envelope.

We demonstrate the metallicity-trend in Figure 5 where a population of synthetic HB stars are shown for different chemical compositions ( $Z$ ) from the RRL portion of the IS (drawn from the same models shown in Figure 3). For these stars we have computed a period using the pulsation relations given in Marconi et al (2015). We show that for metal contents ranging from  $Z = 0.001$  ( $[\text{Fe}/\text{H}] \sim -1.6$  dex) to  $Z = 0.02$  ( $[\text{Fe}/\text{H}] \sim -0.3$  dex) and for a fixed  $\alpha$ -enhancement ( $[\alpha/\text{Fe}] \sim +0.3$  dex), synthetic periods become shorter by  $\Delta \log P \sim -0.1$  and luminosities become fainter by a factor of  $\Delta M_V \sim +0.3$  mag (from bottom to top

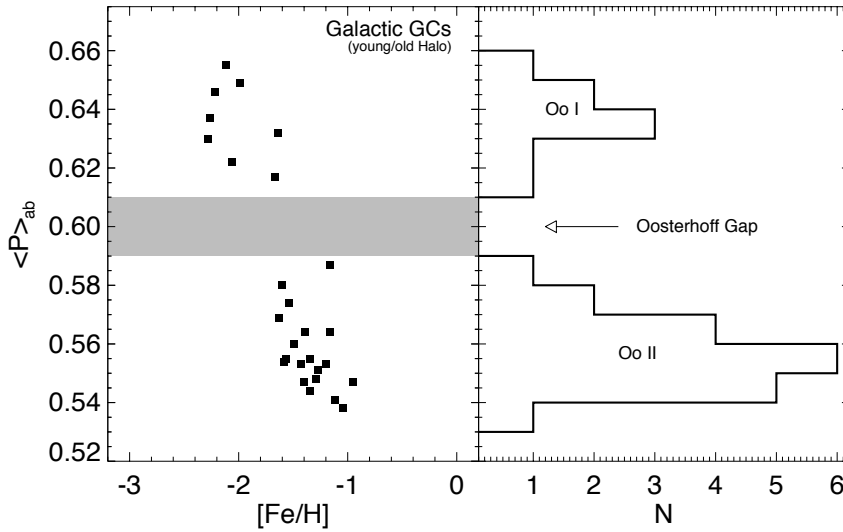


**Fig. 4** Demonstration of the Oosterhoff classification for GGCs with more than ten RRAbs using the compilation of Catelan (2009). Both “young” and “old” halo clusters have been included in this visualization. *Left panel:* The distribution of the mean period ( $\langle P \rangle_{ab}$ ) against the metallicity ( $[Fe/H]$ ) of the cluster. *Right panel:* Histogram of the mean periods that illustrates the distinct separation between the Oo-I and Oo-II type clusters. The lack of clusters with  $\langle P \rangle_{ab} \sim 0.60$  days is known as the Oosterhoff gap.

in Figure 3). However, the offset in luminosity cannot be the only cause of the difference in the mean period of fundamental RRLs between Oo I and Oo II clusters. Bono et al (1997a, and references therein) show that the dichotomy is largely due to the different pulsation behavior in the “OR region,” which is the intersection between the FU and FO IS, as a result of a hysteresis mechanism originally suggested by van Albada and Baker (1973).

Given this relation between magnitude and metallicity, it is common to assume a linear relation between the RRL  $V$ -band absolute magnitude,  $M_V$ , and the stellar metallicity, typically expressed as  $[Fe/H]$  in the following form:

$$M_V(\text{RR}) = \alpha + \gamma [Fe/H]. \quad (4)$$

Many different calibrations have been suggested in the literature for the slope ( $\gamma$ ) and the zero point ( $\alpha$ ; e.g., Liu and Janes, 1990; Carney et al, 1992; McNamara, 1997; Clementini et al, 2003; Bono et al, 2003, among others)

Despite the simplicity of Equation 4, the  $M_V$ - $[Fe/H]$  relation as a distance diagnostic has a number of drawbacks. First of all, the reddening value and the extinction law have an impact on the absolute magnitude. The extinction coefficient is quite large in optical band,  $R_V = 3.1$  (Cardelli et al, 1989), but it decreases by one order of magnitude when approaching longer wavelengths (see also Section 2.2.3). The reddening law, itself, may not be universal (Kudritzki and Urbaneja, 2012). Moreover, several complicated astrophysical effects have a strong impact on the stability of the relationship including:

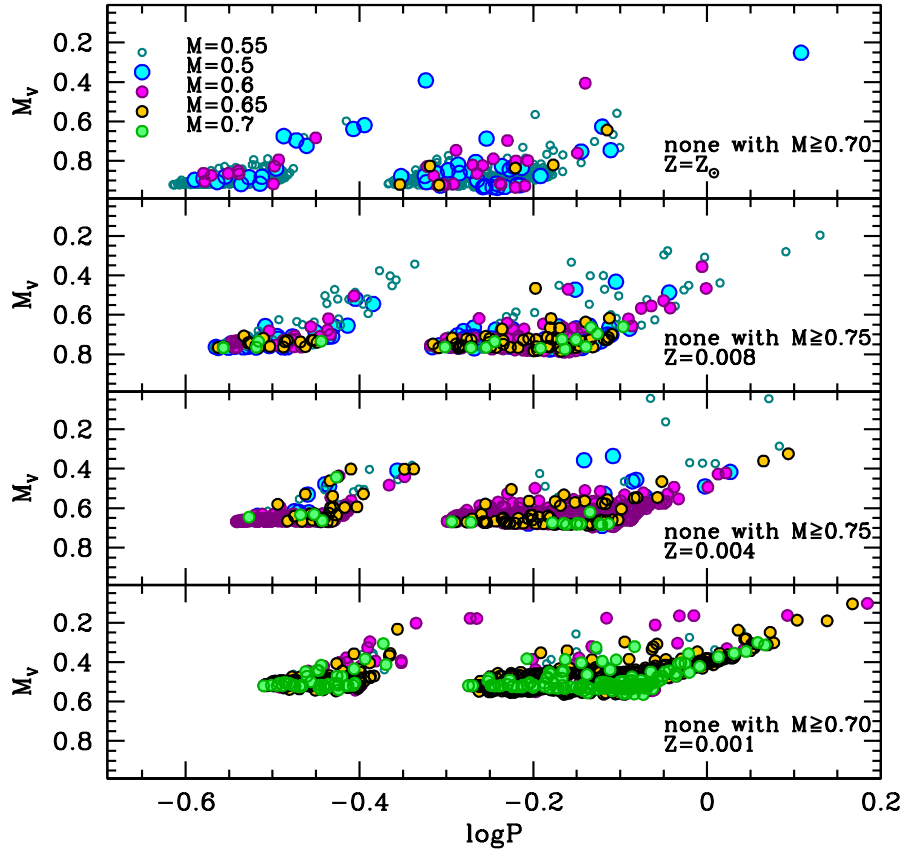


**Fig. 5** Synthetic period-magnitude diagrams for a population of RRLs as a function of metallicity from  $Z = 0.001$  (bottom panel) to Solar (top panel). A range of mean masses have been adopted for each simulation as indicated by color-coding and symbols shapes to highlight the population effects on both the mean magnitude and period.

1. intrinsic deviations from the linear form of Equation 4 (e.g., a form non-linear with iron abundance; Bono et al, 2003, 2007),
2. evolutionary effects within RRL populations,
3. measurement uncertainties for the metallicity, which include both systematic differences between metallicity scales (e.g., calibrations) and methodologies (e.g., what abundance is actually being measured),
4. measurement uncertainties for the  $\alpha$ -enhancement, and
5. deviation from static magnitudes (see also Caputo et al, 2000).

Some additional information on these effects are given in the list below:

1. *Linearity*: The assumption of the linear  $M_V$ -[Fe/H] relation (Equation 4) has been challenged many times. There is strong empirical evidence that the  $M_V$ -[Fe/H] relation is not linear over the whole metallicity range covered by the

observed GGCs (e.g., Rey et al, 2000; Caputo et al, 2000). This is also supported by both pulsational (e.g., Bono, 2003; Caputo et al, 2000; Di Criscienzo et al, 2004) and evolutionary (e.g., Catelan et al, 2004) models. The slope is observed to get steeper at approximately  $[\text{Fe}/\text{H}] = -1.5$  and, as a result, a quadratic form of this relation has been proposed (see e.g., Caputo et al, 2000; Catelan et al, 2004; Di Criscienzo et al, 2004; Sandage and Tammann, 2006; Sandage, 2006; Bono et al, 2007, among others). To provide the reader with a quantitative idea of the dependence on the metallicity and of the uncertainties, we report here the calibration by Clementini et al (2003) that is widely used:

$$V_0(\text{RR}) = 19.064(\pm 0.017) + 0.214(\pm 0.047) [\text{Fe}/\text{H}], \quad (5)$$

where the zero-point reflects the distance to LMC and the quoted uncertainties are only those on the coefficient of the linear regression. In the literature, it has been pointed out that theoretical calibrations of the  $M_V$ - $[\text{Fe}/\text{H}]$  relation consider only the Zero Age HB (ZAHB) models, and hence they do not fully take into account evolutionary effects (e.g., Catelan et al, 2004; Sandage and Tammann, 2006). However, empirical calibrations such as Caputo et al (2000) are built on observed data, with RRL variables at different evolutionary stages, and therefore they represent a “mean” evolutionary state/status for the HB. The quadratic form of the calibration, suitable for  $-2.4 < [\text{Fe}/\text{H}] < 0.0$ , determined in Bono et al (2007) and applied to the Galactic Bulge and Sagittarius dwarf in Kunder and Chaboyer (2009) is as follows:

$$M_{V,\text{RR}} = 1.19 + 0.5[\text{Fe}/\text{H}] + 0.09[\text{Fe}/\text{H}]^2. \quad (6)$$

However, it is worth noting that no deviation from linearity has been observed within the LMC over a broad metallicity range (Clementini et al, 2003). Thus, the interplay between evolutionary effects (discussed below) and metallicity is difficult to decouple in observational work. A canonical example of this difficulty is  $\omega$  Centauri, which is home multiple stellar populations, and has been deemed a “red herring” in the review of Smith (1995) due to the complexity of disentangling these effects (a more recent study is Braga et al, 2016, 2018, with additional references therein).

2. *Evolutionary Effects:* The evolutionary effects on the  $M_V$ - $[\text{Fe}/\text{H}]$  relation are shown in Figures 3 and 5. We have plotted for each selected metallicity several realizations of the HB morphology coming from different assumptions on the mean mass distribution on the HB. This is mimicking different possible values of the mass loss efficiency during the Red Giant Branch (RGB) phase, which has the result of changing the HB morphology. A comprehensive discussion of the role of mass loss on the HB morphology can be found in Salaris et al (2002, and references therein). By an inspection of Figure 5, it is clear that the HB width is not narrow due to the overlap in color-space of stars on the ZAHB and stars evolving off the ZAHB on their path to the Asymptotic Giant Branch (AGB) phase. The evolved-RRL have higher luminosities. The presence of both ZAHB-RRL and evolved-RRL on the HB defines the “evolutionary effect” As a result of the time spent on the HB, we observe RRLs until they have burned most of the He in their cores (up to  $\sim 90\%$ ). The region where a RRL spend most of its life time is also shown in Figure 3 for different He values and a given mean metallicity. This effect implies a broadening of the optical

magnitude distribution across the HB that is also correlated with the metal content, which is supported by both theory (Bono et al, 1995) and observations (Sandage and Katem, 1982).

3. *Size of the He Core:* There are other “ingredients” that affect the theoretical calibration of the  $M_V$ -[Fe/H] relation, which are related to the size of the He core reached before the He ignition. These include:
  - (a) *The initial He value:* This can be summarized as the primordial He content plus a  $\Delta Y/\Delta Z$ , which is commonly measured from H II regions. There is evidence that  $\Delta Y/\Delta Z$  may depend on the environment (e.g., Peimbert and Peimbert, 2010). An increase in total He abundance of  $\Delta \text{He} \sim +0.2$  dex implies  $\Delta M_V \sim 0.5$  mag as is demonstrated in Figure 3.
  - (b) *Details of Red Giant Evolution:* More specifically, the processes occurring along the RGB phase that delay the ignition of the 3- $\alpha$  reaction in the electron degenerate core. These include atomic diffusion, electron conductive opacity, loss of energy via neutrinos, and core rotation. Their impact on the HB luminosity can be up to  $\Delta \log(L/L_\odot) \sim 0.1$  dex or  $\Delta M_V \sim 0.2$  mag (Salaris et al, 2002; Serenelli et al, 2017).

### 2.2.2 The FOBE method

The location in the period–magnitude diagram of the FOBE can be used as a distance indicator for a population of RRL independent of the  $M_V$ -[Fe/H] relationship. The FOBE method was extensively described for the first time by Caputo (1997). This is a graphical, or topological, method that produces accurate distances for those stellar systems with sizable samples of FO RRLs (Fiorentino et al, 2010). However, it can be reliably used only when the blue part of the IS is well populated (Stetson et al, 2014b; Martínez-Vázquez et al, 2017). Once the metallicity is known, preferably from spectroscopic measurements, and a reliable mass for the RRLs can be estimated (typically in the range  $0.5 M_\odot \lesssim M \lesssim 0.7 M_\odot$ ; Bono et al, 2003), the following theoretical relation from Caputo et al (2000) can be used to fit the blue edge defined by FO RRLs to predict the absolute magnitude:

$$M_V(\text{FOBE}) = -0.68(\pm 0.03) - 2.25 \log P_{\text{FOBE}} - 1.26 \log \left( \frac{M}{M_\odot} \right) + 0.06 \log Z, \quad (7)$$

where  $P_{\text{FOBE}}$  is the period of the bluest FO pulsators and  $M_V(\text{FOBE})$  is the magnitude of the bluest FO pulsators for a given composition and mass. Although, an assumption on the RRL mass has to be made (Bono et al, 2003), the possibility to use the FOBE method relies on the well understood negligible dependence of the color of the FOBE on the metallicity (Bono et al, 1997a), which is demonstrated in Figure 3. For the bluest FO RRLs the period is most strongly dependent on luminosity and mass.

The sharp, blue edge of the IS occurs because for a given mass and luminosity, as the surface temperature increases there is less mass above the ionization zones, and in turn, their contribution to the work integral ( $p\delta V$ ) decreases. Then, the FOBE color is essentially fixed by the minimum difference between the temperature of the stellar surface and that of the Hydrogen ionization region, within which pulsation is efficient. The minimum difference is almost constant and does not depend on metallicity, at least for the metallicity range typical of RRLs. On

the contrary, the red edge of the IS strongly depends on metallicity, because the quenching mechanism for the radial pulsations is related to convection that increases with the stellar opacity, and thus by increasing the metal content (Deupree, 1977a; Stellingwerf, 1982). The above theoretical prediction has been observed in GGCs; more specifically, the  $B - V$  FOBE color is always  $\sim 0.2$  mag. Thus, the FOBE method can also be used to estimate the mean reddening of a stellar system (see Walker, 1998, for an example).

### 2.2.3 The NIR period–luminosity relations

Unlike in the optical, the observations in the IR show a true PL relationship (first identified by Longmore et al, 1986). In Figure 6, the mean magnitudes for RRL in the star cluster, Reticulum, are shown for eight photometric bands ( $B, V, I, J, H, K_s, [3.6], [4.5]$ ) against the fundamentalized period, which is defined as follows (Bono et al, 2001):

$$\log P_{\text{FU}} = \log P_{\text{FO}} + 0.127. \quad (8)$$

Reticulum is an ideal system to visualize the behavior of the PL slope with wavelength, because it has no appreciable metallicity spread on the RGB (Grocholski et al, 2006) and, thus, scatter due to metallicity differences are minimized. In Figure 6, preliminary PL fits are shown for each band as solid lines with the scatter about the PL shown as the shaded regions (Catelan and Smith, 2015, Monson et al., in prep.). As previously discussed, the  $V$  band shows no PL slope, whereas a slope appears and becomes progressively steeper at the longest wavelengths. In the next sections, we discuss empirical and theoretical results on the RRL PL.

### The $K$ -band period–luminosity relationship

Period–luminosity–color (PLC) relations have been predicted for RRL by even the earliest theoretical models (e.g., van Albada and Baker, 1971), but their use has always been hampered by several uncertainties on the structural parameters of the stars, in particular mass, effective temperature and metallicity. Evolutionary effects also play a role, because during their evolution (the He burning phase lasts at most for 100 Myr), RRLs change their luminosities and effective temperatures. Moreover, observational uncertainties, such as those associated with reddening and extinction, have to be decoupled from true astrophysical differences. Thus, empirical confirmation of the PLC has only come of late.

Longmore et al (1986) demonstrated, on pure empirical basis, that RRLs follow a tight linear PL relation in the  $K$ -band ( $\text{PL}_K$ ). They also demonstrated that the  $\text{PL}_K$  relation can be derived from the general equation of the pulsation, since the period dependence on the  $K$ -band can be derived from the  $V - K$  proxy of the effective temperature (as a direct consequence of the fact that RRLs follow PLC relations). In other words, a  $\text{PL}_K$  arises because of the increasing bolometric correction as a function of the effective temperature, with the redder RRLs having  $K$ -band magnitudes brighter than the bluer RRL (see Figure 7, for the  $K$  band). Moreover, since for a given cluster, the effective temperature distribution inside the IS is related to the period distribution, such that the stars with longer periods are also cooler, the  $K$  magnitude–effective temperature relation becomes a  $K$

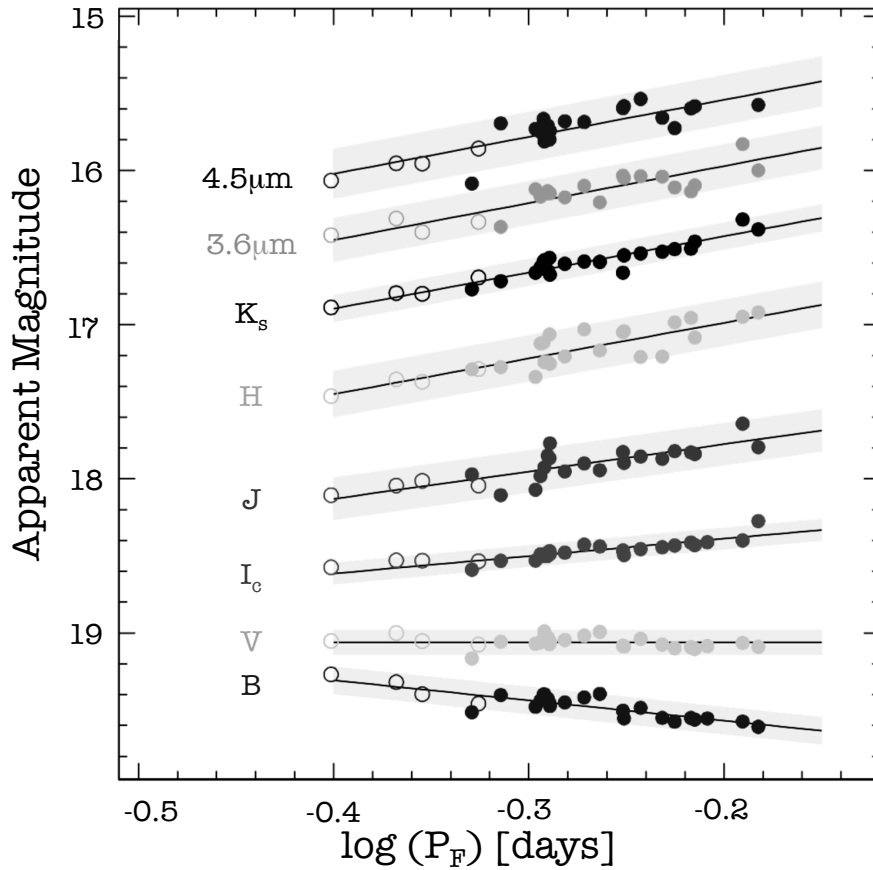


**Fig. 6** Mean apparent magnitudes for RRL in the Reticulum star cluster in the optical ( $B, V, I$ ), NIR ( $J, H, K$ ), and MIR ( $[3.6], [4.5]$ ) versus the fundamentalized period (Equation 8). PL relationships are overlotted (solid lines) for each of the bands (adapted from Catelan and Smith, 2015, Monson et al., in prep.). The change in the slope from the optical into the mid-infrared is noticeable, with  $V$  being a nearly flat slope to the mid-infrared being quite steep.

magnitude-period relation. A more general empirical calibration of the  $PL_K$  was given by Janes and Liu (1992) and these authors also considered the dependence on the metallicity, which was shown to have little impact on the slopes.

A sound and complete theoretical derivation of the  $K$ -band period–luminosity–metallicity ( $PLZ_K$ ) relation was subsequently explored by Bono et al (2001) and Bono et al (2003), finding the following:

1. the uncertainties on the mass and luminosity (e.g., on the evolutionary effects) have only a mild impact on the  $PLZ_K$ .
2. the overall dependence on the metallicity is lower, at  $\gamma \sim 0.17 \text{ mag dex}^{-1}$  in  $[\text{Fe}/\text{H}]$ , than that in the optical bands ( $\gamma > 0.2 \text{ mag dex}^{-1}$ , see Equation 5).

On the latter aspect, we remark that Sollima et al (2006) found an even lower metallicity term ( $\gamma = 0.08 \text{ mag dex}^{-1}$  in  $[\text{Fe}/\text{H}]$ ), on the basis of an empirical calibration. Muraveva et al (2015) combined low-dispersion spectroscopy of 70 RRLs

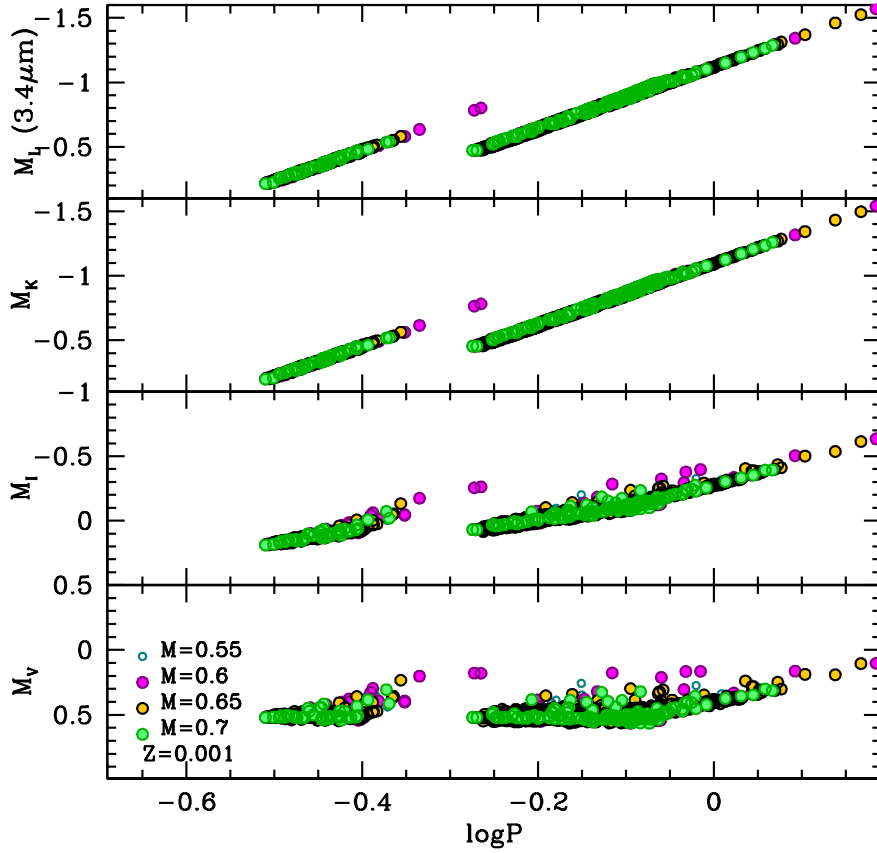


**Fig. 7** PL distribution from optical (bottom panel) to mid-infrared (top panel). We have used synthetic HB models as in Figures 3 and 5 for fixed abundance ( $Z = 0.001$ ) and a canonical He abundance ( $Y = 0.24$ ) with different mean mass for the population distribution.

in the LMC, with  $-2.0 \leq [\text{Fe}/\text{H}] \leq -0.6$  dex, with NIR photometry collected with VISTA finding a very low dependence on the metallicity ( $\gamma = 0.03 \pm 0.07$  mag dex $^{-1}$  in  $[\text{Fe}/\text{H}]$ ), and a quite steep dependence on the period ( $-2.73 \pm 0.25$ ). All these aspects reflect on a very low dispersion of the PL $Z_K$  relation, being  $\sigma = 0.035$  mag rms or  $< 2\%$  in distance (Bono et al, 2001).

PL $K$  and PL $Z_K$  observational relations have been successfully tested on several stellar systems, among the others we mention the LMC cluster Reticulum (Dall’Ora et al, 2004) and the Galactic GGCs IC 4499 (Storm, 2004), M 92 (Del Principe et al, 2005), Omega Centauri (Del Principe et al, 2006), M 5 (Coppola et al, 2011), and M 4 (Braga et al, 2015). The observed scatter about the PL ranges from 0.03 mag (Reticulum) to 0.09 mag (IC 4499), which suggests a single-star distance uncertainty ranging from 1.5% to 4.5% is feasible. Additional studies have occurred in dwarf galaxies such as the LMC (Ripepi et al, 2012a; Moretti et al, 2014), SMC (Szewczyk et al, 2009; Muraveva et al, 2018c), Fornax (Karczmarek



et al, 2017a), Sculptor (Pietrzyński et al, 2008), Carina (Karczmarek et al, 2015), and IC 1613 (Hatt et al, 2017).

Compared to the  $M_V$ -[Fe/H] relationship, the key advantages distance determination at longer wavelengths are:

1. the impact of extinction is less by a factor of ten or more and, as a result, the impact of differential extinction is also greatly reduced;
2. the impact of the uncertainties the reddening measurement, itself, are minimized (this being what is determined to estimate extinction);
3. the pulsation amplitude is lower than in the optical bands (Figure 2) and the light curves are more symmetrical, accurate mean magnitudes can be measured even with a few data points;
4. the availability of light curve templates (e.g., Jones et al, 1996; Monson et al, 2017; Hajdu et al, 2018), permits the estimation of the mean magnitudes even with a single data point, if the ephemerides of the variable are known from the optical photometry (see applications in Beaton et al, 2016, Rich et al. submitted).

On the other hand, finding the variables, measuring their periods, and determining their pulsation mode (FU or FO) is more difficult due to smaller amplitudes, sinusoidal shape, and the more uniform light curve shapes between the sub-classes. Moreover, templates is primarily only available for for the RRab type stars.

#### *Mid-IR period-luminosity relations*

The advantages of using PL relations at mid-infrared wavelengths (MIR, from 3.4 to 22  $\mu\text{m}$ ) with Cepheids have been well-recognized in the literature since McGonegal et al (1982), but only very recently it has been possible to explore this wavelength regime with RRLs. Indisputable advantages to the MIR PLs is that at 3.4  $\mu\text{m}$  the impact of interstellar absorption is more than one order of magnitude lower than in the optical bands, which permits study of heavily obscured and differentially obscured regions like the Galactic bulge that contain a large population of RRL (see discussion in Kunder et al, 2018).

Indeed, on the basis of the Wide Field Infrared Survey Explorer (WISE) measurements of field RRL variables, Klein et al (2011) were able to produce the first calibration of the PL relations at the W1 (3.4  $\mu\text{m}$ ), W2 (4.6  $\mu\text{m}$ ), and W3 (12  $\mu\text{m}$ ) bands. They subsequently refined their calibrations in Klein et al (2012) and Klein et al (2014), with no metallicity term. Another absolute calibration of the MIR PL relations was published by Madore et al (2013), using four field RRLs for which individual trigonometric parallaxes, via the *HST* Fine Guidance Sensors (*HST*-FGS), were available (Benedict et al, 2011). Even if with only four objects, the observed dispersion obtained by Madore et al (2013) is a very promising 0.1 mag ( $\sim 5\%$  in distance). Madore et al (2013) also found, as expected, only a marginal dependence on the metallicity, because at the MIR wavelengths stars with the temperature of RRLs have few molecular bands and metallic lines. Based on a much larger sample of 129 RRLs with *Hipparcos*-based statistical-parallaxes distances, Klein et al (2014) obtained very nice results, with observed spreads ranging from 0.01 mag to 0.05 mag, depending on the filter, on the sample (FU or FO pulsators), and assumptions on the intrinsic width of the PL. Neeley et al (2017) expanded the *Spitzer*-analysis to a larger sample of RRL with parallaxes

from the the TGAS catalog in *Gaia*-DR1 (e.g., Michalik et al, 2015), finding consistent solutions within the observational uncertainties. A complementary analysis from Sesar et al (2017) used *WISE* photometry with the TGAS parallaxes employing a Bayesian algorithm, which Muraveva et al (2018a) has expanded upon recently using *Gaia*-DR2.

The first calibration of the MIR PL using cluster variables was published by Dambis et al (2014), which presented an analysis of *WISE* data for 15 GGCs. Neeley et al (2015, 2017) published data of the GGC M4, collected with the Infrared Array Camera (IRAC) on-board the *Spitzer* Space Telescope, obtaining PL relations in the IRAC [3.6] and [4.5] bands with a scatter of  $\sim 0.05$  mag (2.5% in distance). Muraveva et al (2018b) has recently published a calibration in the LMC star cluster Reticulum.

#### 2.2.4 The RR Lyrae period–luminosity slopes

Because the bolometric correction sensitivity to effective temperature is already at work starting from the *R*-band (see Cassisi et al, 2004; Catelan et al, 2004; Marconi et al, 2015), PL relations have also now been derived theoretically for the photometric bands *R*, *I*, *J* and *H*, which are shown in Figure 7. At shorter wavelengths, the effects related to the finite width of the IS and evolution of RRLs are larger and produce PL relations with larger intrinsic scatter (compare the panels of Figure 7). The relationships in *R*, *I*, *J* and *H* are still of great interest, because these wavelengths can be observed easily from the ground.

In Figure 8, the PL slopes determined from a subset of both empirical (triangles) and theoretical (circles) investigations are plotted versus wavelength following the example of Madore et al (2013). These slopes are for the “global” population, e.g., the first-overtone periods have been fundamentalized following Equation 8. The shaded region in Figure 8 is meant to guide the eye to the behavior with wavelength and this is adapted from the visualization in Madore et al (2013, their figure 4). Generally, the slopes between the different studies, both theoretical and empirical, agree well. Still, there are comparatively few studies on the PL for wavelengths longer than *V* and further investigations, in particular empirical studies in star clusters with differing chemical compositions and evolutionary states, are highly relevant to determining a “consensus” PL slope for a given filter.

In Figure 8, the “predicted” slopes from the period-radius (PR) or period-radius-metallicity (PRZ) relationships are also shown following Madore et al (2013). NIR and MIR wavelengths sample the Rayleigh-Jeans tail for RRLs and, as a result, the magnitudes are much less sensitive to temperature than to the radial variations. This behavior is readily seen in the light curves shown and, indeed, the light curves beyond *H* are nearly indistinguishable. Thus, predicting the PL slope from the period-radius relationship places an asymptotic limit on the PL slopes.

Starting from  $L = 4\pi R^2 \sigma T_{\text{eff}}^4$  and converting into a logarithmic form yields the following,

$$\log L = \log(4\pi\sigma) + 2\log R + 4\log T_{\text{eff}}, \quad (9)$$

which can be converted into magnitudes as follows,

$$\log M = -5\log R - 20\log T_{\text{eff}} + \text{constant}. \quad (10)$$

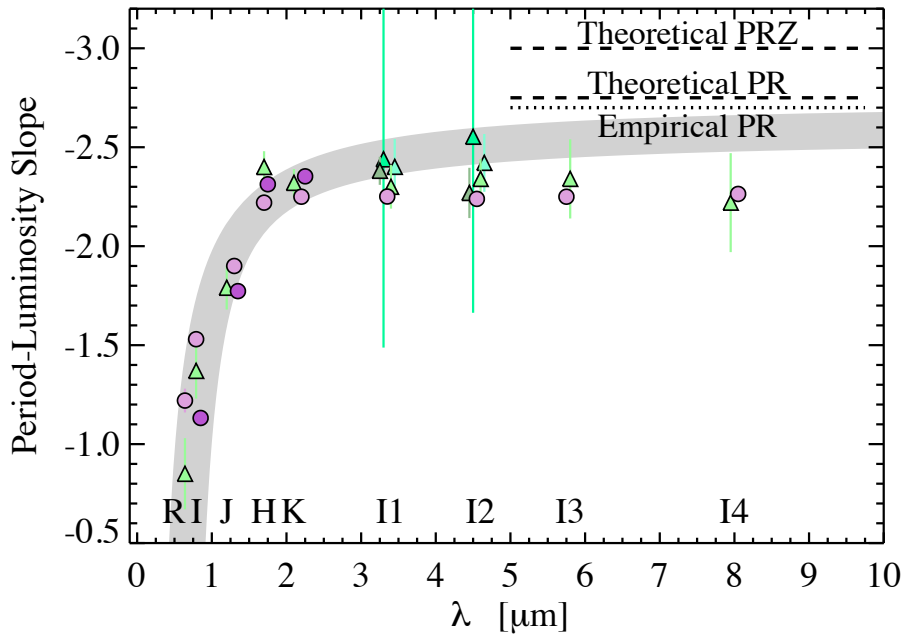


**Fig. 8** Following Madore et al (2013, their figure 4), the PL slopes are plotted as a function of wavelength from both theoretical (circles; Catelan et al, 2004; Marconi et al, 2005a, 2015; Neeley et al, 2017) and empirical (triangles; Klein et al, 2011; Madore et al, 2013; Braga et al, 2015; Dambis et al, 2014; Neeley et al, 2015, 2017) studies. We note that studies in the same photometric band have been offset slightly in their effective wavelength for visualization purposes. The shaded region is drawn to guide the eye following Madore et al (2013). The slopes for the long-wavelength filters asymptotically approach that predicted by period-radius relationship for both theory (dashed line Marconi et al, 2015) and empirical determinations (dotted line Burki and Meylan, 1986).

From here, we can substitute either the period-radius (PR) or period-radius-metallicity (PRZ) relationship to remove the radius term. The PR has been determined in several ways, (i) empirically by Burki and Meylan (1986) using the Baade-Wesselink technique (BW), (ii) stellar evolutionary models by Marconi et al (2005b) (evol), and (iii) pulsation models by Marconi et al (2015) (puls). The PR/PRZ takes the form,  $\log R = a + b \log P + c \log Z$ , and the three studies find period slopes of  $b_{\text{BW}} = 0.54$ ,  $b_{\text{evol}} = 0.65$ , and  $b_{\text{puls}} = 0.55$ , respectively. Substituting, these into Equation 10, we estimate determine period slopes of  $\beta_{\text{BW}} = -2.7$ ,  $\beta_{\text{evol}} = -3.25$ , and  $\beta_{\text{puls}} = -2.75$ .

If we assume that the temperature term contributes very little at long wavelengths then we can ignore that term to obtain an estimate for the slope of the PL relationship. The estimated slopes from the theoretical PR and PRZ (dashed lines; Marconi et al, 2015) and the empirical PR (dotted lines Burki and Meylan, 1986) are shown in Figure 8. The overall agreement between these asymptotic values and the slopes in Figure 8 serves as a good cross-check on our theoretical and empirical measurements.

### 2.2.5 Reddening-free relations

Even if PLZ relations have advantages for estimating individual distances, they are still affected by the uncertainties in the reddening corrections, and the problem can be severe in regions affected by strong differential reddening (e.g., as in M4 Braga et al, 2015, or in the Galactic Bulge).

To circumvent this problem, van den Bergh (1975) and Madore (1982) developed the Wesenheit pseudo-magnitudes. They are, by construction, “reddening free” functions that redefine the observed magnitude. The fiducial form of the transformation is defined as:

$$W(A, B) = M_A + R_{A,B}(M_A - M_B) \quad (11)$$

where  $R_{A,B}$  is the selective-to-total extinction ratio. In the common practice, “Cardelli’s law” is adopted (Cardelli et al, 1989).

The Wesenheit period–luminosity (PW) and period–luminosity–metallicity (PWZ) relations have the following form:

$$W = \alpha + \beta \log P + \gamma [\text{Fe}/\text{H}], \quad (12)$$

where each combination of filters will have its own set of PWZ parameters. The advantages and disadvantages of PW and PWZ relations have been discussed several times in the literature, in particular for classical Cepheids (e.g., Inno et al, 2013; Fiorentino et al, 2007; Ngeow et al, 2005; Storm et al, 2011; Ripepi et al, 2012b) and, more recently, with RRLs (e.g., Braga et al, 2015; Marconi et al, 2015, and references therein).

Briefly, the main features can be summarized as follows:

1. the individual distances are independent of the uncertainties in the reddening or in differential reddening within an RRL population;
2. a universal reddening law is assumed, but there are indications of deviations from “Cardelli’s law” in regions of high obscuration (Cardelli et al, 1989);
3. PW and PWZ relations mimic PLC relations, since they host the color term: this means that the effect of the width of the IS is reduced, and individual distances are much more precise than those obtained with simple PL relations.

Thus, in regions where the assumption of universal reddening law is reasonable, the PW/PWZ is a powerful tool.

On the practical side, however, use of the PW/PWZ are more observationally expensive than common PL and PLZ relations, because they need accurate mean magnitudes determined in two photometric bands. According to the models by Marconi et al (2015), the dispersion around the PW and PWZ relations range from  $\sim 0.01$  mag (in the NIR bands) to  $\sim 0.07$ – $0.08$  mag (in the optical bands). Braga et al (2015) provide complementary empirical PW/PWZ relations determined from M4 in the optical and NIR. The  $PW_{B,V}$  relation is almost independent of metallicity and are particularly useful.

We also note that, on empirical basis, Riess et al (2011) proposed to use three-band PW relations, where the  $W$  magnitude is reconstructed from the following form,

$$W(A, B, C) = M_A + R_{A,B,C}(M_B - M_C), \quad (13)$$

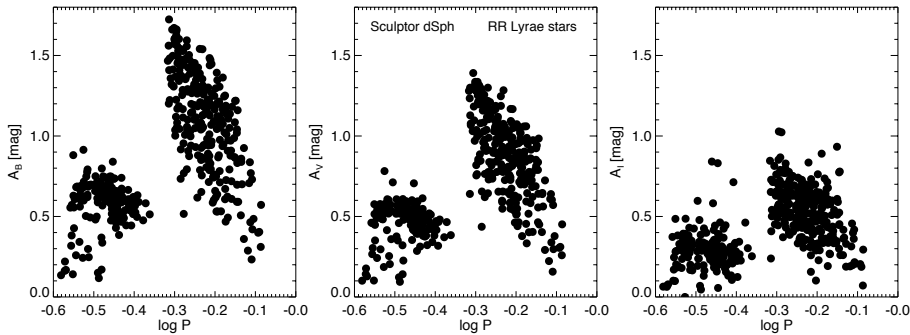


**Fig. 9** Period-amplitude diagrams for the RR Lyrae stars in Sculptor in three different optical bands:  $B$  (left),  $V$  (middle) and  $I$  (right). RRab and RRc are shown as black circles. For the sake of clarity, RRd stars are not plotted as their periods are less certain. The RRc and RRab occupy specific regions in the Bailey diagram, with the RRc having shorter periods and smaller amplitudes (i.e., in the bottom left) than the RRab’s (right). The RRab’s also have a broader range of amplitudes. These primary groups in the Bailey diagram can be further refined into specific sequences for the Oo groups, with two clear sequences visible for the RRab’s.

where  $R_{A,B,C}$  is the ratio between the selective absorption in the  $A$  band, and the color excess for the  $B - C$  color  $E(B - C)$ . The advantages of triple band PW/PWZ relations are a smaller dispersion respect to the two band relations and lower systematics from correlated errors having used the same magnitude in the color term. The drawback is that they need accurate mean magnitudes determined for three bands. The most advanced theoretical study on this topic to date is that of Marconi et al (2015), which provides theoretical three-band relations for RRL in the optical and NIR.

### 2.3 Case studies using RR Lyrae

In the previous section, a general physical understanding of RRLs as distance indicators was developed using both theoretical and empirical investigations. In this section, a series of case studies are presented on the practice of using RRLs for the different wavelength regimes discussed previously. In Section 2.3.1, the  $M_I - [\text{Fe}/\text{H}]$  relationship and the optical PW relationships are applied to the Sculptor dwarf galaxy. In Sections 2.3.2 and 2.3.3, the optical, near-infrared and mid-infrared PL relations are determined and applied to the nearby GGC M 4 that suffers from strong differential reddening in the optical.

#### 2.3.1 An optical study of RR Lyrae in Sculptor

Here we present a brief summary of a comprehensive study of the RRLs in the Sculptor dwarf galaxy (Martínez-Vázquez et al, 2015, 2016a,b). Sculptor is a Milky Way dwarf spheroidal (dSph) satellite with a complex chemical enrichment history (Smith and Dopita, 1983; Da Costa, 1984; Majewski et al, 1999; Hurley-Keller et al, 1999; Tolstoy et al, 2004; de Boer et al, 2012; Starkenburg et al, 2013). Tolstoy et al (2004) demonstrated that the red HB stars (RHB) are more centrally concentrated

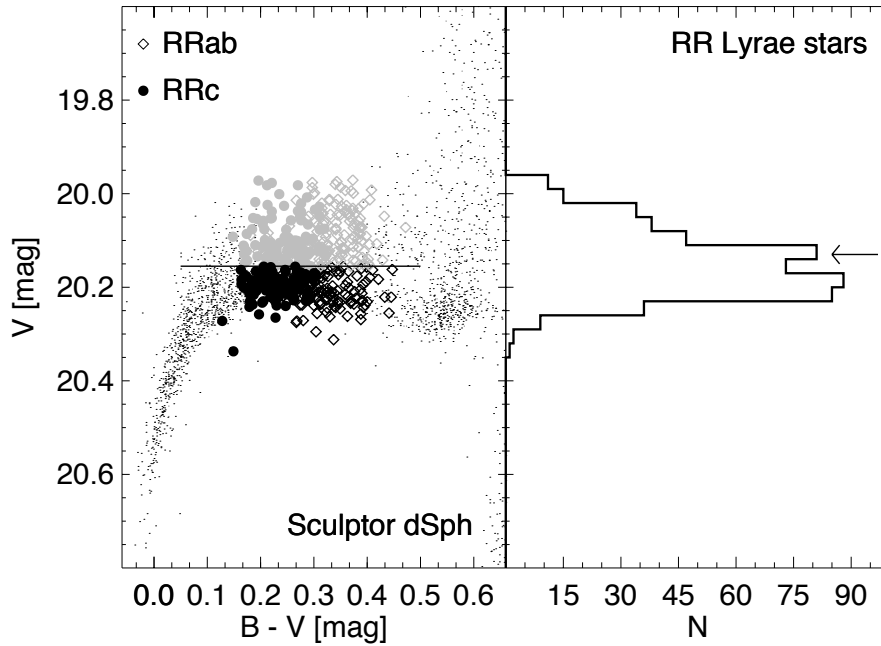


**Fig. 10** The  $V$  distribution for Sculptor RRL. *Left panel:* Zoom-in on the HB stars in the color-magnitude diagram of Sculptor. The horizontal line (at  $V = 25.155$  mag) displays the split between bright (gray) and faint (black) RRL subsamples. Open diamonds and circles represent the RRab and RRc stars, respectively. *Right panel:* Luminosity distribution function in  $V$  band for Sculptor RRLs. The arrow marks the magnitude adopted to split into bright and faint RRL subsamples. We note that the RRd and other more complicated RRL sub-types have been removed from this sample.

than the blue HB stars (BHB) that mirrors gradients from detailed spectroscopic studies on the RGB Battaglia et al (2008); Walker et al (2007, 2009); Kirby et al (2009); Leaman et al (2013); Ho et al (2015), which suggests a that range of metallicities in also present the RRL population.

Time series photometry was produced for stars Sculptor from a set of 5149 individual images collected over 24 years. Variables were identified using the Welch-Stetson variability index (Welch and Stetson, 1993) and periods obtained from a simple string-length algorithm (Stetson et al, 1998) from which 536 RRLs were identified using the the shapes of the light curve. The final dataset contains pulsational properties and mean magnitudes for 536 RRLs in the  $B$ ,  $V$ , and  $I$  bands that is complete over  $\sim 70\%$  of Sculptors area.

Figure 9 shows the Bailey Diagrams for the  $B$ ,  $V$ , and  $I$  bands. The RRab and RRc stars separate into long- and short-period groups, that have their own amplitude behavior. The overall reduction of the amplitudes from the  $B$  to the  $I$  band is apparent. In the  $B$  and  $V$  the sub-division of the primary RRab and RRc sequences into Oo groups can also be seen, which is anticipated from the large metallicity spread.

Figure 10 shows the  $V$  magnitude distribution for the Sculptor RRLs. A zoom-in on the CMD is shown in the left panel and the corresponding luminosity function

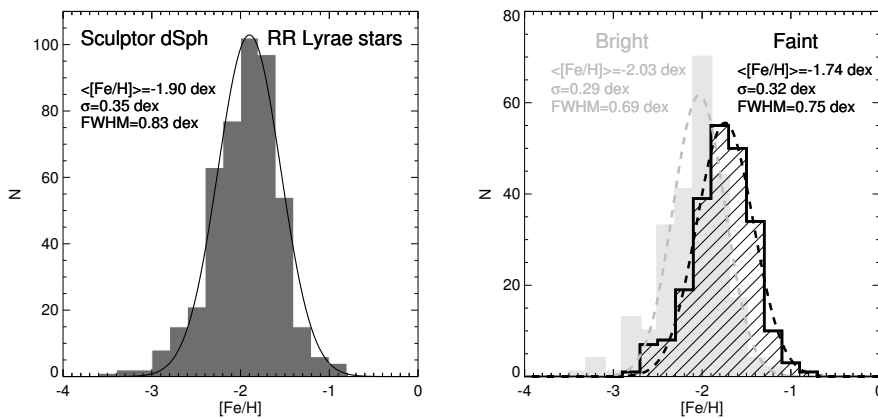


**Fig. 11** *Left panel* Metallicity distribution obtained from the PL in  $I$  band for the RRLs of Sculptor (dark grey histogram). The black solid line show the Gaussian fit performed. The parameters of the fit are labeled in the panel. *Right panel* Metallicity distribution for the bright (light grey histogram) and faint RRL subsample. Both distributions have been fitted to a Gaussian (dashed curves). The parameters of each fit are labeled in the panel.

for the RRLs is shown in the right panel. The RRL stars of Sculptor show a spread in  $V$  magnitude of  $\sim 0.35$  mag, which is significantly larger than the typical uncertainties in the mean magnitude ( $\sigma = 0.03$  mag), larger than anticipated for a mono-metallicity population showing evolutionary effects, and larger than the intrinsic spread for a mono-metallicity population.

The  $I$ -band PLZ ( $PLZ_I$ ) can be used to obtain the metallicity distribution for the RRLs following Martínez-Vázquez et al (2016a):

1. A cross comparison of the photometric metallicities to the spectroscopic measurements from Clementini et al (for several dozen sources; 2005).
2. Application of the technique to RRL in Reticulum, which has a well-defined spectroscopic metallicity (e.g., Mackey and Gilmore, 2004) and well-sampled  $I$  light curves (Kuehn et al, 2013).

Both tests validated the photometric metallicities obtained using the  $PL_I$  and the results of this analysis for the Sculptor RRLs are given in Figure 11. In Figure 11, the left panel shows the full distribution for Sculptor and the right panel emphasizes the difference in the population split into the Bt and Ft groups identified from the  $V$ -magnitudes.

The distribution of RRLs are centered at  $-1.90$  dex, with  $\gtrsim 90\%$  of the sample between  $-1.2$  and  $-2.6$  dex (left panel of Figure 11). The Bt sample is on average more metal-poor, with mean metallicity of  $-2.03$  dex, than the Ft sample that has a mean metallicity of  $-1.74$  dex (right panel of Figure 11).

The distance to Sculptor was determined using the metal-independent PW relations for the  $V$ ,  $B-V$  and  $V$ ,  $B-I$  filter-color combinations (e.g., Equation 11 and 13) with parameters from Marconi et al (2015, their table 9) and Martínez-Vázquez et al (2015, their table 2), respectively. Marconi et al (2015) demonstrated that these PW relations are relatively insensitive to metallicity, which is important for the large metallicity spread in Sculptor. These PW relations were applied to

each of three subsamples within the RRL population: (i) RRab, (ii) RRc, and (iii) the global sample (both RRab and fundamentalized RRc).

The zero-points of the PW relationships are not well constrained from observations as there are only good (<10%) trigonometric parallaxes for five RRL, even after the release of the TGAS parallaxes from *Gaia* DR1 (Lindgren et al, 2016, and references therein) Thus, three different approaches were used to quantify the effect of both the zero-point ( $\alpha$ ) and the slope ( $\beta$ ) of the relation on the distances. These are:

1. *Theoretical*: Using the zero-points and slopes of the predicted PW relations
2. *Semi-empirical*: Using the same theoretical zero-points and the empirical slopes, which were obtained from the fit performed in the plane of both observational Wesenheit magnitudes versus  $\log(P)$  the RRLs.
3. *Empirical*: Adopting observed slopes used in the previous method, but using the zero-points determined from *HST* trigonometric parallaxes (Benedict et al, 2011). More specifically, RR Lyr, itself, to calibrate both the RRab and the global samples and RZ Cep to calibrate the RRc sample.

The full details of these distance determinations can be found in Martínez-Vázquez et al (2015, in particular, section 4 and their table 3).

The zero-points are determined for each of the four RRab, global, and RRc PW relations. For the RRab and global relations, the zero-points agree quite well with theoretical ones. However, in the case of the RRc, the new zero-points are  $\sim 30\%$  smaller than predicted, which is in agreement with the mean RRc magnitude determined from Kollmeier et al (2013) from statistical parallax and highlights the need to use a large sample to determine robust zero points.

The final result is  $\mu_0 = 19.62$  mag with  $\sigma_{mean} = 0.04$  mag, which is in good agreement with previous determinations (e.g., Rizzi, 2002; Pietrzyński et al, 2008, among others). The multiple methods required to set the zero-points and slopes of the PW relationships also emphasizes the role that high-quality trigonometric parallaxes for field RRLs, and later cluster RRLs, will play in improving the accuracy of the distances determined via the RRL PL, PLZ, and PW relationships.

### 2.3.2 A near-IR study of the RRLs in M4

We present a case study using the GGC M4. M4 is the closest GGC to the Sun and it hosts a sizable sample of RRLs (Stetson et al, 2014b), but the cluster suffers from strong differential extinction. The mean reddening is  $E(B - V) = 0.37$  mag with a range of  $\Delta E(B - V) = 0.10$  mag – or a mean  $A_B$  ( $A_V$ ) of 1.81 mag (1.37 mag), with variations at the 0.4 mag level across the cluster. In contrast, the IR reddening is  $E(J - H) = 0.13$  mag with a variation of only  $\Delta E(J - H) = 0.04$  mag – or a mean  $A_H = 0.22$  mag with variation at the  $\sim 0.1$  mag level.

The data for M4 is similar in its volume and time-baseline to that for the Sculptor dwarf from Section 2.3.1 and is described in full in Stetson et al (2014b). The optical data was obtained in 18 runs over 16 years for a total of over 5000 images in  $U$ ,  $B$ ,  $V$ ,  $R$ , and  $I$  filters. The NIR data was obtained in 18 runs over 10 years in  $J$ ,  $H$ , and  $K$ . The final RRL census in M4 contains 32 RRab and 12 RRc for a total of 45 RRL.

Figure 12a shows the optical CMD for M4 and Figure 12b is a histogram of the mean magnitudes in  $V$  for the RRLs, both of which can be compared directly



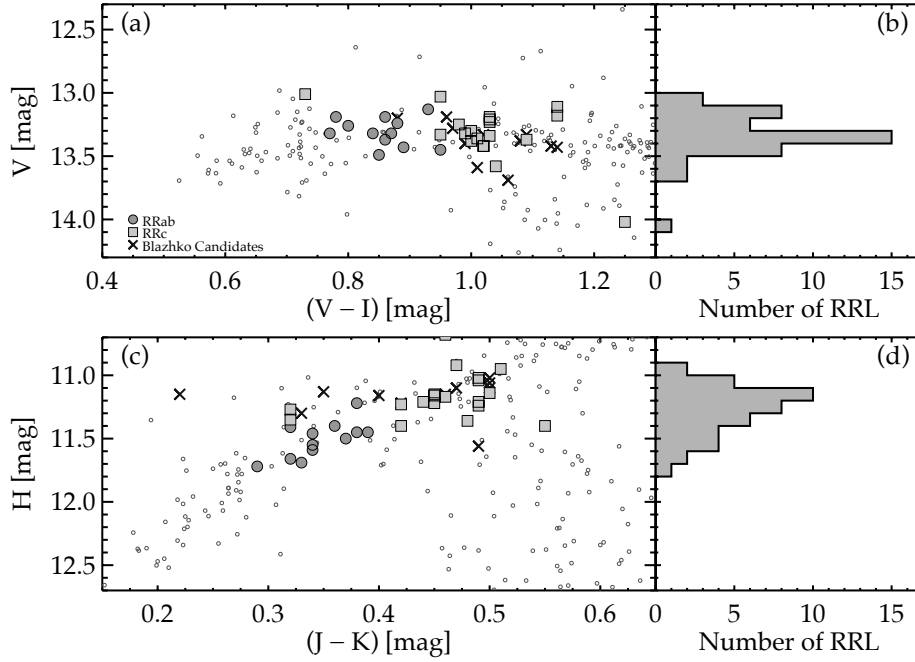


**Fig. 12** Optical and NIR CMDs for M4. (a): Optical  $V - I, V$  CMD for the HB in M4 (data from Stetson et al, 2014a). The RRab (circles), RRc (squares), and Blazhko candidate RRLs are indicated. (b):  $V$  magnitude histogram. The dispersion of the distribution is  $\sim 0.18$  mag, which, despite the differential reddening, is much narrower than that of Sculptor (Figure 10) due to the lack of strong metallicity gradients. (c): NIR  $J - K, H$  CMD for the HB in M4 (data from Stetson et al, 2014a). Unlike the optical (a), the NIR HB has a noticeable slant that gives rise to the PL. (d):  $H$  magnitude histogram where the width is due to the PL. The y-axis for all panels is 2.0 mag for ease of comparison.

to the corresponding panels of Figure 10 showing the same for Sculptor. M4 has a dramatically smaller metallicity spread than Sculptor, but it suffers from strong differential extinction in the optical, which creates a broadened distribution of RRL magnitudes. Figure 12c is the NIR CMD for M4 and Figure 12d is a histogram of the mean magnitudes in  $K$  for the RRLs.

#### Period-luminosity relations

Figure 13 shows the empirical PL relations in the  $J$  (top),  $H$  (middle), and  $K$  (bottom) bands for the RRab and RRc in M4. The RRab and RRc RRL are shown independently in Figure 13 with their native periods. The resulting PL relations are given below. First, for the RRab stars:

$$\begin{aligned}
 J_{RRab} &= -2.030 (\pm 0.204) \log P + 10.946 (\pm 0.056) \quad \sigma = 0.065 \\
 H_{RRab} &= -2.215 (\pm 0.176) \log P + 10.537 (\pm 0.047) \quad \sigma = 0.050 \\
 K_{RRab} &= -2.372 (\pm 0.142) \log P + 10.410 (\pm 0.039) \quad \sigma = 0.045
 \end{aligned} \tag{14}$$

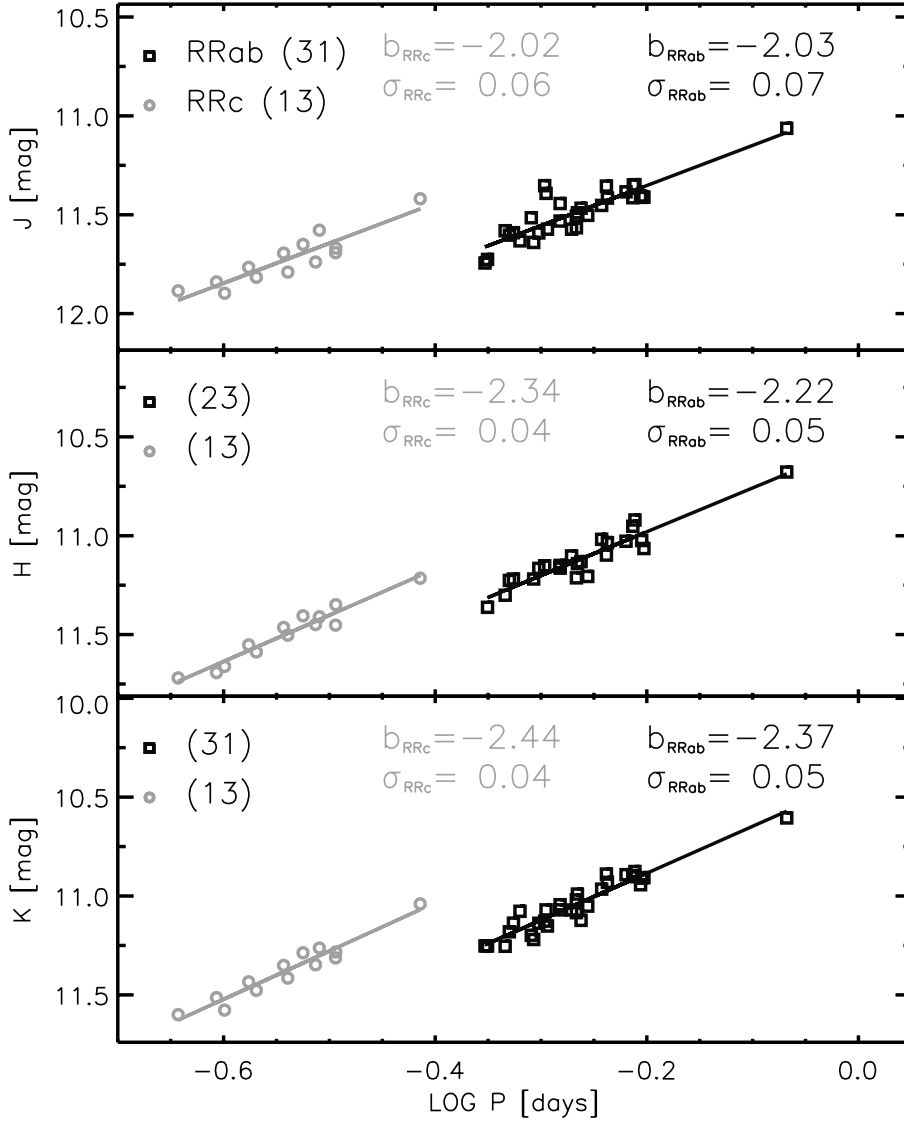


**Fig. 13** NIR PL relations for RRL in M4. *Top:* Empirical  $J$ -band PL relations of the RRLs of M4. Light circles represent RRcs, while dark squares mark the position of RRabs. Slopes ( $b$ ) and dispersions ( $\sigma$ ) of the relations are labeled. *Middle:* same as top, but for  $H$ -band PL relations. *Bottom:* same as top, but for  $K$ -band PL relations

For the RRc,

$$\begin{aligned}
 J_{RRc} &= -2.020 (\pm 0.273) \log P + 10.634 (\pm 0.148) \quad \sigma = 0.056 \\
 H_{RRc} &= -2.340 (\pm 0.179) \log P + 10.232 (\pm 0.097) \quad \sigma = 0.037 \\
 K_{RRc} &= -2.440 (\pm 0.198) \log P + 10.058 (\pm 0.108) \quad \sigma = 0.041
 \end{aligned}
 \tag{15}$$

Lastly, the global PL uses fundamentalized periods for the RRc variables (e.g., Equation 8), which is not shown explicitly in Figure 13:

$$\begin{aligned} J_{Glob} &= -1.793 (\pm 0.109) \log P_F + 11.002 (\pm 0.035) \sigma = 0.064 \\ H_{Glob} &= -2.408 (\pm 0.082) \log P_F + 10.492 (\pm 0.027) \sigma = 0.046 \\ K_{Glob} &= -2.326 (\pm 0.074) \log P_F + 10.420 (\pm 0.024) \sigma = 0.043 \end{aligned} \quad (16)$$

These slopes and their dispersions are also labeled on the top of each panel in Figure 13. As expected, the slope increases with wavelength as PL approaches the PR relation (e.g., Figure 8). The dispersion in  $K$  (0.06 mag) is half that of the  $R$  for this cluster (Braga et al, 2015), further emphasizing a strength of the NIR PL.

The distance to M 4 can be determined once the zero-point of the PL is calibrated. Similar to the methods for Sculptor, this can be done either on an empirical or on a theoretical basis, as we describe below:

1. *Empirical*: Zero points are determined by adopting the *HST* parallaxes (Benedict et al, 2011) and the mean *JHK* magnitudes (Sollima et al, 2008) for RR Lyr (an RRab). Note that the *HST* parallaxes have smaller uncertainties than those from TGAS in *Gaia* DR1 (Lindegren et al, 2016).
2. *Theoretical*: Zero points are adopted from the predictions of the theoretical PLZ relations (Marconi et al, 2015). The metallicity term is taken into account by adopting a fixed  $[\text{Fe}/\text{H}] = -1.1$  dex, which is the average iron abundance of M 4 (Marino et al, 2008; Malavolta et al, 2014).

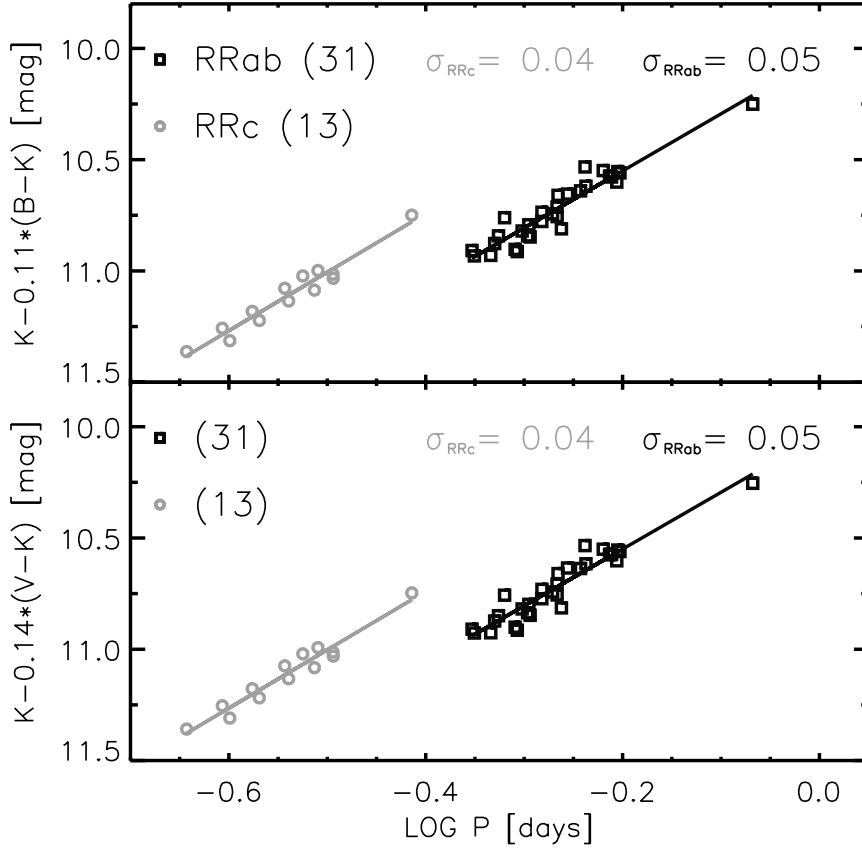
The two methods provide distances of  $\mu_0 = 11.35 \pm 0.03$  (standard error)  $\pm 0.05$  (standard deviation) mag and  $\mu_0 = 11.283 \pm 0.010$  (standard error)  $\pm 0.018$  mag (standard deviation), respectively (see Braga et al, 2015, for additional details). Both are in agreement within  $1 \sigma$  with estimates of the distance modulus from the literature, in particular that derived from eclipsing binaries of  $\mu_0 = 11.30 \pm 0.05$  mag ( $1\text{-}\sigma$  agreement; Kaluzny et al, 2013).

Figure 14 shows two PW relationships in  $B,B - K$  and  $K,V - K$  for M 4 from Braga et al (2015) that combine both optical and NIR magnitudes. Using these relationships, calibrated in a similar fashion, provide  $\mu_0 = 11.272 \pm 0.004 \pm 0.013$  mag, in perfect agreement with the distance moduli determined from the PLs. For the two relationships shown in Figure 14, the dispersions are between 0.04 and 0.05 mag. The small dispersions and the agreement between these distance moduli and those from the NIR PL provide empirical validation that the PW relationships are indeed insensitive to reddening and that the assumptions of the PW relationship (e.g., ‘‘Cardelli’s Law’’) work well for M 4 in the NIR.

### 2.3.3 A MIR study of RR Lyrae in M 4

The MIR case study also uses the closest GGC, M 4. Due to the smaller amplitudes at longer wavelengths, it is not practical to identify and derive the pulsation characteristics using only MIR data (e.g., Figure 2). Therefore we rely on ground-based optical and NIR data described previously to provide the coordinates and periods of our target RRL, which then sets the optimal strategy to derive well sampled light curves in the MIR (see also Hendel et al, 2018; Muraveva et al, 2018b).

Intensity mean magnitudes are computed either from Fourier fitting techniques (as in Dambis et al, 2014) or the GLOESS method (as in Monson et al, 2017). Using



**Fig. 14** Three-band PW relationships for RRL in M4. *Top*: Empirical PW( $K, B - K$ ) relations of the RRLs of M4. Light circles represent RRcs, while dark squares mark the position of RRabs. The dispersions ( $\sigma$ ) of the relations are labeled. *Bottom*: same as top, but for PW( $K, V - K$ ) relations

the exquisite multi-band data available for M4 and described in this chapter, the extinction and distance to M4 can be measured using a semi-empirical method, as described in Neeley et al (2017). The photometry was simultaneously fit in each band to theoretical PLZ relations, finding an extinction of  $A_V = 1.45 \pm 0.12$  (assuming  $R_V = 3.62$  measured directly in the foreground of M4 by Hendricks et al, 2012) and a distance modulus of  $\mu_0 = 11.257 \pm 0.035$  mag. Both this value and the fully empirical results above are in good agreement with other distance methods, (e.g. eclipsing binaries from Kaluzny et al, 2013) as well as from RRL in the NIR (Braga et al, 2015).

The empirical PL relations using both *Spitzer* and *WISE* data are given in Figure 16. Periods of the RRab stars (shown as open circles) have been fundamentalized following Equation 8. The empirical MIR PL relations for M4 for the

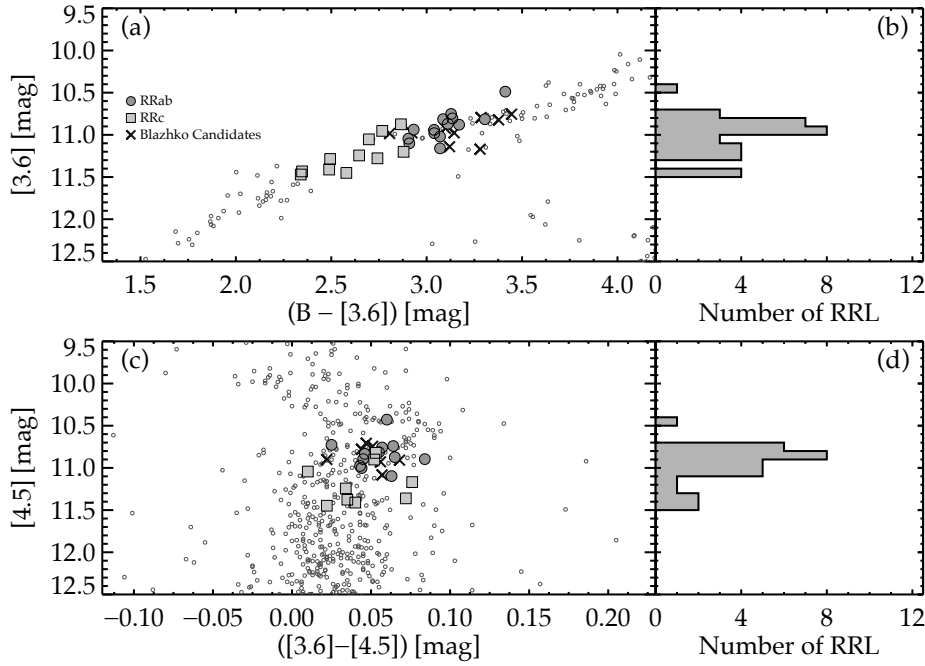


**Fig. 15** MIR photometry for the HB in M4. (a) Joint opt-MIR CMD for the HB in M4 (data from Stetson et al, 2014a; Neeley et al, 2015) with the RRL common to both datasets indicated. (b) Distribution of [3.6]-mag for the RRLs in M4. (c) MIR CMD for the HB in M4 (data from Neeley et al, 2015) that demonstrates the HB is not readily identifiable in MIR CMDs. Identification and classification of RRLs is much more readily completed in the opt or NIR, but the RRc variables are noticeably fainter. (d) Histogram of [4.5] magnitudes for the RRLs in M4.

“global sample” are as follows:

$$\begin{aligned}
 [3.6]_{Glob} &= -2.304(\pm 0.105) \log P_F + 10.241(\pm 0.034) \\
 [4.5]_{Glob} &= -2.340(\pm 0.104) \log P_F + 10.225(\pm 0.034) \\
 W1_{Glob} &= -2.694(\pm 0.213) \log P_F + 10.145(\pm 0.213) \\
 W2_{Glob} &= -2.540(\pm 0.248) \log P_F + 10.182(\pm 0.249).
 \end{aligned} \tag{17}$$

The dispersion on the IRAC relations is 0.05 mag and is approaching the expected intrinsic scatter of the PL relation ( $\sim 0.03$  mag). The difficulty of deriving accurate photometry in clusters using WISE data (due to the larger PSF) results in a larger dispersion of  $\sim 0.09$  mag. The observed slopes are in good agreement with theoretical PL relations derived from pulsation models (see discussion in Neeley et al, 2017).

To use the PL to determine a distance, the absolute zero point must be calibrated with RRL of known distances. Similar to the NIR study of M4, there are two methods:

1. *Empirical*: Adopting observed slopes from M4 RRLs and zero points are determined using trigonometric parallaxes for Galactic RRLs (either from *HST*-FGS or *Gaia*).

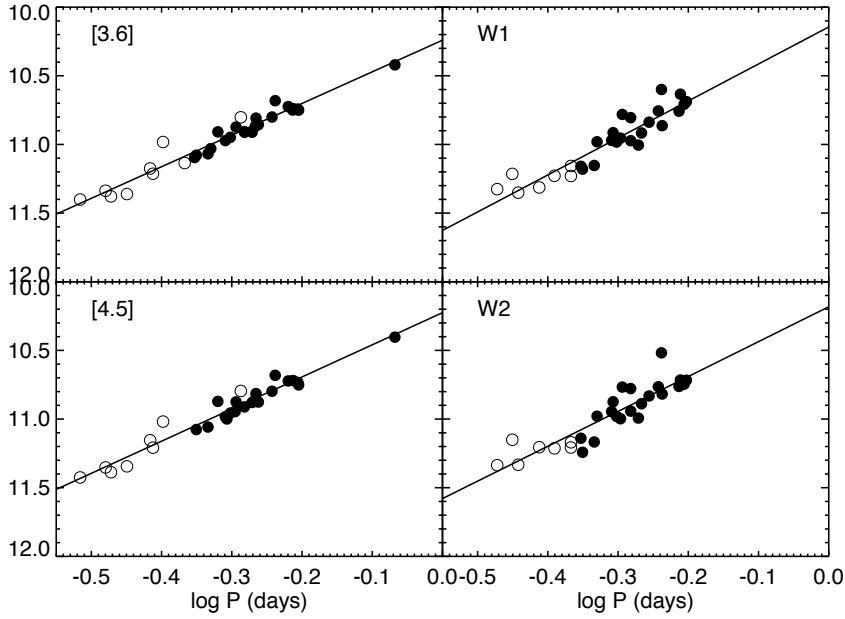


**Fig. 16** IRAC (left) and WISE (right) PL relations for RRL in M4 using data from Neeley et al (2015) and Dambis et al (2014). Periods of the first overtone pulsators (open circles) have been fundamentalized (e.g., Equation 8).

2. *Semi-empirical*: The distance and extinction are measured simultaneously by fitting multi-wavelength data to the theoretical PLZ relations (Marconi et al, 2015; Neeley et al, 2017).

The distance modulus of M4 can be derived by comparing the empirical and calibrated PL relations, as was done in Neeley et al (2017). This results in  $\mu_{[3.6]} = 11.353 \pm 0.095$  mag and  $\mu_{[4.5]} = 11.363 \pm 0.095$  mag, which agrees with the Kaluzny et al (2013) and Braga et al (2015) measurements. Using the exquisite multi-band data available for M4 and described in this chapter, the extinction to M4 can be measured by fitting the distance and extinction law directly to each star as was described in Neeley et al (2015, 2017), finding  $A_V = 1.45 \pm 0.12$  mag using  $R_V = 3.62$  measured directly in the foreground of M4 by Hendricks et al (2012, taking into account M4 is directly behind the  $\rho$  Oph cloud).

## 2.4 Summary

RRLs have been so far excellent standard candles (e.g., Tammann et al, 2008). RRL can be used in individual Galactic structures, extra-galactic systems, and are likely the only relatively-luminous standard candle that can be used to trace ultra-faint galaxies and tidal streams) that populate the Galactic halo (e.g., Fiorentino et al, 2015, 2017; Andrievsky et al, 2018). Although they are typically discovered and classified in the optical, photometry of RRL can be used to determine distances

in a number of passbands, from the optical to the mid-infrared using theoretical and/or empirical calibrations of the RRL PLZ or the FOBE method.

On the theoretical side, current uncertainties in the PL relations come from our lack of perfect knowledge of the evolutionary effects (mixing length, turbulent convection, mass loss, helium abundance), of the input physics (atomic diffusion, extra-mixing, neutrino losses), and of the color-temperature transformations that are adopted to transform bolometric magnitudes and effective temperatures, into the observed magnitudes and colors. Given that theoretical relations are often preferred over empirical ones, these improvements are important.

As demonstrated by the case studies, the distances from the RRL are limited by the incomplete knowledge of the RRL PLZ (in all bands), in particular by the lack of a strong trigonometric parallax calibration. As such, single studies will often apply several calibrations to determine the distance. Studies using RRL are also limited by the imprecise knowledge of the metallicity for individual RRLs, although there are some forms of the RRL PLZ that have only a small dependence on metallicity.

The next generation of large telescopes will permit use of RRLs to distances of  $\sim 5\text{--}6$  Mpc (see e.g., Deep et al, 2011), which have previously only been accessible via Cepheids. The proposed adaptive optics systems for 30-meter class telescopes will be optimized for the NIR wavelengths, which necessitates sound calibration of the NIR PLZ and PWZ relations.

### 3 The type II Cepheids

#### 3.1 Overview

Type II Cepheids (T2Cs) are evolved, low-mass stars (typically  $< 1 M_{\odot}$ ) and have periods between 1 and 100 days, which roughly spans the range between RRLs and Miras (for the former, see the previous section and for the latter see Subramanian et al, 2017). The discovery of T2Cs played a critical role in the establishment of the modern extragalactic distance scale in the 1950s (formalized in the reviews of Baade, 1958b,c, at the seminal Vatican Conference). Before its revolutionizing discovery, the stars adopted to build the PL relation of Cepheids were a mixture of both (i) young, intermediate-mass stars characterized by a radial distribution typical of thin disk stars and (ii) old, low-mass stars with a radial distribution typical of the Galactic halo or bulge. The former are the classical Cepheids of Population-I, while the latter are known as Type-II Cepheids (T2Cs), to further emphasize the difference in age and stellar mass of their progenitors. By discovering the presence of two distinct classes of variables Baade effectively doubled the size (and the age) of the Universe (Baade, 1956; Fernie, 1969) by identifying and resolving a major issue in the determination of the Hubble constant at that time.

The discovery of T2Cs can be considered as one of three seminal discoveries that formed the modern distance ladder, joining (i) the measurement of stellar parallax by Bessel (1871) and (ii) the discovery of the Leavitt Law<sup>7</sup> or PL, first

<sup>7</sup> The consensus of the scientific community present for the *Thanks to Henrietta Leavitt Symposium* held on Nov 8, 2008 was to officially adopt the term ‘Leavitt Law’ for the Cepheid PL relationship. The Council of the American Astronomical Society provided similar advice shortly thereafter. The reader is referred to <https://www.cfa.harvard.edu/events/>

noted by Leavitt (1908) and then quantified by Leavitt and Pickering (1912). For a review of the Leavitt Law, readers are referred to Subramanian et al (2017). After the separation of classical Cepheids and T2Cs, the latter have received far less attention than the former. Nevertheless, there are several good reviews on T2Cs and related objects which are recommended to interested readers: Harris (1985); Wallerstein and Cox (1984); Wallerstein (2002); Sandage and Tammann (2006); Welch (2012); Feast (2010, 2013); Catelan and Smith (2015).

Dating back to almost half a century ago (Wallerstein, 1970), T2Cs have been associated with GGCs characterized by a blue (hot) HB morphology. This means that the HB for these clusters is well populated on the blue tail, which is comprised of hot and extreme HB stars. Roughly one hundred of these variables have been detected in GGCs (Clement et al, 2001a). They have also been observed in stellar systems with complex star formation histories like the Magellanic Clouds (S08; S10, Groenewegen and Jurkovic, 2017a,b) and there are a preliminary identifications in the extragalactic stellar systems with examples being: IC 1613, M 31, M 33, M 106 and NGC 4603 (Majaess et al, 2009). On the other hand, Fornax is the only nearby dSph galaxy for which even a handful of T2Cs have been detected (Bersier and Wood, 2002); if these stars were a signpost for old metal-poor populations, then dSphs, which are home to many RRLs, would be expected to be hosts as well. The paucity of these objects in dSphs has been explained by their lack of blue HB morphologies. However, an observational bias cannot be excluded, since we still lack long-term photometric monitoring for the bulk of distant and diffuse stellar systems, although recent efforts have dramatically improved our variable star census (e.g., Stetson et al, 2014b, among others).

### 3.2 Observed pulsational properties

Example light curves for T2Cs for a wide span of periods are given in Figure 17 using data from OGLE (S08). The T2Cs show a striking degree of variation in comparison to the RRLs (Figure 2), because T2Cs are often divided into subpopulations. The period distribution from S08 is given in Figure 18a and shows three groupings by period. Considering this period distribution, S08 presented a classification scheme for the T2Cs in the LMC using the pulsation properties of the stars, including their amplitudes, light curve shapes, and periods. These pulsation properties are both distance and reddening independent and, thus, are good means for typing the stars. The three groups are divided into the classical sub-types with the following criteria:

1. BL Herculis (or BL Her) with  $1 \leq P \leq 4$  days,
2. W Virginis (or W Vir) with  $4 < P \leq 20$  days,
3. RV Tauri (or RV Tau) with  $P > 20$  days.

The period-amplitude diagram in the  $I$ -band ( $A_I$ ) for the LMC T2Cs is given in Figure 18b with the amplitudes ranging from  $\sim 0.1$  to  $\sim 1$  mag. Figure 18b further demonstrates that there is a set of structure in the period-amplitude diagram similar to what is seen in the Bailey diagram for RRLs (see e.g., Figure 9), albeit the T2C groups are less well defined than the RRLs. In addition to these classical



groupings, S08 have also proposed a new group of T2Cs, the peculiar W Vir (or pW) stars known as pW variables, that display peculiar light curves and are brighter than typical T2Cs at a fixed period; these stars are indicated by open circles in Figure 18b. This classification scheme, however, has not been well settled, because the two minima of the period distribution that drive the definition of the sub-groups depends on the metal abundance and, likely, also on the environment. This means that the quoted period ranges will not universally define the three sub-groups and, thus, further investigations in a more diverse set of objects may yield further sophistication to our sub-classifications.

It is also important to note that different classification schemes have been adopted in different studies throughout the years. For example, General Catalog of Variable Stars<sup>8</sup> (GCVS, Samus et al, 2017) uses a boundary of 8 days to separate the T2Cs, ‘CWA’ for  $P > 8$  days and ‘CWB’ for  $P < 8$  days. In addition, GCVS uses the label ‘RV’ for RV Tau stars for radially pulsating supergiants characterized by the presence of alternating primary and secondary minima. Different schemes were proposed by Joy (1949) and later by Diethelm (1990) that take into account factors beyond the period, such as the light curve shape and spectroscopic features (see also Sandage and Tammann, 2006). Several authors have further suggested that the RV Tau stars are also heterogeneous as a class. While six objects in GGCs have been claimed to be RV Tau stars, some authors have doubted this classification from both the photometric (Zsoldos, 1998) and the spectroscopic point of view (Russell, 1998). The reader should be cautious, when exploring this topic, due to the complexities of these classifications.

### 3.3 Theoretical pulsation predictions

There is a general consensus that T2Cs are in a post-HB phase with a C+O degenerate core with H-shell burning as the main energy source. As is well known, Zero-Age HB stars have a wide range of effective temperatures depending on the total mass (or the envelope mass). After the He exhaustion in the core, they start to climb up in the HR diagram evolving mainly into AGB, but this climb can begin at a range of effective temperatures on the HB. The evolutionary paths of the post-HB phase are predicted to be highly dependent on the ZAHB position. Stars coming from the blue HB tail that go through the IS at luminosities brighter than those of RRL, are found to be pulsating stars and commonly called T2Cs. Calculated evolutionary tracks were pioneered by Gingold (1976, 1977) with Smolec (2016) and Bono et al (2016) providing up-to-date theoretical calculations. However, we still lack a firm understanding of the production routes for T2Cs, in particular specific observational evidence for or against the postulated paths (though, we note that detailed studies such as Groenewegen and Jurkovic, 2017a,b, provide a solid starting point). An interesting question is, for example, the possibility of excursions, first suggested by Schwarzschild and Härm (1970), from the AGB to the hotter side reaching the instability strip. The early investigations Gingold (1976, 1977) suggested such routes (*Gingold nose*) play an important role on explaining a fraction of T2Cs, but such excursions are not expected to take place commonly if at all according to more recent calculations (see Smolec, 2016; Bono et al, 2016).

<sup>8</sup> Available: <http://www.sai.msu.su/gcvs/gcvs/>

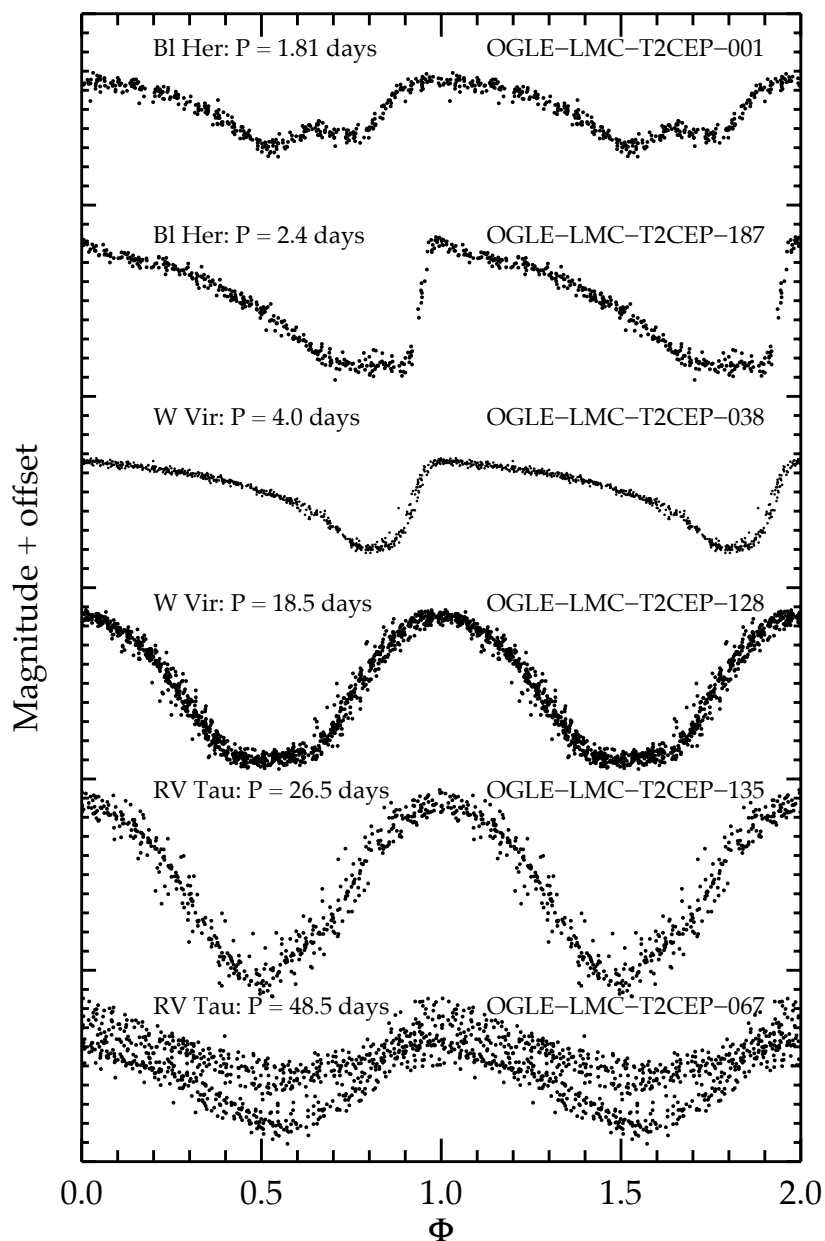


**Fig. 17** Example optical, *I*-band, light curves for T2C in the LMC from the OGLE survey (S08). From top to bottom there are two representative light curves for stars of each of the BL Her, W Vir, and RV Tau classes. The light curves have been normalized to amplitudes of 1 mag to allow comparison of the shapes and structures, with the minor-tick marks being 0.1 mag. The light curve shapes are easily distinguished from those of RRL with similar periods (e.g., Figure 2).

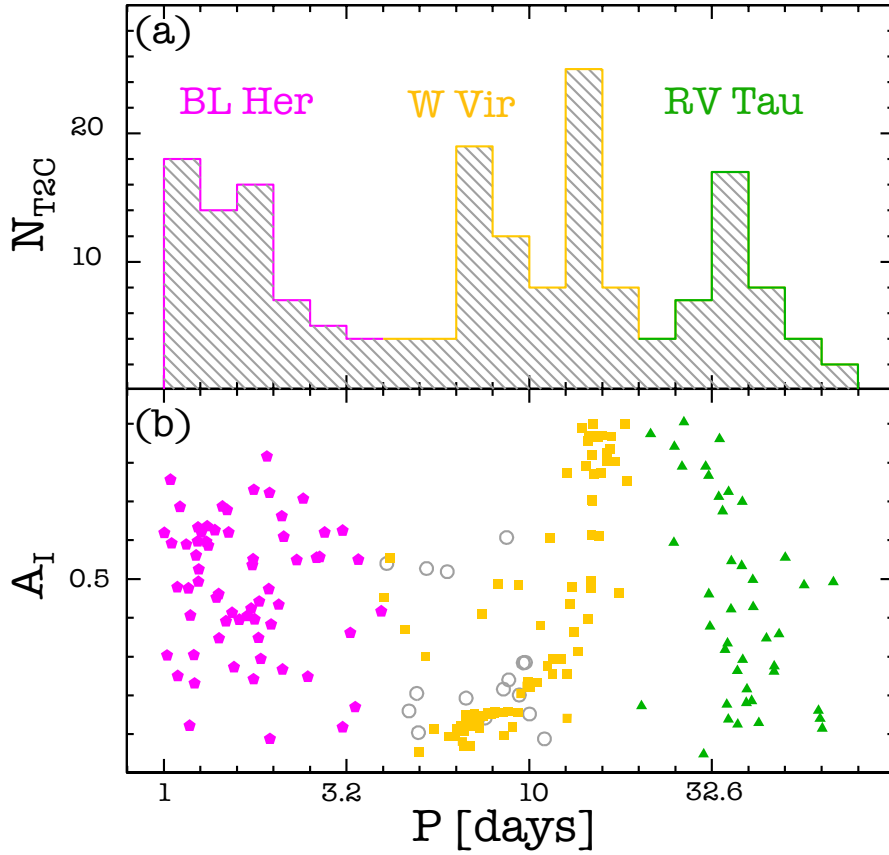


**Fig. 18** Basic properties of the T2Cs as defined in the LMC from the OGLE survey (S08). (a) Period distribution of the T2Cs as divided into the BL Her, W Vir, and RV Tau objects following the S08 classification scheme. (b)  $I$ -band amplitude ( $A_I$ ) versus period diagram (known as the Bailey diagram for the RRLs). The pentagons correspond to BL Her stars, the squares to W Vir stars, the open circles to peculiar W Vir objects, and triangles to RV Tau stars.

In contrast to the RRLs, theoretical investigations of the pulsation properties of T2Cs are quite limited. Early studies based on linear models were discussed by Wallerstein and Cox (1984) together with their period distribution, light- and velocity curves, and their location in the color magnitude diagram. Subsequently, a detailed analysis of T2Cs pulsation properties was performed by Fadeev and Fokin (1985) using non linear radiative models. In particular, Fadeev and Fokin (1985) investigated the modal stability and provided theoretical constraints on the PL relation for T2Cs, but their approach neglected the convective transport and, in turn, the physical mechanism that causes the quenching of radial oscillations. This means that this approach cannot predict the location of the cool (red) boundary of the IS. Using a similar approach, a thorough analysis of the limit cycle stability of T2Cs was presented by Kovacs and Buchler (1988). They have shown that the

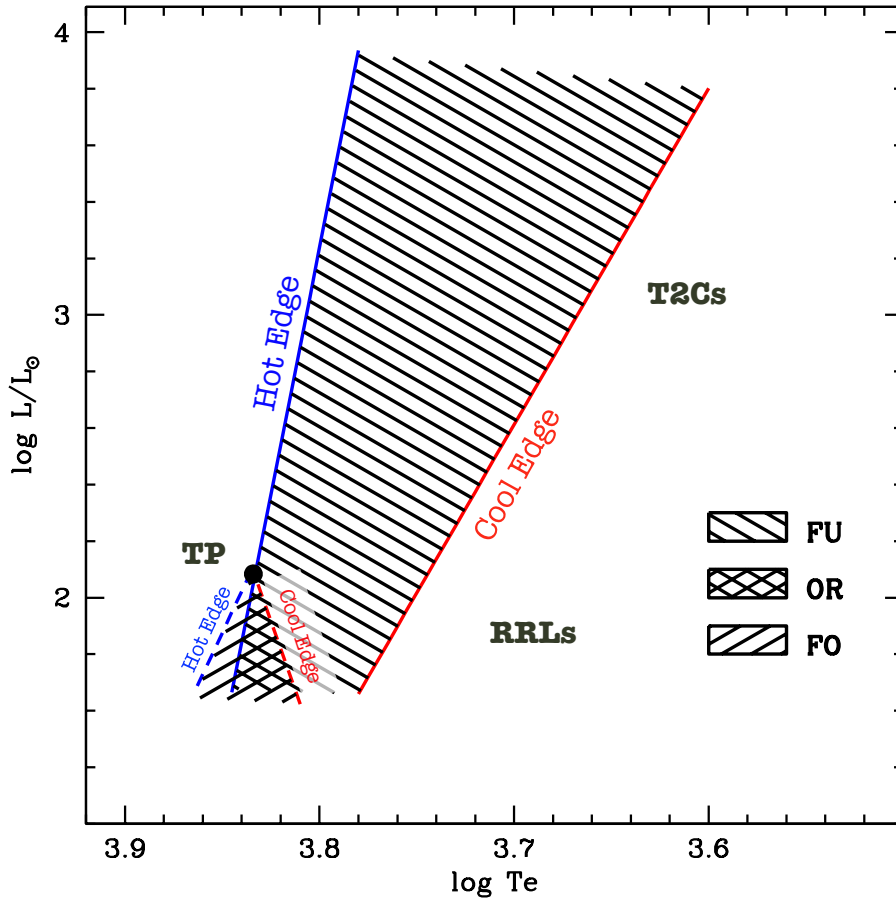


**Fig. 19** Predicted topology of the instability strip in the luminosity and effective temperature range typical of RRLs and T2Cs (Marconi et al, 2015). The the hot and cool edges of the strip are indicated for the FU mode (solid edges), FO mode (dashed edges), and their overlap region (“OR”; double hatched). Stars more luminous than the transition point (“TP”; see the text for definition) do not pulsate in the FO. Only in the region demarcated by the dashed edges can FO pulsators (RRc) attain a stable limit cycle. In the region labeled “OR”, variables can pulsate simultaneously in the FO and in the FU mode (RRd, or mixed-mode pulsators). The region bounded by the solid edges represent the regions where FU pulsators can attain a stable limit cycle. The luminosity for the bulk of the T2Cs excludes them from the FO region.

pulsation behavior changes from single periodic, to period doubling, and eventually to chaotic when increasing the pulsation period.

A more comprehensive theoretical scenario including a time-dependent convective transport was presented for BL Her stars by Bono et al (1997c); Marconi and Di Criscienzo (2007); Di Criscienzo et al (2007). In Bono et al (1997c), a systematic theoretical investigation of T2Cs has shown that fundamental pulsators are primarily expected among this class of variable stars. Moreover, they derived a period–luminosity–amplitude relation and found that it is independent of metallicity for the metal poor regime of  $-2.3 \leq [\text{Fe}/\text{H}] \lesssim -1.5$  that was explored in

the study. These theoretical predictions match quite well the pulsation properties observed for GGCs.

Marconi and Di Criscienzo (2007) presented the full morphology of the theoretical IS for both fundamental and first overtone pulsators and a detailed atlas of both the light and radial velocity curves. Their models confirm that the FO IS is both narrow and limited to faint luminosities, providing new constraints on the *transition point*. The topology of the IS for the luminosity and effective temperature range of the RRLs and T2Cs is given in Figure 19. T2Cs populate the IS at luminosities brighter than the so-called *transition point* (Stellingwerf, 1979). The *transition point* corresponds to the luminosity at which the cool (red) edge of the FO IS matches the luminosity and the effective temperature of the hot (blue) edge of the FU. This means that FO pulsators do not attain a stable limit cycle for luminosities that are brighter and effective temperatures that are cooler than the *transition point*. In consequence, most T2Cs are fundamental pulsators. The first overtones, if any, are only permitted for the low luminosity or short period T2Cs. The empirical evidence, originally brought forward by McNamara (1995) and more recently by S08 and S10 for Galactic and Magellanic T2Cs, confirms that they primarily pulsate in the fundamental mode. There is theoretical evidence that some stability islands for the FO can appear at luminosities brighter than the *transition point*, but their true nature needs to be further clarified (Marconi et al, 2015). Furthermore, the FO IS tends to vanish in the metal-rich regime (e.g.,  $[\text{Fe}/\text{H}] \sim -1.0$ ). Finally, using these same pulsation models and the evolutionary tracks from Pietrinferni et al (2004), Di Criscienzo et al (2007) derived analytical relations for the boundaries of the IS as a function of the adopted stellar parameters, as well as the PL and PW relations for these objects. They derived the T2C-based distances to GGCs and concluded that there is good agreement with the distance scale set by the RRLs.

Similarly to what happens for classical Cepheids, the PL relation for T2Cs can be derived using the fundamental pulsation relation given in Equation 1 (van Albada and Baker, 1971) valid for radial pulsators, together with the mass–luminosity relation typical of low-mass AGB evolutionary models (e.g., for BL Her stars, Di Criscienzo et al, 2007). Indeed, these AGB pulsators follow an inverse relation between stellar mass and luminosity, since lower mass pulsators are crossing the IS at a luminosity brighter than those with larger masses (Bono et al, 2016). The pulsation relation can then be averaged in temperature because the width of the IS is quite narrow ( $\sim 1500$  K), originating a PL relation (see also Fadeev and Fokin, 1985; Matsunaga et al, 2006). Interestingly enough, the slope of the overall PL for T2Cs is less steep than that of classical Cepheids, which is also predicted by theoretical models (e.g., Bono et al, 1999; Di Criscienzo et al, 2007).

### 3.4 Optical and near-IR period–luminosity and period–Wesenheit relations

It has long been recognized that T2Cs follow, at least, a loose PL relation. From previous studies on T2Cs in GGCs, it is known that the T2Cs do follow a PL in  $BVI$ . However, the relation has not been well established until recent work. While Harris (1985) and McNamara (1995) claimed that the optical PL slopes become steeper at around  $\log P = 1$ , Pritzl et al (2003) did not find such a feature for the T2Cs in NGC 6388 and NGC 6441 based on *HST* photometric data. As Pritzl

et al (2003) claimed, many earlier studies for the T2Cs were based on magnitudes determined from photographic plates and, from these earlier works, it had been unclear if this class were useful as a distance indicator.

Breakthroughs were brought by modern photometric surveys in both the optical and the infrared. In particular, large-scale microlensing surveys that started in the late 1990s have systematically discovered T2Cs in the Magellanic Clouds. In the MACHO microlensing survey, Alcock et al (1998) determined that W Vir and RV Tau sub-types follow a PLC relation in the form of

$$M_V = a + b \log P + c(V - R) \quad (18)$$

with a relatively small scatter of 0.15 mag, which is identical (c.f. Bono and Marconi 1999) to a PW relation of the form,

$$V - c(V - R) = a + b \log P. \quad (19)$$

The photometric analysis performed by S08 using  $VI$  optical data from the OGLE survey provided solid, empirical optical PL relations that support the theoretical predictions. The LMC sample is larger than the samples in GGCs and, because they are in the same system, can be studied as an ensemble without uncertainties from distances to the individual clusters. Figures 20a and 20b show the period-luminosity distribution for the T2Cs from S08 for the  $I$  and  $V$  bands, respectively; the BL Her stars are shown as filled hexagons, the W Vir as filled squares, and the RV Tau stars as filled triangles, while the pW stars are removed (following the classification by S08). The PL relations can be fit in three ways:

1. First, a linear regression can be performed for the entire sample, which results in the following relations,

$$\begin{aligned} M_V &= 19.01 - 2.07 \log P \quad (\sigma_V = 0.6), \\ M_I &= 18.37 - 2.29 \log P \quad (\sigma_I = 0.4). \end{aligned} \quad (20)$$

A linear regression over the entire period range shows a decrease of the dispersion from  $\sim 0.6$  to  $\sim 0.4$  mag when moving from the  $V$  to the  $I$  band, indicating that the scatter decreases for longer wavelengths.

2. As is evident in Figures 20, the PL relations for T2Cs in these photometric bands are far from being linear and they could be better represented by a higher order fit, more specifically a polynomial quadratic in  $\log P$ . Fitting this form of the PL to the S08 data results in the following fits,

$$\begin{aligned} M_V &= 18.58 - 0.34 \log P - 1.03 (\log P)^2 \quad (\sigma_V = 0.5), \\ M_I &= 18.06 - 1.04 \log P - 0.74 (\log P)^2 \quad (\sigma_I = 0.3). \end{aligned} \quad (21)$$

This reduces the scatter by 0.1 mag, corresponding to improvements in distance precision by 5 %.

3. As has been done in previous works, we also consider excluding RV Tau stars from the sample, because they show a larger spread in luminosity at fixed period for all wavelengths. Effectively, this is a cut in period for the S08 sample to those stars with  $P \leq 20$  days. Fitting a linear relation over this period range results in the following,

$$\begin{aligned} M_V &= 18.78 - 1.57 \log P \quad (\sigma_V = 0.5), \\ M_I &= 18.20 - 1.94 \log P \quad (\sigma_I = 0.3). \end{aligned} \quad (22)$$

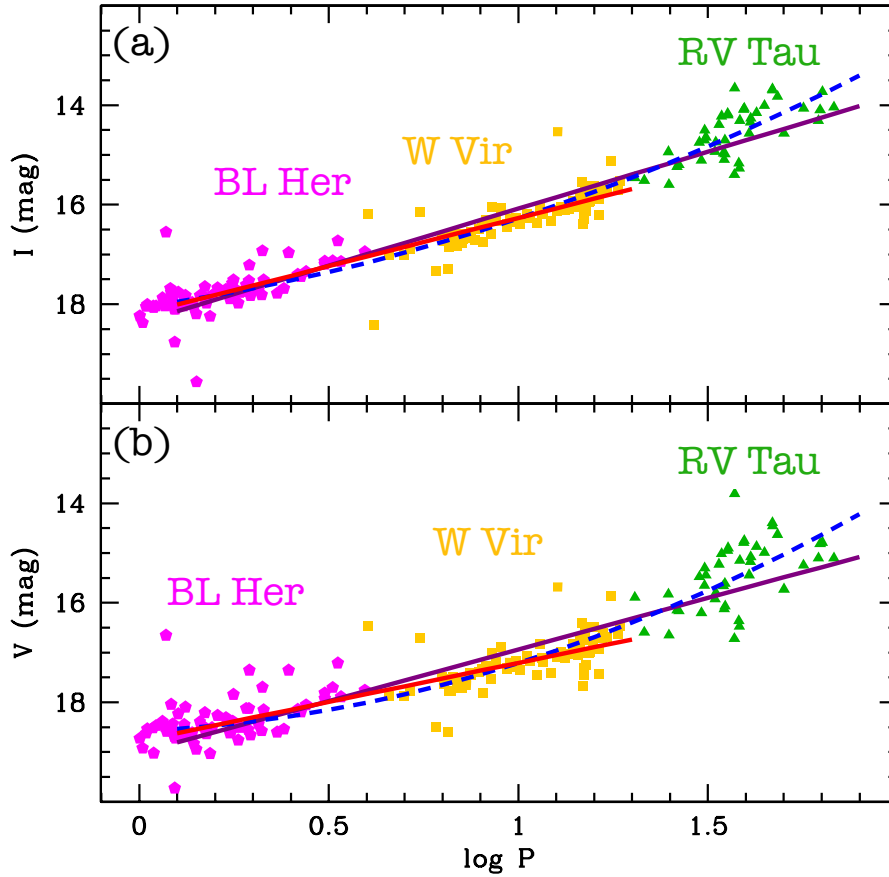


**Fig. 20** The PL relations for T2Cs in the LMC: (a)  $I$ -band and (b)  $V$ -band PL relations. The S08 T2C classification is maintained, but the peculiar W Vir stars are removed. The three PLs discussed in the text are shown for both panels: (i) a linear global fit for all three sub-types (solid line; Equation 20), (ii) a quadratic global fit that better accounts for the structure of the RV Tau types (dashed line; Equation 21), and (iii) a linear fit just to the BL Her and W Vir type stars (solid line; Equation 22).

However, it is noteworthy that the scatter of these relations and those of the quadratic fits for all three sub-types are similar. Exploration of additional systems with different metallicities and in different environments may help distinguish which of the relations is more representative for a larger range of properties.

One has to keep in mind the presence of peculiar T2Cs that are scattered above the PL relation for BL Her and W Vir type T2Cs. They have some distinctive characteristics compared to W Vir stars (e.g., light curve shapes) but otherwise may be difficult to distinguish without long term monitoring. Soszyński et al (2017) further investigated the light curves of this pW group. A significant fraction of the pW stars identified by S08 and S10 were found to be in eclipsing binary systems. These objects are interesting in terms of evolutionary paths to produce T2Cs (and

related objects), but to obtain accurate distances to stellar systems with T2Cs these atypical objects need to be identified and then excluded.

There is also evidence that T2Cs display well defined NIR PL relations that are linear over the entire period range. Matsunaga et al (2006) reported relations with a scatter of 0.15 mag in  $JHK_s$  for BL Her to RV Tau stars in GGCs. Because they used RRL-based distances to individual GGCs to combine T2Cs onto the single relation, the well-defined relations suggest some consistency with the RRL distance scale. Ripepi et al (2015) found smaller dispersions in both the  $J$  (0.13 mag) and  $K$  (0.09 mag) for T2Cs in the LMC, further supporting the evidence that they are good distance indicators. Recent updates on the NIR relations based on a larger photometric sample can be found in Bhardwaj et al (2017a,b).

The slopes of these NIR PL relations do not change dramatically over the metallicity range spanned by these observations, as shown by Figure 21 that displays the values for  $JHK$  PL relations obtained from GGCs (Matsunaga et al, 2006) and the LMC (Ripepi et al, 2015). Spectroscopic measurements are still too limited to draw firm conclusions (only a few dozen have measurements); those stars with metallicity measurements, however, span a range of metallicities similar to that of RRLs. The agreement becomes more stringent if we account for the theoretical NIR PL relations provided by Di Criscienzo et al (2007), which are shown in Figure 21 as the open circles. Note that a similar agreement is also found in a detailed comparison of the zero-points. Theoretical work, however, suggested a dependence of the zero-point on the metal content at the level of 0.04 to 0.06 mag dex<sup>-1</sup>. Observations, on the other hand, suggest a minimal, if any, dependence (Matsunaga et al, 2006). A different result is found when considering the T2Cs in the SMC (Ciechanowska et al, 2010); more specifically, the slopes are shallower with  $-1.95$  in the  $J$ -band ( $\sigma_J = 0.24$  mag) and  $-2.15$  in the  $K$ -band ( $\sigma_K = 0.2$  mag). However, the difference with the slopes shown in Figure 21 is within the associated  $1 \sigma$  errors, and it is probably due to the high scatter of the mean NIR magnitudes derived from single epoch observations in Ciechanowska et al (2010). In addition, the NIR sample of T2Cs in Ciechanowska et al (2010) includes only 50% of the total optical sample for the SMC (40 objects, S10) and thus a more complete sample with more well-sampled light curves may resolve the discrepancy.

The use of empirical relations to determine the LMC distance employed by Ripepi et al (2015) returned a distance modulus in excellent agreement with RRLs, but with a difference of  $\sim 0.1$  mag with respect to the distance modulus based on classical Cepheids (**most likely due to parallax sample used, see Section 5.2**). Even though this is not a statistically significant difference (e.g., within the formal  $1 \sigma$  uncertainty), it suggests a possible population bias in the LMC distances (Inno et al, 2016). Theoretical models for the BL Her period range are in extremely good agreement with the above evidence, since they predict dispersions in these passbands equal to  $\sigma_J = 0.13$  mag and  $\sigma_K = 0.06$  mag (Di Criscienzo et al, 2007).

Matsunaga et al (2006) also pointed out that the T2Cs and RRLs seem to follow the same, or continuous, PL relations in the infrared. The fact that RRLs and T2Cs follow very similar NIR PL relations (see also Feast, 2011) seems to be supported by the smooth and natural transition of the evolutionary properties of evolved RRLs and BL Her type stars. Although it was also discussed that BL Her and W Vir stars could have distinct NIR PL relations, recent findings based on accurate NIR mean magnitudes for LMC T2Cs suggest they are, within the errors,



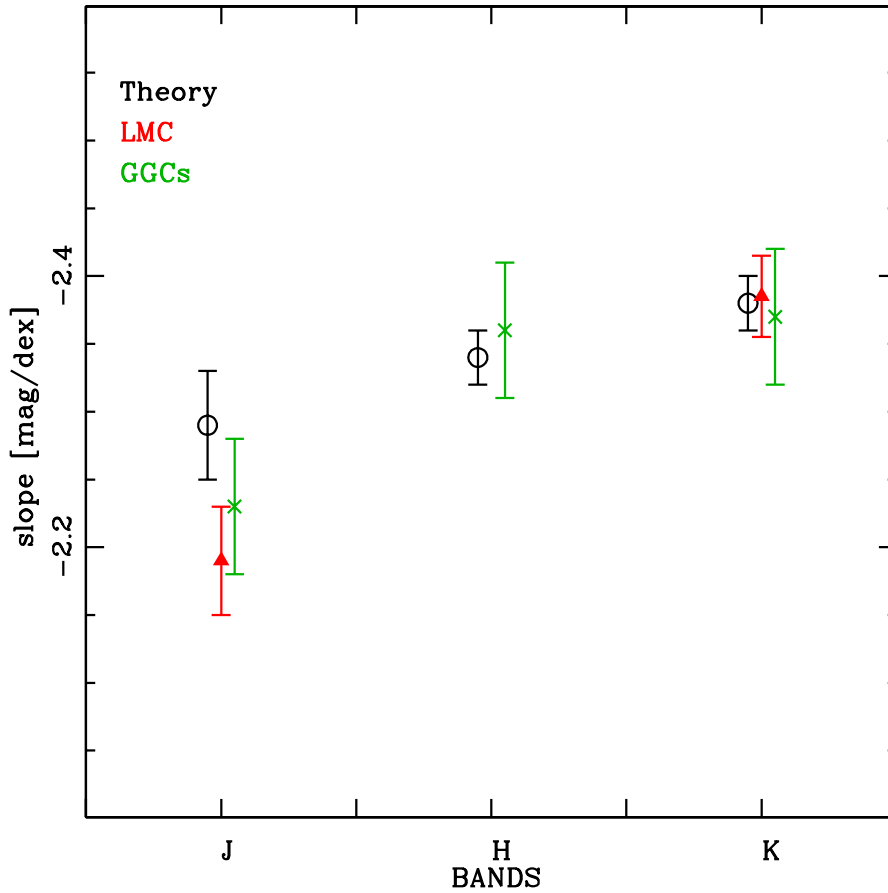


**Fig. 21** Observed slopes of NIR ( $JHK$ ) PL relations for T2Cs in GGCs (xes, Matsunaga et al, 2006) and in the LMC (triangles, S08). The slopes predicted by (Di Criscienzo et al, 2007) are plotted as open circle. The vertical bars display the uncertainties on the slopes.

very similar (Ripepi et al, 2015, and references therein). This does not apply to RV Tau variables, because they typically display a larger spread compared to W Vir and BL Her stars. The increase in the spread might also mask a possible change in the slopes of the NIR PL relations (Ripepi et al, 2015). This occurrence appears to be associated with the properties of the circumstellar envelopes typical of these variables, which may also contribute to the larger scatter for this sub-type observed in the optical bands (see Figure 20).

PW relations are also commonly used to reduce the impact of extinction in distance determination and here we derive these for T2Cs based on the most conspicuous samples available in literature (see also Bhardwaj et al, 2017a).

1. The most common Wesenheit magnitude in the optical takes the form of  $W(I, V - I) = I - 1.55(V - I)$ . Performing a linear regression to the BL Her

and W Vir stars we find:

$$\begin{aligned} W(I, V - I)_{\text{LMC}} &= 17.31 - 2.50 \log P + \mu_0(\text{LMC}) \quad (\sigma = 0.2), \\ W(I, V - I)_{\text{SMC}} &= 17.63 - 2.71 \log P + \mu_0(\text{SMC}) \quad (\sigma = 0.4), \end{aligned} \quad (23)$$

for the LMC (S08) and SMC (S10) data, respectively. To compare the relations on the absolute scale, we assume the consensus distance moduli,  $\mu_0(\text{LMC}) = 18.49$  mag (de Grijs et al, 2014, and references therein) and  $\mu_0(\text{SMC}) = 18.96$  mag (de Grijs and Bono, 2015, and references therein), respectively (see also de Grijs et al, 2017, in this series). Figure 22a compares these  $W(I, V - I)$  relations. It is worth noticing that when decreasing the host galaxy metallicity (from that of the LMC to that of the SMC), the slopes get steeper and the dispersion around the mean relation increases, although the difference of slopes is still within  $1 \sigma$ .

2. The most common NIR Wesenheit magnitude takes the form of  $W(K, J - K) = K - 0.69(J - K)$ . Performing a linear regression to the BL Her and W Vir type stars for the LMC (as given by Ripepi et al, 2015), SMC (IR magnitudes and periods from Ciechanowska et al, 2010) and GGCs (data from Matsunaga et al, 2006), we find the following PW relations:

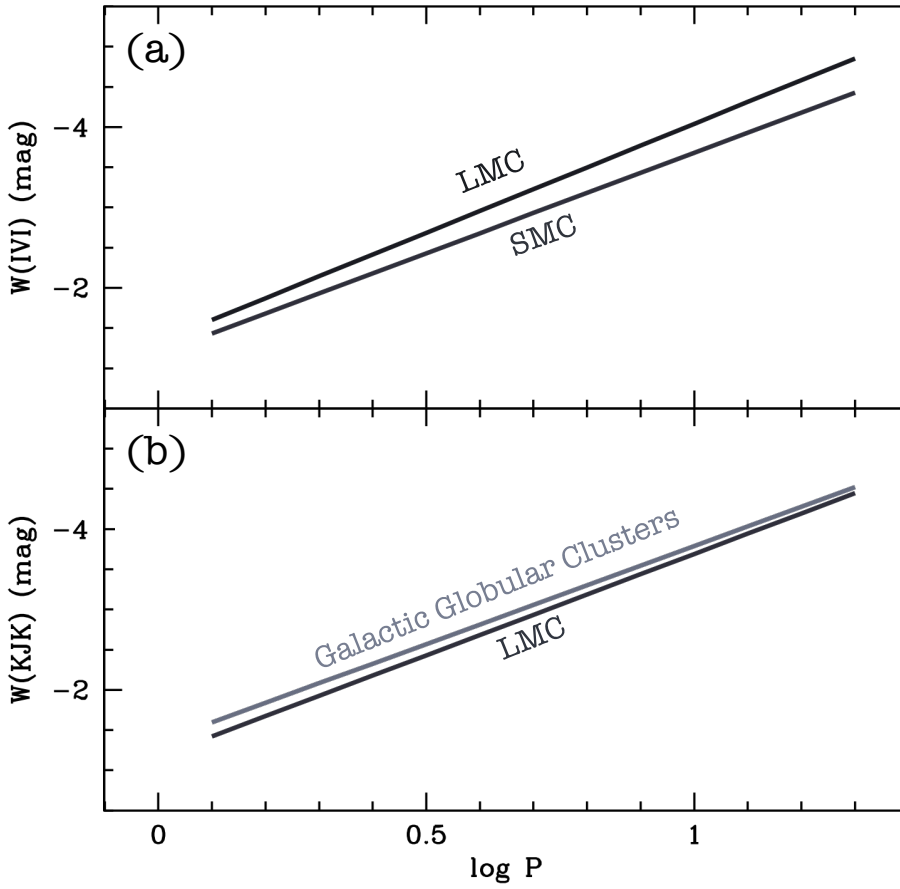
$$\begin{aligned} W(K, J - K)_{\text{LMC}} &= 17.32 - 2.52 \log P + \mu_0(\text{LMC}) \quad (\sigma = 0.08), \\ W(K, J - K)_{\text{SMC}} &= 17.41 - 2.17 \log P + \mu_0(\text{SMC}) \quad (\sigma = 0.3), \\ W(K, J - K)_{\text{GGCs}} &= -1.35 - 2.44 \log P \quad (\sigma = 0.2). \end{aligned} \quad (24)$$

Figure 22b compares NIR PW relations; the SMC relation is not included because the mean magnitudes have a large dispersion about the relation due to sparse sampling of the NIR light curve. As shown in Figure 22b, the slopes for LMC and GGCs are very similar, suggestive of only a mild dependence on the metal content. However, for the SMC we note that the slope decreases down to  $-2.17 \text{ mag dex}^{-1}$ , which is opposite to what happens in the optical regime. There are no doubts that a more detailed investigation of T2Cs in the SMC will be crucial to understand the universality of the NIR PW relations.

### 3.5 T2Cs in context with RRLs and CCs

In this section we discuss the pulsation and evolutionary properties of T2Cs as compared to the most popular distance indicators, namely RRLs and classical Cepheids. The aim is to highlight their possible new role for these stars in the *Gaia* era that is expected to refine the extragalactic distance scale. In the following, we list their properties and assess their advantages and disadvantages compared to classical Cepheids and RRLs:

1. *NIR PL relation*: As discussed in the previous section, T2Cs follow well defined optical and NIR PL relations (Matsunaga et al, 2006, 2013). Moreover, there is evidence that their pulsation properties are either independent of, or minimally affected by, the metal abundance (Bono et al, 1997c; Di Criscienzo et al, 2007; Lemasle et al, 2015a). RRLs also follow linear NIR PL relations, however their luminosity (and luminosity range) is much smaller, which largely limits their application to within the Local Group (e.g., distances up to  $\sim 1$  Mpc). T2Cs are



**Fig. 22** (a) Optical ( $I,V - I$ ) PW relations for T2Cs in the LMC and SMC derived as described in the text using data taken from (S08) and (S10), respectively. (b) NIR ( $K,J-K$ ) PW relations for T2Cs. The LMC data is adopted from Ripepi et al (2015), whereas the for GGCs it has been derived using NIR magnitudes from Matsunaga et al (2006). The precise form of the relations is given in Equations 23 and 24 and described in the text.

roughly 1.5 mag fainter than classical Cepheids at fixed period with the precise difference being period dependent. Moreover, the long period tail of classical Cepheids exceeds 100 days, while the long period tail of T2Cs approaches  $\sim 70$  days.

2. *Linearity:* The current empirical evidence indicates that BL Her and W Vir stars follow NIR PL relations that are linear over the entire period range. With current data, however, it is unclear if RV Tau objects follow a long period extension of the same PL relations, or whether their PL relation is distinct. Thus, RV Tau subgroup is typically neglected when fitting PL relations and in determining distances.
3. *Brightness:* T2Cs are brighter than RRLs and cover a similar magnitude range as Classical Cepheids. The difference with RRLs ranges from at least half magnitude ( $M_V \sim -0.5 / -1$  mag) to roughly three magnitudes ( $M_V \sim -3$  mag).

This means that they can be employed to measure distances and trace old (blue HB) stellar populations beyond the Local Group.

4. *(Short) Evolutionary Lifetime:* T2Cs are typically approaching the AGB phase. This means that their evolutionary time scale is roughly two orders of magnitude faster than RRLs (Marconi et al, 2015; Bono et al, 2016). RRLs are low-mass stars during their core He burning phase, they have been identified in all stellar systems hosting stellar populations older than  $\sim 10$  Gyr, and from a theoretical point of view stellar mass and chemical abundance ranges that can give origin to RRLs are well known (Bono et al, 1996, 1997a,b). The same is true for classical Cepheids, that are young core helium burning stars. The ratio of evolutionary times of classical Cepheids to the entire lifetime of their progenitors is longer than for T2Cs (Marconi et al, 2005a). This has a strong impact on the occurrence of T2Cs in a given system such that T2Cs are more rare than both RRLs and classical Cepheids. As shown in Figure 1a, the LMC contains  $\sim 3,000$  classical Cepheids,  $\sim 20,000$  RRLs, but only  $\sim 200$  T2Cs (Fiorentino and Monelli, 2012).
5. *Binary or Evolutionary Channel:* The fraction of T2Cs in binary systems is not well constrained. Very recently Soszyński et al (2017) and Soszyński et al (2018) presented additional monitoring of T2Cs in the LMC and in the Bulge that find new irregularities in the light curves consistent with binary companions. Maas et al (2002) present evidence that several RV Tau stars may be in binary systems. More importantly, there is photometric evidence that the pW stars may also be binaries (most recently Pilecki et al, 2017). This working hypothesis is also supported by spectroscopic evidence of binary companions for some T2Cs (Maas et al, 2007; Soszyński et al, 2010; Jurkovic et al, 2016) and, in turn, casts some doubts on the proposed small initial mass of their progenitor stars. These kind of objects have been dubbed *Binary Evolution Pulsators* (Karczmarek et al, 2016, 2017b). Long term monitoring of T2Cs can help identify their evolutionary path and determine if binary formation is the dominant formation path. Period changes can tell us the directions of evolution within the instability strip and this, in turn, provides additional evidence for the evolutionary paths of T2Cs (e.g, Diethelm, 1996; Wallerstein, 2002; Rabidoux et al, 2010).
6. *Shape of the light curve:* The coupling between shape of the light curve, e.g., the Fourier parameters and luminosity amplitudes, and the pulsation period is less distinctive for T2Cs than for RRLs (e.g., compare Figure 17 to Figure 2 for light curves and Figure 18 and Figure 9 for the amplitude-magnitude diagrams). They partially overlap with classical Cepheids (S08).
7. *Host stellar systems:* T2Cs have been identified in a variety of stellar systems hosting an old ( $t \geq 10$  Gyr) stellar population, e.g., both early and late type stellar systems. Although this appears as a solid empirical evidence, we still lack firm identification of T2Cs in dSphs. The lack of T2Cs in dSphs can hardly be explained as an observational bias, since they are systematically brighter than RRLs and some of the classical dSphs have been surveyed for very long time scales (e.g., Stetson et al, 2014a; Coppola et al, 2015; Martínez-Vázquez et al, 2016b, among others). The working hypothesis suggested by Bono et al (2011, 2016) to explain the desert of T2Cs in dSphs is that they typically lack hot and extreme HB stars (Salaris et al, 2013). This means that the fraction of HB stars evolving from the blue (hot) to the red (cool) side of the CMD is

small. This is relevant, given that the stellar populations of dSphs do cover the same metallicity range of GGCs that do have well extended blue tails on the HB. The lack of hot/extreme HB stars, and in turn of T2Cs, may be due to an environmental effect between dSphs and GGCs, that otherwise are composed of similar stellar populations.

On the whole, T2Cs have many enticing properties and show potential as distance indicators, but also still have some more shadowy areas left to be resolved before their application en masse.

### 3.6 Summary and final remarks

In this section, the observational and theoretical properties of T2Cs have been described. Although there is no doubt that they are radially pulsating stars crossing the IS, their evolutionary origin has not yet been completely addressed (e.g., the **Binary Evolution Pulsator scenario**, see Karczmarek et al, 2016, 2017a). Both theoretical and observational studies demonstrate that T2Cs mainly pulsate in the fundamental mode, given that they reach luminosities brighter than the *transition point*. The possible occurrence of short-period, fainter T2Cs evolving along the so-called *blue hanger* (Bono et al, 2011) cannot be excluded. However, they are expected to add little contamination to the fundamental mode NIR PL and PW relations.

T2Cs are *largo sensu* solid distance indicators, for they follow well defined optical and NIR PL relations, and both theoretical and empirical results suggest a minimal dependence on metal-abundance. Furthermore, they also follow similar optical and NIR PW relations. The key advantages of these diagnostics is to be independent of reddening uncertainties, but rely on the assumption that the reddening law is universal. This further suggests that T2Cs can be considered *stricto sensu* ideal distance indicators, given that they can provide very accurate relative distances, independent of uncertainties in the zero-point of the PL relations. The small metallicity dependence of the slopes of the NIR PW relations further supports the use of these variables as distance indicators for stellar systems affected by differential reddening (e.g., as with M 4 in Braga et al, 2015). To obtain the tighter PL relations, only BL Her and W Vir stars (i.e., those T2Cs with periods less than 20 days and  $M_V$  fainter than  $-2$  mag) are considered, excluding the brighter RV Tau objects. This means that one can detect and employ T2Cs as distance indicators out to  $\sim 10$  Mpc with *HST* (limiting magnitude  $V \sim 30$  mag). However, because their periods have a wide distribution ranging from a few days to 20 days, complete photometric surveys with long temporal baseline have to be conducted in order to collect complete T2C samples.

The absolute distance scale of T2Cs, i.e., the zero point of the PL relation, is calibrated using the populations in the Magellanic Cloud and GGCs. There are only a handful of trigonometric parallax measurements for T2Cs and the uncertainties for the measurements that do exist make it difficult to establish a distance scale directly tied to parallax. The uncertainties affecting the zero-points of these relationships, and in turn, the absolute distances based on T2Cs, are going to be largely reduced during the next few years. This is thanks to the very accurate trigonometric parallaxes that will be provided by *Gaia*, not only for the nearest

T2Cs, but for more than 100 field T2Cs and at least a dozen in nearby GGCs using end-of-mission predictions (Harris, 1985; Matsunaga et al, 2006).

The observational outlook concerning T2Cs appears even more promising if we take account of the fact that *JWST* will be capable of producing a complete census of T2Cs for Local Group and Local Volume galaxies. The halos of large galaxies are, indeed, marginally affected by crowding problems. Moreover, 30 meter-class telescopes will provide a unique opportunity to trace old stellar populations in the bulges and the innermost regions of galaxies in the Local Volume due to their unprecedented spatial resolution (Bono et al, 2017).

#### 4 The Tip of the Red Giant Branch

The ultimate origin of the tip of the red giant branch (TRGB) as a standard candle is the canonical work of Baade (1944), who used red-sensitive plates to first resolve the stellar populations in early-type stellar systems, M 32, NGC 205 and the central region of M 31. From these observations developed the concept of the stellar classes of Pop I and Pop II. Baade also concluded that the brightest stars in these objects had similar magnitudes and colors. Sandage (1971) later pointed out that galaxies in the Local Group invariably contained a background sheet of red stars. Comparing the Cepheid distances to three Local Group galaxies, M 31, M 32, and IC 1613, he determined a mean absolute magnitude of the brightest red stars to be  $M_V = -3.0 \pm 0.2$  mag. This work led to the early applications using RGB stars for distance determination in the early eighties (see a summary in Lee et al, 1993).

A formal method to detect the TRGB in color-magnitude-diagrams (CMDs) of galaxies, a calibration and a thorough analysis of its uncertainties were first published by Lee et al (1993) and Madore and Freedman (1995), respectively. More specifically, Lee et al (1993) compared empirical RGB loci for 6 GGCs (Da Costa and Armandroff, 1990) with theoretical stellar evolutionary tracks (Yale Models, Green et al, 1987), and concluded that the *I*-band absolute magnitude of the TRGB is accurate to  $\pm 0.1$  mag for resolved stellar systems of low metallicity (e.g.,  $[\text{Fe}/\text{H}] < -0.7$ ). Lee et al (1993) introduced Sobel “edge detection” kernels for detecting the discontinuity caused by the TRGB in *I*-band luminosity functions and this methodology was rigorously tested by Madore and Freedman (1995). Since those works, the TRGB has been used extensively in Pop II dominated systems. With current observational capabilities the TRGB can be used to determine distances out to  $\sim 20$  Mpc (see e.g., Jang and Lee, 2015, 2017a; Jang et al, 2018, and references therein). Indeed, several authors have discussed the TRGB as an alternative to CCs for the basis of the extragalactic distance scale (e.g., Mould and Sakai, 2008; Beaton et al, 2016). So far, more than 400 galaxies have been measured their distances with the TRGB (Tully et al, 2016).

The TRGB as a precise distance indicator for resolved stellar systems has held against several observational tests (Lee et al, 1993; Ferrarese et al, 2000; Bellazzini et al, 2001; Sakai et al, 2004). Several studies have shown that the TRGB distance estimates to nearby galaxies agree well with those based on other precise distance indicators, such as CCs, RRLs, and Megamasers (Freedman, 1988; Lee et al, 1993; Sakai et al, 2004; Ferrarese et al, 2000; Tammann et al, 2008; Mager et al, 2008;

Freedman and Madore, 2010; Jang and Lee, 2017b). It indicates that the precision of the TRGB is comparable to those of other primary distance indicators.

In this section, physical understanding of the TRGB is given in Section 4.1. Section 4.2 discusses empirical methods to measure the TRGB. A case study of using TRGB in the optical is described in Section 4.3. In Section 4.4, the IR properties of the TRGB are discussed. We conclude looking to future improvements of the method in Section 4.5.

#### 4.1 Physical Description

The TRGB corresponds to the termination of the RGB evolution in old stellar populations, due to the onset of the He-flash in the electron degenerate cores of low-mass stars. For a given initial chemical composition, the bolometric luminosity of the TRGB is determined by the He-core mass at the He-flash. This mass is basically constant, e.g., within a few  $0.001M_{\odot}$ , for stellar masses that reach He-ignition at ages from 1.5-3 Gyr to the age of the Universe (the starting age is a function of the initial metallicity).

The use of the TRGB for distance estimates has been traditionally based on *I*-band photometry, in the implicit assumption that the observed RGB of a galaxy has an age comparable to the age of GGCs, or in any case larger than 4-5 Gyr and metallicity  $[M/H]$  below  $\sim -0.7$  (see, e.g., Da Costa and Armandroff, 1990; Lee et al, 1993; Salaris et al, 2002). In this age range  $M_{bol}^{TRGB}$  is roughly constant for a given  $[M/H]$ , but becomes brighter with increasing  $[M/H]$ . Two effects influence  $M_{bol}^{TRGB}$  in more metal rich stars: (i) increased efficiency of the hydrogen burning shell, which makes the stars brighter, and (ii) decreasing He-core mass, which makes the stars fainter; overall,  $M_{bol}^{TRGB}$  is more luminous in metal-rich stars from these two effects. At the same time the effective temperature of the TRGB decreases with increasing  $[M/H]$  and the bolometric corrections,  $BC_I$ , decrease with decreasing  $T_{eff}$ . The resulting rate of decrease of  $BC_I$  with increasing metallicity very nearly matches the rate of increase of  $M_{bol}^{TRGB}$  with  $[M/H]$ . Given that  $M_I^{TRGB} = M_{bol}^{TRGB} - BC_I$ , this implies that  $M_I^{TRGB}$  stays almost constant with  $[M/H]$  for the range between  $\sim -2.0$  and  $\sim -0.7$  and for ages older than 4-5 Gyr.

From the variation of the absolute magnitude from theoretical models, it follows that applying a single-value for the absolute magnitude of the TRGB to galaxies with an extended star formation history can cause large systematic errors. Adopting a single value in a system assumes that the RGB stars in these galaxies are *all* older than 4-5 Gyr with  $[M/H] < -0.7$ , which can only be assumed safely in specific conditions. This effect has been studied theoretically by Barker et al (2004), Salaris and Girardi (2005), Cassisi and Salaris (2013), and also verified empirically by Górski et al (2016). A recent, detailed study is given in Serenelli et al (2017).

Figure 23 displays a theoretical  $M_I^{TRGB} - (V - I)^{TRGB}$  calibration in Johnson-Cousins filters using the Pietrinferni et al (2004, BaSTI) stellar evolution models after correcting the TRGB bolometric magnitudes for the effect of including the updated electron conduction opacities by Cassisi et al (2007) and using the empirical bolometric corrections by Worthey and Lee (2011). In Figure 23  $[M/H]$  lower(larger) than  $-0.65$ , are displayed with open(filled) circles, respectively. The BaSTI theoretical models cover a range of metallicity  $[M/H]$  between  $-2.2$  and

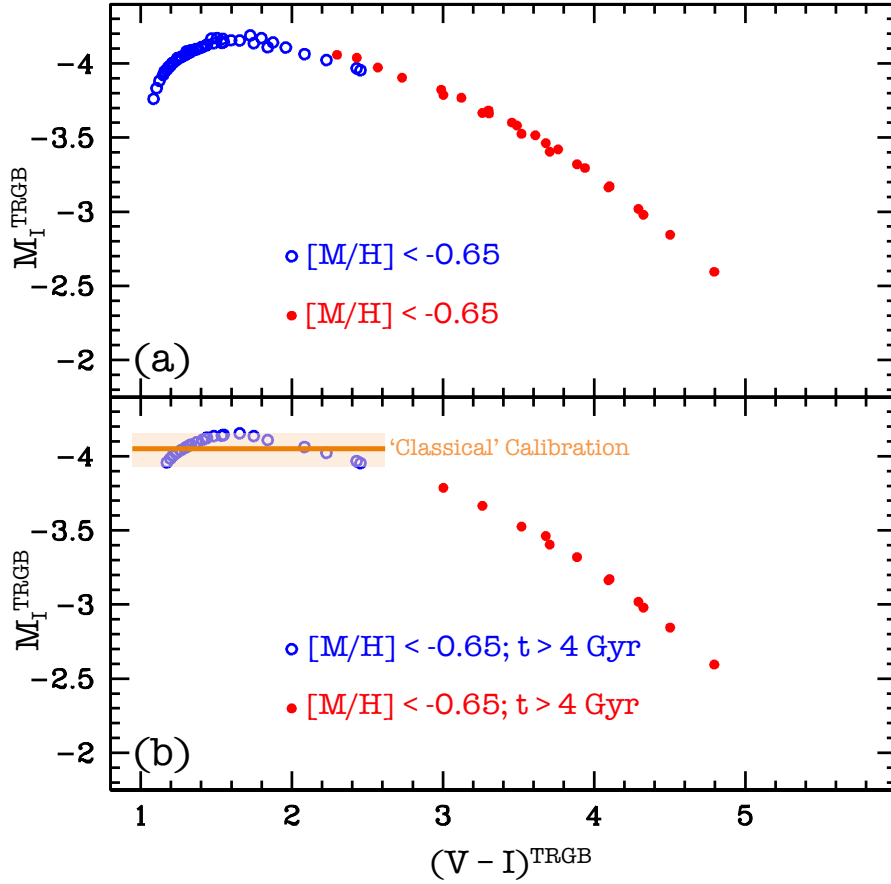


**Fig. 23**  $M_I^{TRGB} - (V - I)^{TRGB}$  distribution for the TRGB from theoretical models from BaSTI (Pietrinferni et al, 2004). (a) The full range of ages ( $1.5 < t < 14$  Gyr) and metallicity ( $-2.2 < [M/H] < 0.3$  dex) for the models and (b) only models with ages older than 4 Gyr. In both panels, the blue open circles are for  $[M/H] < 0.65$  dex and the red filled circles are for  $[M/H] > 0.65$  dex. The solid orange line represents the empirical calibration of  $M_I^{TRGB} = -4.05$  mag (Lee et al, 1993; Salaris and Cassisi, 1997; Tammann and Reindl, 2013), with the shading giving the typical uncertainty of  $\pm 0.10$  mag. The ‘classical’ calibration is a reasonable approximation to the theory for stars in this age and metallicity range (corresponding to V-I from 1.0 to 2.5 mag).

0.3 and ages between 1.5 and 14 Gyr. The full age and metallicity range of the models is shown in Figure 23a, which demonstrates that decreasing age at constant  $[M/H]$  pushes  $M_I^{TRGB}$  to bluer colors, whereas increasing  $[M/H]$  at fixed age has the opposite effect. The smooth  $M_I^{TRGB} - (V - I)^{TRGB}$  relation displays a maximum around  $(V - I)^{TRGB} \sim 1.6$ , with the TRGB magnitude increasing steadily for redder colors.

Figure 23b shows TRGB magnitudes and colors for ages above 4 Gyr with  $[M/H] > -0.65$  and  $[M/H] < -0.65$  using the same symbols as Figure 23a compared with a ‘classical’ calibration (orange). This ‘classical’ calibration provides a median  $M_I^{TRGB} = -4.05$ , with typical observational uncertainties of  $\pm 0.10$  mag over the



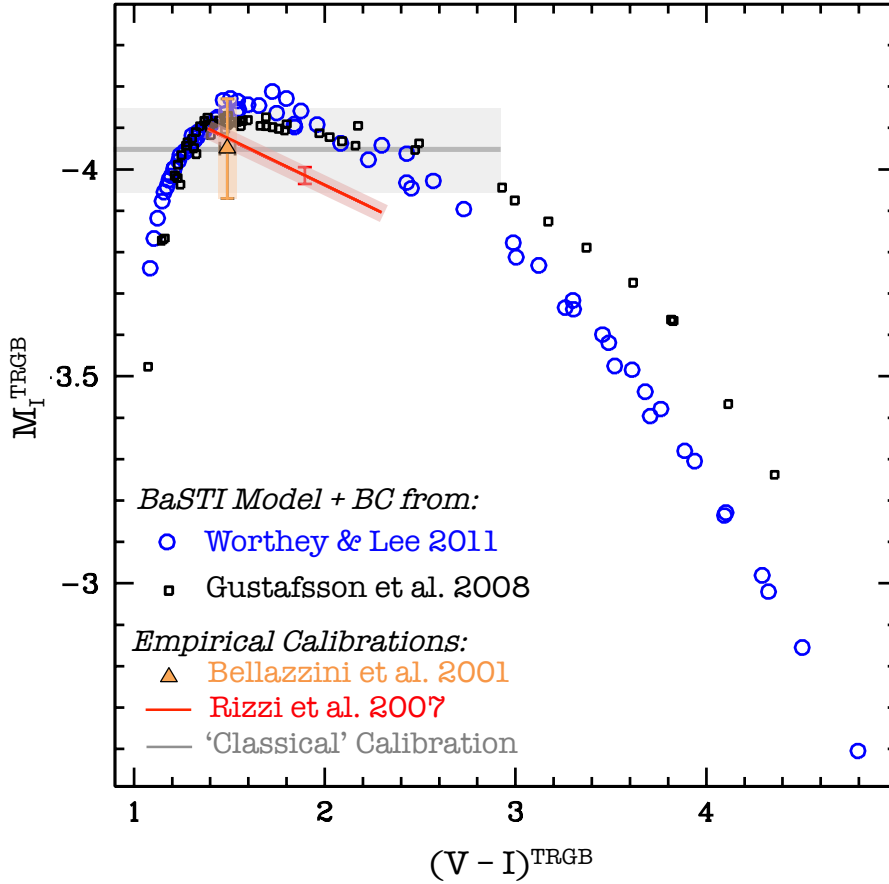


**Fig. 24** Theoretical  $M_I^{TRGB} - (V - I)^{TRGB}$  distribution at the TRGB for the full age range of the BaSTI models, but limited to sub-solar  $[M/H]$ . Two different sets of bolometric corrections are employed, more specifically those of Worthey and Lee (2011, blue circles) blue circles and of Gustafsson et al (2008, black squares). We also show the empirical estimate (Bellazzini et al, 2001) for  $\omega$  Centauri (orange triangle; Bellazzini et al, 2001) and the empirical relationship by Rizzi et al (2007) based on a sample of galaxies (red line). The range of the 'classical' calibration is shown in gray. The the zero point uncertainties are shown by the shading. See also Serenelli et al (2017).

range of  $V - I$  from 1.0 to 2.5 mag (shown with the shading; Lee et al, 1993; Salaris and Cassisi, 1997; Tammann and Reindl, 2013). The theoretical behavior of  $M_I^{TRGB}$  vs  $(V - I)^{TRGB}$  in this age and metallicity range is approximately quadratic, but using a constant average value of  $M_I^{TRGB}$  is a decent approximation as is shown by the shading in Figure 23b.

It is evident that the  $M_I^{TRGB} - (V - I)^{TRGB}$  relationship is very smooth for all  $[M/H]$ , and irrespective of any age sub-selection, and can be used as distance indicator for any stellar population with an RGB. Figure 24 compares the theoretical relationship of Figure 23 (open circles) to one obtained using the same models, but applying the bolometric corrections by Gustafsson et al (2008, open squares).

For these bolometric corrections we include the TRGB only up to  $[M/H] \sim$  solar, because at super-solar metallicities TRGB models have negative  $\log(g)$  (surface gravity) that are not covered by these bolometric corrections (additional discussion is given in Serenelli et al, 2017). We compare the theoretical relations to the empirical relationship determined by Rizzi et al (2007) on a sample of galaxies (solid red line) and the determination of the TRGB absolute magnitude for  $\omega$  Centauri, which has a broad range of metallicities and ages (Bellazzini et al, 2001) and the ‘classical’ calibration from Figure 23.

Rizzi et al (2007) calibration has roughly the same slope of the theoretical ones for  $(V - I)$  above  $\sim 1.6$ - $1.7$ , but with a magnitude offset of  $\sim 0.1$  mag. The uncertainty for the  $\omega$  Centauri datapoint is large and does not put very strong constraints on the TRGB absolute magnitude. The two sets of bolometric corrections applied to the theoretical calculations provide similar results as long as  $(V - I)$  is below  $\sim 2.0$ . Increasingly larger discrepancies appear for redder colors.

The panels of Figure 25 shows theoretical TRGB absolute magnitude-color calibrations for the infrared filters  $K_s$  and  $J$  (Figure 25a and 25b, respectively). Notice an almost linear behavior and again a smooth and tight correlation over the whole age and metallicity range covered by the models, with the added bonus of a lower sensitivity to reddening. Notice also how the dynamical range of the TRGB magnitude in  $J$  is reduced compared to the case of the  $K_s$  and  $I$  bands.

The panels of Figure 25 also compare the results from the different bolometric corrections, as in Figure 24. The uncertainty on the bolometric corrections is at the moment the major drawback for theoretical calibrations in these filters. Notice the different overall slope of the two sets of results, that cause systematic differences of the TRGB absolute magnitudes at fixed color up to  $\sim 0.2$  mag.

Wu et al (2014) have also derived empirically relationships in the corresponding infrared filters of the WFC3-*HST* system, namely  $F110W$  and  $F160W$  following the same methods as Rizzi et al (2007). Figure 26 compares their  $M_{F110W} - (F110W - F160W)$  TRGB relationship (red boxes) with the theoretical one based on Gustafsson et al (2008) bolometric corrections (filled circles). The overall shapes are different in the sense that the empirical calibration has a clear change of slope at  $(F110W - F160W) \sim 0.95$  that is not seen in the theoretical counterpart. Overall differences of the TRGB absolute magnitude at fixed color are however typically within  $\sim \pm 0.05$  mag.

## 4.2 Detecting the TRGB

In this subsection, we discuss the different techniques employed to determine the apparent magnitude of the TRGB, which is a sharp discontinuity along the observed luminosity function (LF). In the following, we discuss the major components of the TRGB detection process: edge-detection algorithms in Section 4.2.1, strategies used to account for the TRGB shape in Section 4.2.2, and brief caution regarding the overlap between the TRGB and other stellar sequences in Section 4.2.3.

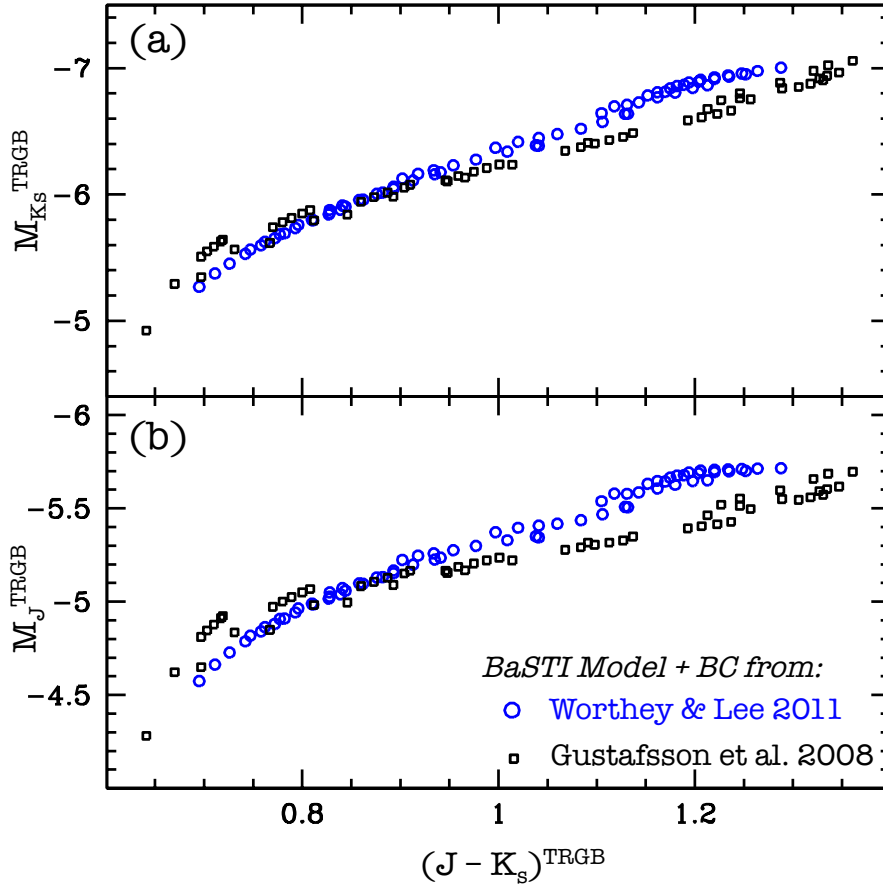


**Fig. 25** Theoretical  $M_{NIR}^{TRGB} - (J - K_s)^{TRGB}$  distribution at the TRGB for the full age and  $[M/H]$  range of the models, more specifically the panels are: (a)  $M_{K_s}^{TRGB} - (J - K_s)^{TRGB}$  and (b)  $M_J^{TRGB} - (J - K_s)^{TRGB}$ . The color coding matches that of Figure 24, more specifically open circles denote results obtained with the Worthey and Lee (2011) bolometric corrections, whilst open squares display results obtained with the Gustafsson et al (2008) bolometric corrections. Overall, the NIR-TRGB magnitude shows an approximately linear relationship with  $J - K_s$  color and, compared to the optical (Figures 23 and 24), it more than 1 magnitude brighter, spans a range of  $\sim 1$  mag over this range of  $[M/H]$  and ages, but spans a much more narrow color-range. See also Serenelli et al (2017).

**Table 2** Discrete Approximations to the First Derivative Used for TRGB Detection

Reference	Derivative Approximation
Lee et al (1993)	$[-2, 0, +2]$
Madore and Freedman (1995)	$[-1, -2, 0, +2, +1]$
Sakai et al (1996)	$\Phi(I + \sigma_m) - \Phi(I - \sigma_m)$
Méndez et al (2002)	$\sqrt{\Phi}[\log(\Phi(I + \sigma_m)) - \log(\Phi(I - \sigma_m))]$
Mager et al (2008)	$\sqrt{\sum N_m}[\log(\Sigma N_m) - \log(\Sigma N_m)]$
Madore et al (2009)	$[-1, -1, -1, 0, 0, +1, +1, +1]$
Jang and Lee (2017a)	$[-1, -2, -1, 0, +1, +2, +1]$
Hatt et al (2017)	$[-1, 0, +1]$

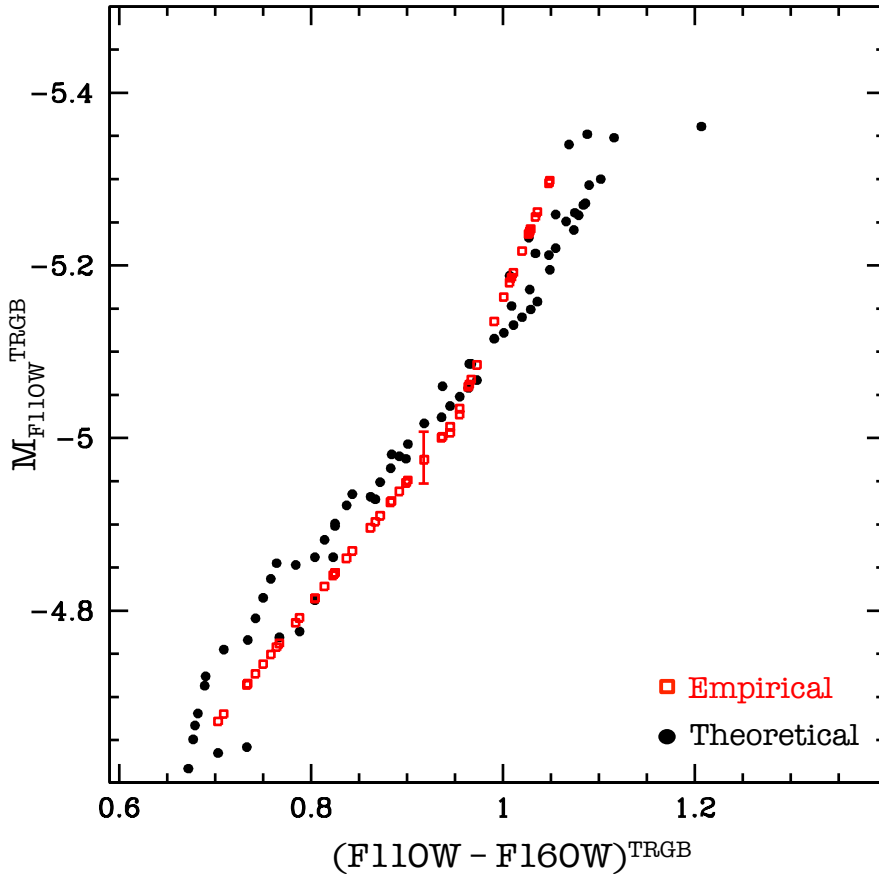


**Fig. 26** Comparison of theoretical and empirical calibrations of the NIR-TRGB color-magnitude distribution for the *HST*+WFC3/IR filters F110W and F160W, which are similar to the 2MASS *J* and *H*. The filled black circles are the theoretical predictions from BaSTI using the Gustafsson et al (2008) bolometric corrections and the open squares are the empirical measurements from Wu et al (2014). The error bar on the zero point of the empirical calibration is also displayed.

#### 4.2.1 Edge-Detection Techniques

Practically, the LF is constructed from binning the magnitudes of RGB stars from selection over an appropriate color range. The TRGB is detected by finding the point of greatest change in the LF, either using tools that approximate the first derivative or tools that model the components of the LF itself (e.g., individual stellar sequences). Poisson noise occurs in the LF, especially in smaller samples (like in GGCs), which in turn create spurious spikes in the edge-detection response. Thus, smoothing is generally used to mitigate this noise, which can either be (i) incorporated into the functional form of the edge-detection kernel, (ii) applied to

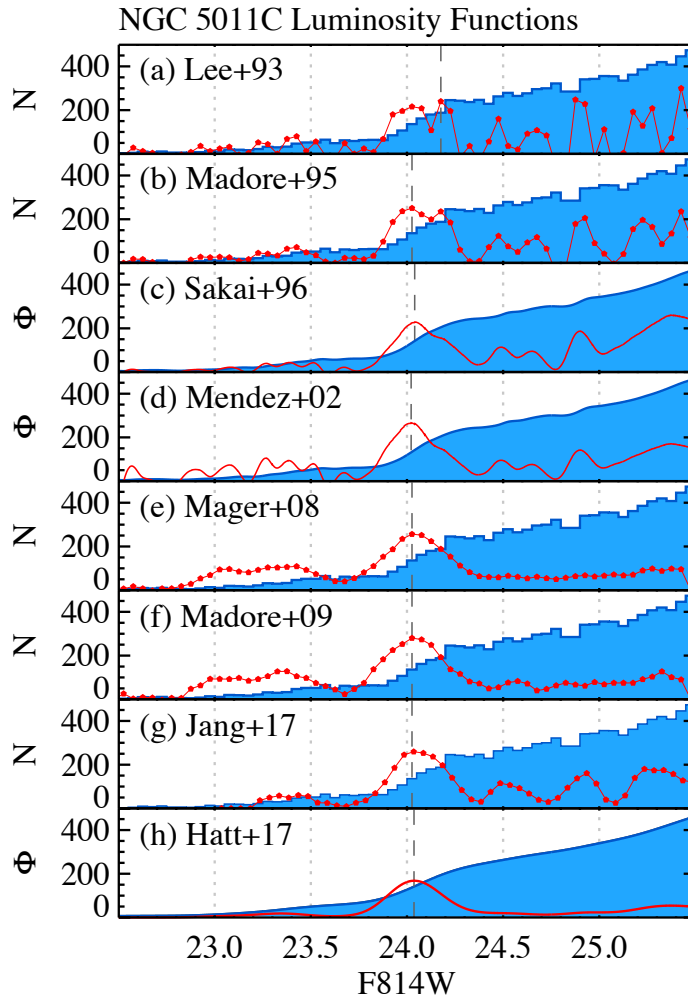


**Fig. 27** Following Jang et al (2018, their figure 9), F814W luminosity functions (blue histograms) and edge-detection responses (red lines) applied to NGC 5011 C. Each panel applies a specific TRGB algorithm to the same underlying data, as follows: (a) Lee et al (1993), (b) Madore and Freedman (1995), (c) Sakai et al (1996), (d) Méndez et al (2002), (e) Mager et al (2008), (f) Madore et al (2009), (g) Jang and Lee (2017a), and (h) Hatt et al (2017). The histograms show modifications for smoothing as employed in each of the studies with y-axis labels of  $N$  for binned starcounts and  $\phi$  for smoothing. The TRGB is detected in each plot as the maximum of the response function, which is indicated by the dashed vertical line. Generally the algorithms agree for this dataset, but differences can occur as in Jang et al (2018).

the LF itself, or (iii) folded into the model. Edge detection techniques for the TRGB come in the following forms:

1. discrete approximations to the derivative (e.g., the Sobel kernel),
2. discrete approximations to the derivative that incorporate smoothing (e.g., a Gaussian formulation of the Sobel kernel),

3. maximum-likelihood fitting techniques (e.g., fitting a functional form to the LF with the TRGB as a parameter).

These methods can applied LF that are either discrete (e.g., with large bins) or a “continuous” (e.g., with bins over very small intervals). Each method has advantages and disadvantages that should be weighed for the science application in question. As an example, simulations by Madore and Freedman (1995) demonstrated that at least 100 stars within one magnitude below the TRGB to detect unambiguously the TRGB for their algorithm and similar tests should be performed for any algorithmic approach to provide guidance for its application. Popular forms of the discrete derivative approximations are given in Table 2. Alternative parametric and non-parametric methods have been also applied to determine the TRGB magnitude in a number of stellar systems; the studies of Cioni et al (2000); Conn et al (2011); Makarov et al (2006) are representative examples.<sup>9</sup>

Figure 27 compares applications of eight different forms for TRGB detection from the literature similar to the comparison in NGC 1365 made by Jang et al (2018, their figure 9). The same photometry for NGC 5011 C, a dwarf galaxy in the Centaurus A group (Tully, 2011), has been used in each panel. The histograms are slightly different owing to the prescriptions of the individual method; those that use direct binned LFs have  $N$  labels and those that smooth and/or resample the LF have are labeled  $\phi$ . Comparison of the LF histograms, show that they look relatively similar irregardless of the smoothing, thus differences in the edge-response (red) can be largely attributed to the formulation of edge-detection algorithm.

The edge-detection response function is shown in red in each panel of Figure 27. The form of the algorithm is given in Table 2. The Lee et al (1993), Madore and Freedman (1995), Jang and Lee (2017a), and Madore et al (2009) kernels are similar and are applied to binned LFs, except that additional elements are progressively added into the kernel that act to “smooth” the response; this is seen by comparing Figures 27a, 27b, 27g, and 27f that show a progressive smoothing of the edge-detection response. The algorithms for Sakai et al (1996), Méndez et al (2002), and Mager et al (2008) implement smoothing directly into the algorithm using various means of suppressing the noise; in particular, Sakai et al (1996) uses adaptive binning and both Méndez et al (2002) and Mager et al (2008) use a poison-noise weight applied to a logarithmic form. The impact of these forms can be seen as Figure 27c largely shows the same features as the previous discrete forms, but slightly broader and smoother and both Figure 27d and 27e show a slight amplification of the smaller scale features due both their weighting and logarithmic forms. Figure 27h that was proposed in Hatt et al (2017) and used subsequently by Jang et al (2018) and Hatt et al (2018) uses a Guassian smoothing function on the LF but applies the simple Sobel kernel from Lee et al (1993), which results in an unambiguous single peaked edge-response.

The magnitude bin of maximum response for each panel are not significantly different from each other (especially considering the discrete forms use magnitude bins of 0.05 mag):  $m_{F814W}^{TRGB} = 24.18, 24.03, 24.04, 24.02, 24.03, 24.03, 24.03,$  and  $24.04$  mag for panels (a) to (h), respectively. The total range of th detection is 0.16 mag or 8% in distance. The edge-response peak is asymmetric in many of the panels, but only in Lee et al (1993) (Figure 27a) is the maximum response in the secondary peak; excluding this result, the range is 0.02 mag or 1% variation

<sup>9</sup> Additional non-parametric studies are listed in Jang et al (2018).

**Table 3** Calibrations of the Shape of the OPT-TRGB

Reference	Calibration of $M_I$	$\sigma_{ZP}$
Color Based Calibrations:		
Lee et al (1993)	-4.0	$\pm 0.1$
Rizzi et al (2007)	$-4.05 + 0.217[(V - I)_0 - 1.6]$	none given
Bellazzini (2008)	$-3.939 - 0.194(V - I)_0 + 0.080(V - I)_0^2$	none given
Madore et al (2009)	$-4.05 + 0.2[(V - I)_0 - 1.5]$	none given
Jang and Lee (2017a)	$-4.015 - 0.007[(V - I)_0 - 1.5] + 0.091[(V - I)_0 - 1.5]^2$	$\pm 0.058$
Metallicity Based Calibrations:		
Salaris and Cassisi (1997)	$-3.732 + 0.588[\text{M}/\text{H}] + 0.193[\text{M}/\text{H}]^2$	Theoretical
Bellazzini et al (2001)	$-3.66 + 0.48[\text{Fe}/\text{H}] + 0.14[\text{Fe}/\text{H}]^2$	$\pm 0.12$
Bellazzini et al (2004)	$-3.629 + 0.679[\text{M}/\text{H}] + 0.258[\text{M}/\text{H}]^2$	$\pm 0.12$

in distance. This is a more consistent result than for NGC 1365, which was the example shown in Jang et al (2018). This LF showed a much larger degree of variation in the peak response for these same algorithms, albeit the authors ultimately concluded the results were not dissimilar within the statistical uncertainties. Thus, it is important to choose the algorithm carefully for a given application.

The uncertainties on the TRGB detection are particularly difficult to determine and there is a similar degree of variation in how this measurement is made as in the TRGB detection algorithm. The strategies incorporate one or more of the following elements: boot-strap or jack-knife resampling of the LF, the bin-size, the mean photometric uncertainty at the tip, the width of the response function, the width of the kernel, and the signal-to-noise of the detection. Certainly each of these elements play a role in the underlying uncertainty, but each contributes differently in terms of random or systematic elements. One particular uncertainty that is often overlooked is the start point of the binning itself; even with bins of 0.05 mag, the TRGB result will change as the bins are shifted small amounts.

To counter this, Hatt et al (2017) presents a detailed discussion of how the uncertainties, from the magnitudes and colors to the binning, are coupled in complex ways. As a result of this investigation, Hatt et al (2017) developed end-to-end simulations that insert an artificial TRGB into their images, photometer it, and measure the TRGB in statistical fashion. This technique combines many of the strategies listed, but adds an ability to measure both random and systematic uncertainty as the TRGB inserted into the images was known a priori. Using these simulations, they not only produce rigorous estimates of their uncertainties, but use the statistical distributions to select the best smoothing parameters for their LF. The Hatt et al methodology naturally incorporates the effects of incompleteness and crowding. This method has been applied thus far to five galaxies out to 20 Mpc distant with good results (Hatt et al, 2017; Jang et al, 2018; Hatt et al, 2018).

#### 4.2.2 Techniques to “Sharpen” the Tip Edge

The absolute magnitude of the TRGB is often approximated to a single value:  $M_I^{TRGB} \sim -4.05 \pm 0.10$  mag (see, e.g., Lee et al, 1993; Salaris and Cassisi, 1997; Tammann and Reindl, 2013; Bellazzini et al, 2001, and references therein). However, as shown in Figures 23 and Figures 24, outside of the old, metal-poor regime,  $M_I^{TRGB}$  is not, in fact, constant. Fortunately, the age or metallicity effect is pro-

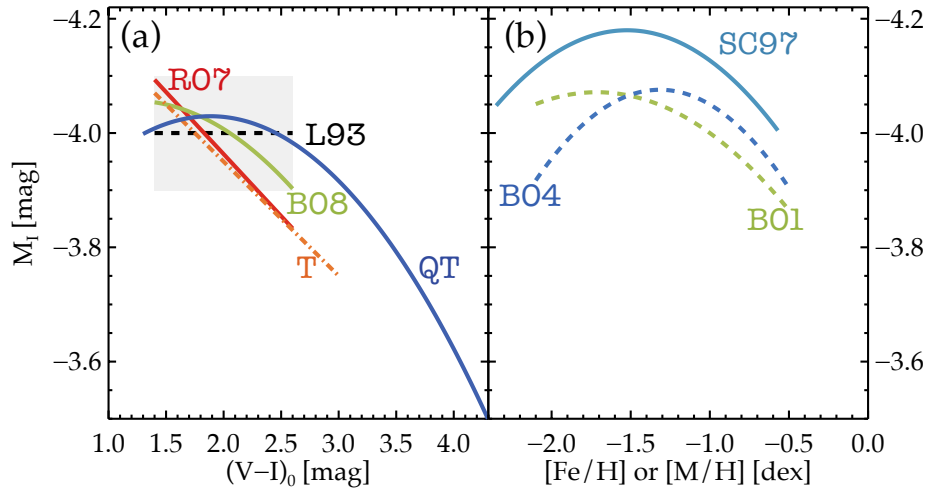


**Fig. 28** Comparison of optical TRGB calibrations. (a) Calibrations of  $M_I$  in terms of  $(V-I)_0$ . The uncertainties on the zero points are  $\sim \pm 0.10$  mag the span of which is shown by the gray shading, with the exception of the QT calibration at  $\pm 0.06$  mag using multiple calibration paths (for details see Jang and Lee, 2017b). (b) Calibrations of  $M_I$  in terms of  $[\text{Fe}/\text{H}]$  or  $[\text{M}/\text{H}]$ , the uncertainty on the zeropoint of B04 and B01 is  $\pm 0.12$  mag and for SC97, which is from theoretical models, see Section 4.1. The labels are as follows, in panel a: L93 – Lee et al (1993); R07 – Rizzi et al (2007), B08 – Bellazzini (2008), T: Madore et al (2009), and QT: Jang and Lee (2017b); and in panel b: SC97 – Salaris and Cassisi (1997); B01 – Bellazzini et al (2001), and B04 Bellazzini et al (2004).

jected into the color of the star, e.g., more metal rich and/or younger stars are fainter and redder in  $I, (V-I)$  CMDs than old their metal-poor counterparts. To both boost the signal at the TRGB and to avoid spurious detections, many authors take this effect into consideration.

The two primary ways to counteract the shape of the TRGB are as follows:

1. *Magnitude-Color Calibration*: Instead of determining a single-valued calibration, the calibration can be measured as a function of the mean  $V-I$  color known as the  $M_I^{TRGB} - (V-I)^{TRGB}$  relation. Here, the TRGB  $(V-I)$  color basically accounts for the star formation history of the observed population. Typically, users of this technique will use the mean color of the RGB sequence to estimate  $M_I^{TRGB}$  for their system. An alternate formulation relates  $M_I^{TRGB}$  directly to the metallicity. Given that the metallicity has to be measured independently, preferably from spectroscopy, but often in reference to theoretical stellar tracks (isochrone fitting), this is not necessarily an advantage.
2. *T magnitude*: Madore et al (2009) suggested that, instead of fitting a more complex zero-point, to calibrate the slope out of the color-magnitude data. Madore et al used theoretical tracks to produce an alternate magnitude system, known as the “T” for TRGB-magnitude system. This technique transforms the observed photometry into a system where the TRGB is flat – effectively torquing the CMD (a useful schematic can be found in figure 1 of Madore et al, 2009). Then, a single calibration to the metal-poor portion of the TRGB can be applied to the data over the full range. This can be done independent of



priors on metallicity. The Madore et al (2009) formulation is as follows:

$$T = I - \beta[(V - I)_0 - \gamma], \quad (25)$$

where  $\gamma$  is a fiducial color (preferably where the absolute zero point is determined) and  $\beta$  was determined relative to theoretical models to be  $\beta = 0.20$  from Bellazzini et al (2001), but values ranging from 0.15 (Mager et al, 2008) to 0.22 (Rizzi et al, 2007) have been used.

3. *QT magnitude*: More recently, Jang and Lee (2017b) expanded upon this initial formulation proposing the *QT* magnitude system, where the *Q* stands for “quadratic” because the functional form is a quadratic in color. The *QT* magnitude takes on the following form:

$$QT = F814W - \alpha(\text{color} - \gamma)^2 - \beta(\text{color} - \gamma) \quad (26)$$

where  $\alpha = 0.159 \pm 0.010$ ,  $\beta = -0.047 \pm 0.020$ , and  $\gamma = 1.1$  for the *F814W*, *F606W* – *F814W* magnitude-color combination (similar to the ground based *I*, *V* – *I*). Jang and Lee (2017b) provide calibrations in several common *HST* filter combinations.

Table 3 summaries several of the color-magnitude and metallicity-magnitude calibrations of the optical TRGB and their uncertainties, if available. The calibrations are compared in Figure 28, where Figure 28a shows the  $M_I$ -(*V* – *I*) calibrations and Figure 28b shows the  $M_I$ -[*Fe*/*H*] calibrations. The common single-value from Lee et al (1993) and its approximate color-range is also shown for comparison and its uncertainty largely encompasses the  $M_I$  span of the more complex forms for the blue-side of the RGB. Moreover, Hatt et al (2017) and Jang et al (2018) both demonstrated that there was no formal difference between the TRGB detections for in native, T or QT magnitudes for metal-poor systems. As with the edge-detectors, the application of these different techniques depends largely on the situation; in particular, only when there are well measured colors, there are significant red populations, and the uncertainties due to the transform be estimated, is it advisable to adopt more complex forms of the absolute calibration.

#### 4.2.3 Contamination to the LF

Unfortunately, over its color-magnitude span, the RGB is not the only stellar sequence. A particularly vexing containment are the asymptotic giant branch stars (AGB), that cover a magnitude range overlapping with the brightest portion of the RGB, and eventually, depending on the galaxy star formation history, can extend to much brighter magnitudes than the TRGB (for more description of the AGB see Håbing and Olofsson, 2003; Rosenfield et al, 2014, 2016, and references therein). The AGB are particularly daunting because the RGB is their progenitor population and so, where there are strong RGB sequences, there is likely an AGB sequence, albeit at lower overall numbers.

The start of the AGB sequence for stars more luminous than the RGB can be confused for the TRGB. This can be seen in Figure 27, especially for the Méndez et al (2002) and Mager et al (2008) algorithms, there are small increases in the LF and edge-response at  $\sim 1$  magnitude brighter than the TRGB. While in the NGC 5011 C case the effect is small, it is not so in galaxies with more recent star

formation. An example being attempts to detect the TRGB in the Antennae galaxy (NGC 4038/39) by Saviane et al (2004, 2008), who found  $\mu = 30.7 \pm 0.25$  (random)  $\pm 0.14$  (systematic) mag. A later study, Schweizer et al (2008), took into account the AGB population and used fields outside of the main star forming disk to find  $\mu = 31.51 \pm 0.12$  (random)  $\pm 0.12$  (systematic) mag, which has been independently confirmed by Jang and Lee (2015). The Saviane et al physical distance was 13.3 Mpc compared to Schweizer et al measuring 20 Mpc, which demonstrates the impact neglecting AGB stars can have.

Mitigation strategies for the AGB include: fitting the full form of the LF, including an AGB component, as in Méndez et al (2002, among others) or working in regions of galaxies where the likelihood of significant contamination is small like in stellar halos (see discussion in Beaton et al, 2016). It is worth mentioning, that in regions that are dominated by younger stellar populations (like in disks), other populations like red super giants or highly extinguished yellow super giants (Cepheids), can also cause difficulty measuring the TRGB confidently (see, e.g., in the LMC and SMC in Figure 1). These latter populations show much more intrinsic variations as well as being embedded in dust (e.g. local changes in extinction) such that they are much more difficult to model. For the highest precision and accuracy, the TRGB is best applied to old population regimes.

#### 4.3 Case Study for the Optical TRGB

Here we present an example of the TRGB distance measurement for the Local Group dwarf elliptical galaxy, NGC 185 (E3 pec) using the dataset described in Geha et al (2015, Proposal ID:GO11724). Figure 29a shows the  $F814W - (F606W - F814W)$  CMD (similar to ground based  $I, V - I$ ) for a halo field in NGC 185 and it is evident that the bulk of the bright stars are Pop II. The CMD, itself, shows multiple stellar populations, including the main sequence, blue stragglers, HB, AGB, and RGB, but few unambiguously Pop I sequences (e.g., compare to the LMC and SMC in Figures 1a and 1b). The TRGB is the brightest part of RGB sequence and is marked by a dashed line.

The apparent magnitude of the TRGB is determined from the  $I$  ( $F814W$ ) luminosity function, which is given in Figure 29b. Because the TRGB is, effectively, the ending point of the RGB sequence, the LF should show a strong discontinuity at the TRGB. Here, we applied the edge-detection algorithm introduced in Mager et al (2008) and plotted the response in Figure 29b as a solid line. The edge-detection response shows a strong peak at  $F814W = 20.43$  mag. Using bootstrap resampling of the LF and subsequent TRGB detection, the uncertainty on the TRGB measurement is  $\pm 0.03$  mag or a 1.5% statistical uncertainty for the TRGB measurement.

The distance modulus is then determined using a calibration of the TRGB absolute magnitude in the  $F814W$  filters and we adopt the Rizzi et al (2007) calibration given in Table 3. In this formulation, the age-metallicity behavior of the TRGB is modeled using the color of the RGB star, effectively fitting a tilted line to the TRGB absolute magnitude (shown in Figure 24). The median TRGB color in Figure 29a is  $F606W - F814W = 1.43 \pm 0.02$  mag. Foreground extinction is estimated to be  $E(B-V) = 0.162$  mag, corresponding to  $A_{F814W} = 0.281$  and  $A_{F606W} = 0.455$  mag (Schlafly and Finkbeiner, 2011). Combining the absolute

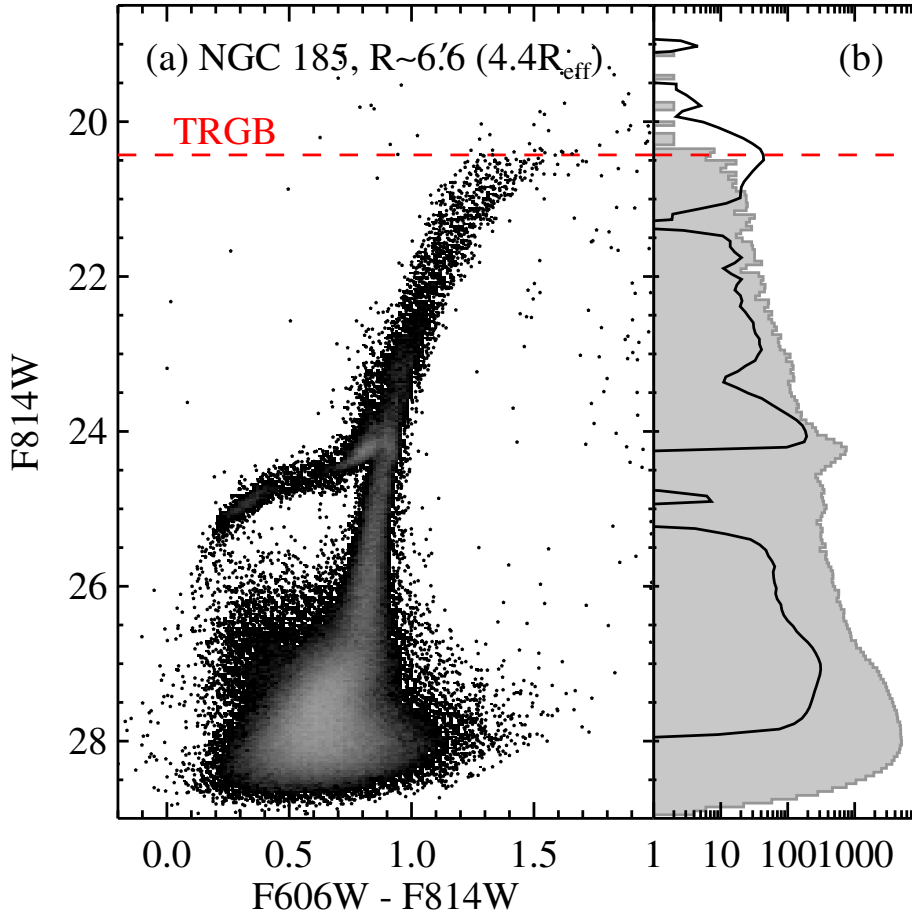


**Fig. 29** Demonstration of the TRGB measurement process for the Local Group galaxy NGC 185 using *HST*+ACS data. (a)  $F814W - (F606W - F814W)$  CMD of resolved stars in its outer region ( $R > 4.4R_{\text{eff}}$ ). The TRGB is marked by a dashed line. (b)  $F814W$ -band luminosity function of resolved stars (histogram) and corresponding edge-detection response (solid line). A strong edge-detection response is seen at the TRGB ( $F814W_{\text{TRGB}} = 20.43 \pm 0.03$  mag).

magnitude of the TRGB ( $M_{F814W} = -4.06 \pm 0.12$ ) with the apparent magnitude of the TRGB ( $F814W = 20.43 \pm 0.03$ ), we obtained a value for the distance modulus,  $(m - M)_0 = 24.21 \pm 0.03(\text{random}) \pm 0.12(\text{systematic})$  mag.

This value is in good agreement with those based on red clump stars,  $(m - M)_0 = 24.51 \sim 24.64$  mag (Pietrzyński et al, 2010), and RRLs,  $(m - M)_0 = 23.93 \sim 24.15$  mag (Salaris and Cassisi, 1997, 1998; Tammann et al, 2008). The distance summary for NGC 185 provided by de Grijs and Bono (2014) quotes the mean distance of  $24.027 \pm 0.333$  mag from 26 studies for the TRGB,  $23.993 \pm 0.128$  mag for the RR Lyrae from 8 studies, and  $23.997 \pm 0.119$  mag for the full sample of distances.

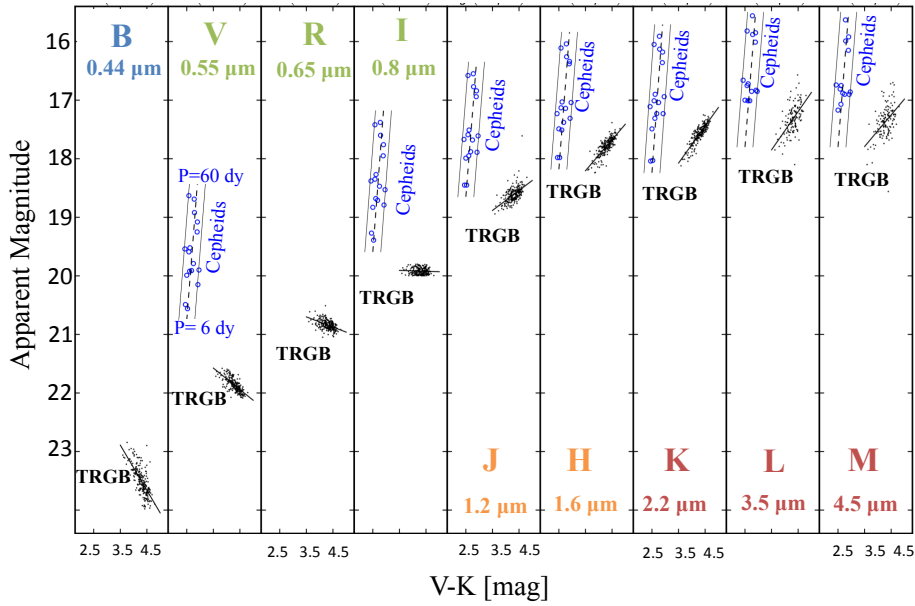


**Fig. 30** The TRGB morphology as a function of wavelength for the Local Group dwarf galaxy NGC 6822. From left to right, the magnitudes in the  $B$ ,  $V$ ,  $I$ ,  $J$ ,  $H$ ,  $K$ ,  $L$ , and  $M$  bands are plotted against the  $V - K$  color. TRGB stars are selected in the  $I$ , where the slope is flat, and the same stars are plotted in the other panels. For comparison, the Cepheid sequence in NGC 6822 is plotted when the Cepheids could be identified in the data. Figure courtesy of Erika Carlson and using data from Rich et al (2014).

#### 4.4 Developments for the IR-TRGB as a Distance Indicator

Figure 30 compare the TRGB (black points) to the CC sequence (blue circles) in the Local Group dwarf NGC 6822. Each panel uses a different photometric band plotted against the  $V - K$  color, more specifically, (from left to right)  $B$ ,  $V$ ,  $I$ ,  $J$ ,  $H$ ,  $K$ ,  $L$ , and  $M$ . The TRGB stars are identified in the  $I$  where the tip is relatively flat and the same stars are plotted in each of the panels. The physical behavior of the TRGB described previously is seen empirically as the sloping tips in bands bluer and redder than  $I$ . While in the optical bands the CC population is significantly brighter than the TRGB, in the IR the TRGB is comparable to the shortest period stars (here  $P=10$  days). Considering that TRGB is non-variable, there are significant gains in observational efficiency using the TRGB in the IR for distances. We will focus on the NIR, but note that discussions of MIR stellar populations can be found in Boyer et al (2015b,a).

Of course, owing to the steep slope of the TRGB in the IR, the tools developed in the optical case study are not immediately applicable. Dalcanton et al (2012), Wu et al (2014), and Górski et al (2016) address this issue by using TRGB detection at a fiducial mean color for the RGB sequence (this is not dissimilar from means of calibrating the redder optical populations). Using their large sample of nearby dwarf galaxies Dalcanton et al (2012) note, however, that there is a range of mean color across their sample and they correlate this range with the mean metallicity of the galaxies (inferred from star formation histories of the same

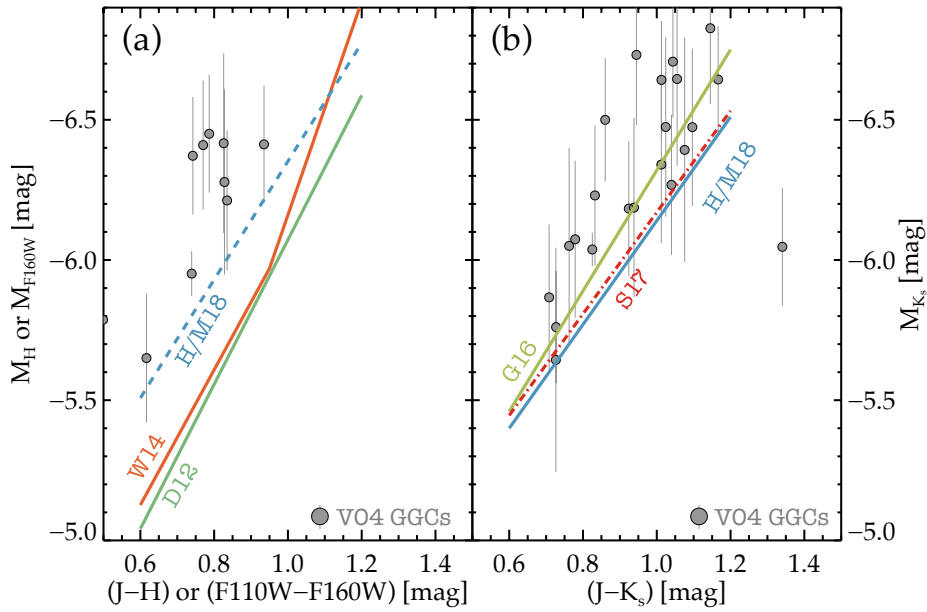


**Fig. 31** Comparison of IR-TRGB slope measurements. (a)  $M_H$  against  $J - H$  for GGCs in Valenti et al (2004, grey circles) and the LMC zeropoint + IC 1613 slopes from Hoyt et al (2018) and Madore et al (2018) (dashed blue line), respectively.  $M_{F110W}$  is plotted against  $F110W - F160W$  on the same panel (without transformation) and compares Wu et al (2014, orange) and Dalcanton et al (2012, green). (b)  $M_{K_s}$  against  $J - K_s$  for GGCs in Valenti et al (2004, grey circles), theoretical calibration from Serenelli et al (2017, dot-dash red), and LMC zeropoint + IC 1613 slopes from Hoyt et al (2018) and Madore et al (2018) (solid blue line). There is a clear distinction between the ground 2MASS and space WFC3/IR filter sets, but generally calibrations agree reasonably well. Functional forms are given in Table 4.

field). Stated differently, it is not sufficient to calibrate the TRGB in the IR at one color, the slope of the TRGB needs to be determined.

Several calibrations of the sloped IR-TRGB are given in Table 4. The calibrations from both Dalcanton et al (2012) and Wu et al (2014) are in the *HST* flight system and are tied to optical TRGB measurements. Wu et al (2014) rely heavily on theoretical stellar tracks to guide their calibration. Górski et al (2016), on the other hand, transform a calibration from GGCs by Valenti et al (2004) in 2MASS bandpasses to the color-magnitude plane. Recently, Madore et al (2018) and Hatt et al (2018) combine a magnitude-color slope measurement from IC 1613 with a zero-point determined in the LMC, both in 2MASS bandpasses.

These calibrations are compared in the panels of Figure 31, with Figure 31a showing  $M_H$  ( $M_{F160W}$ ) versus  $J - H$  ( $F110W - F160W$ ) and Figure 31b showing  $M_{K_s}$  versus  $J - K_s$ . The calibrations previously described are all shown, with the individual GGC data from Valenti et al (2004) in both panels and a recent theoretical calibration from Serenelli et al (2017) in Figure 31b.

First, there is a noticeable offset between the 2MASS and *HST* filter systems shown in Figure 31a that is likely due to bandpass differences that are described in Riess (2011) and discussed by Dalcanton et al (2012). Both Dalcanton et al (2012) and Riess (2011) use stellar models to transform between 2MASS and *HST*

**Table 4** Calibrations of the Shape of the IR-TRGB

Reference	$\lambda$	Calibration of $M_\lambda$	Notes
Color Based Calibrations, <i>HST</i> Flight System:			
Dalcanton et al (2012)	F160W	-3.496 -2.576 (F110W-F160W)	rms=0.05
Wu et al (2014)	F160W	-5.97 -2.41[(F110W-F160W) - 0.95]	blue
		-5.97 -3.81[(F110W-F160W) - 0.95]	red
	F110W	-5.02 -1.41[(F110W-F160W) - 0.95]	blue
Serenelli et al (2017)		-5.02 -2.81[(F110W-F160W) - 0.95]	red
	F110W	-4.630 -9.525[(F110W-F160W) - 0.68]	blue, Theoretical
		-4.630 -1.511[(F110W-F160W) - 0.68]	red, Theoretical
	F160W	-5.310 -10.525[(F110W-F160W)- 0.68]	blue, Theoretical
		-5.310 - 2.511[(F110W-F160W)-0.68]	red, Theoretical
Color Based Calibrations, 2MASS System:			
Górski et al (2016)	K	-6.32 - 2.15 [(J-K <sub>s</sub> ) - 1.00]	ZW84 scale
	J	-5.32 - 1.15 [(J-K <sub>s</sub> ) - 1.00]	ZW84 scale
Serenelli et al (2017)	K	-6.17 - 1.81[(J-K <sub>s</sub> ) - 1.00]	theoretical
	J	-4.96 - 0.81[(J-K <sub>s</sub> ) - 0.76]	theoretical
Madore et al (2018) and Hoyt et al (2018)	J	-5.13( $\pm 0.01_{stat} \pm 0.06_{sys}$ ) - 1.11( $\pm 0.15$ ) [(J-H)-0.80]	
	H	-5.93( $\pm 0.01_{stat} \pm 0.06_{sys}$ ) - 2.11( $\pm 0.26$ ) [(J-H)-0.80]	
	K	-6.13( $\pm 0.01_{stat} \pm 0.06_{sys}$ ) - 2.41( $\pm 0.36$ ) [(J-H)-0.80]	
	J	-5.14( $\pm 0.01_{stat} \pm 0.06_{sys}$ ) - 0.85( $\pm 0.12$ ) [(J-K)-1.00]	
	H	-5.94( $\pm 0.01_{stat} \pm 0.06_{sys}$ ) - 1.62( $\pm 0.22$ ) [(J-K)-1.00]	
	K	-6.14( $\pm 0.01_{stat} \pm 0.06_{sys}$ ) - 1.85( $\pm 0.27$ ) [(J-K)-1.00]	
Metallicity Based Calibrations:			
Valenti et al (2004)	J	-5.67 - 0.31[Fe/H]	GGCs, CG97 scale
	H	-6.71 - 0.47[Fe/H]	GGCs, CG97 scale
	K	-6.98 - 0.58[Fe/H]	GGCs, CG97 scale
	$M_{bol}$	-3.87 - 0.18[Fe/H]	GGCs, CG97 scale
	J	-5.64 - 0.32[M/H]	GGCs
	H	-6.66 - 0.49[M/H]	GGCs
	K	-6.92 - 0.62[M/H]	GGCs
	$M_{bol}$	-3.85 - 0.19[Fe/H]	GGCs

flight systems, but inconsistencies still remain for these red stars whose models are more uncertain (see Dalcanton et al, 2012, their figure 18 and associated discussion). Second, comparing similar filter systems, the results are not terribly dissimilar; Wu et al (W14, 2014) and (D12, Dalcanton et al, 2012) largely agree, with the former have more objects at redder colors (they also employ very similar overall strategies). Hoyt et al (2018) and Madore et al (2018) (collectively called H/M18 in the figure) find results not dissimilar from the GGCS from Valenti et al (2004), especially considering the TRGB in GGCS is not always well populated and AGB/RGB stars cannot be disentangled. Górski et al (2016) agrees well with Valenti et al (2004), as anticipated, as their relations are derived from those data.

Unfortunately, both Dalcanton et al (2012) and Wu et al (2014) predominantly use relatively distant objects for the calibration, for which precise distances are not necessarily known independent of TRGB analyses. Górski et al (2016), Madore et al (2018), Hoyt et al (2018), and Valenti et al (2004), on the other hand, focus on the Local Group dwarfs for which independent high-precision distances are known and they find reasonable agreement between these works and their own distances. Of course the divide between filter systems still persists in these comparisons, as does the technique of application.

Dalcanton et al (2012), Wu et al (2014), and Górski et al (2016) each measure the TRGB absolute magnitude at the mean-color of the RGB (similar to the

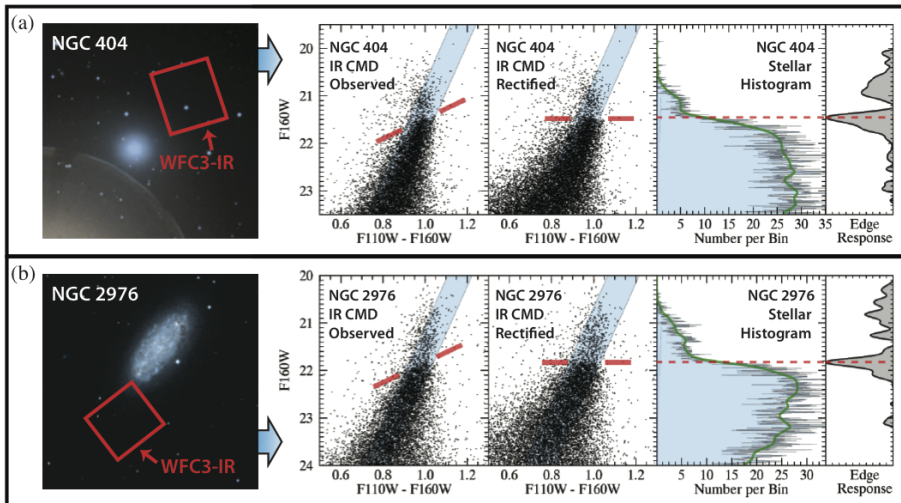


**Fig. 32** Use of the NIR-TRGB as a distance indicator applied to (a) NGC 404 and (b) NGC 2976. The photometry is from Dalcanton et al (2012). The WFC3-IR field used is shown in red for GALEX images of the galaxies in the left most panels. The CMD is shown in the left central panels and a ‘rectified’ CMD is shown in the next panel, from which a luminosity function is determined and an edge-detector employed. Figure courtesy of Mark Seibert and photometry courtesy of Julianne Dalcanton and Ben Williams.

procedure followed for NGC 185 in Section 4.3), which is slightly different from the measurements of Hoyt et al (2018) and Madore et al (2018) that measure the slope in the color-magnitude diagram. As in the optical, an alternate technique is to use a “T” magnitude that accounts for the color dependence. Hoyt et al (2018) demonstrated this method to be extremely effective (precise and accurate), as they were able to see internal structure of the LMC by determining distances to individual zones across the LMC. The alternate technique is demonstrated in Figures 32a and 32b for two galaxies in the Dalcanton et al (2012) sample, NGC 404 and NGC 2976. Here, the sloped-TRGB is rectified into a “T” magnitude system, to which the same edge-detection tools from the optical are applied to determine the TRGB magnitude (here following the methods of Hatt et al, 2017).

#### 4.5 Summary

In this Section, we have described the TRGB as a standard candle from a theoretical and empirical perspective. The TRGB is the terminus of the RGB sequence that occurs at the transition from H-shell burning to He-core burning. In the  $I$ -band, the TRGB is observed to have a constant value of  $M_I = -4$  mag with uncertainties at the 0.1 mag level for old, metal-poor stars. Many empirical and theoretical investigations have provided refinements to this value that are largely consistent, but only via secondary calibration methods; no direct calibration exists.

The TRGB method relies on detecting the star of the RGB sequence, which has been implemented in a myriad of methods, some of which were compared directly in Figure 27. Generally, the choice of the most appropriate method depends on

the scientific application and the data at hand, e.g., what filters are available, the number of sources populating the TRGB, and the contamination, among other concerns. Despite the diversity of the approaches summarized here, the advantage of using a relatively-luminous non-variable stellar population comes with dramatically higher observational efficiency than that of variable stars.

## 5 Systematics and the Absolute Scale

The goal of this section is to compare the absolute scales amongst the old stellar population standard candles. An overall review of progress toward a self-consistent distance scale for all standard candles can be found in de Grijs et al (2017), with significant works focusing on overall consistency for objects within  $\sim 1$  Mpc given in de Grijs et al (2014); de Grijs and Bono (2014, 2015). A discussion of absolute scales, ultimately, rests onto two nuanced points: (i) full evaluation the systematics associated with the distance measurements, and (ii) a full understanding of the true independence of the scales utilized by each standard candles. To set the stage for this discussion, we open with a case study that compares distance measurements from CCs, RRL, and the TRGB in the Local Group galaxy IC 1613 in Section 5.1. In Section 5.2, the “primary” methods to set the absolute scale are described with summaries of progress for each of the standard candles. Section 5.3 discusses the “secondary” methods to set the absolute scale, these being the adoption of a distance to a specific object and using the standard candle in that object. With these efforts in mind, the systematic impacts of metallicity on the derived distances are discussed Section 5.4. Other systematic effects are discussed briefly in Section 5.5.

### 5.1 Comparison Case Study in IC1613

We use the compendium of distances to IC 1613 of Hatt et al (2017) for CCs, RRLs, and optical TRGB standard candles; no new distances have been published since this paper (while Madore et al, 2018, uses IC 1613 to calibrate the IR-TRGB, the distance is adopted from Hatt et al.). The references for these comparisons and the shorthand used in the plot are as follows: Mac01 – Macri et al (2001), Dol01 – Dolphin et al (2001), Fre01 – Freedman et al (2001), Uda01 – Udalski et al (2001), Tik02 – Tikhonov and Galazutdinova (2002), Pie06 – Pietrzyński et al (2006), Ant06 – Antonello et al (2006), Fre09 – Freedman et al (2009), Ber10 – Bernard et al (2010a), Sco13–Scowcroft et al (2013), Dam13 – Dambis et al (2013), and Hat17 – Hatt et al (2017). Only a single T2C candidate is known in IC 1613 (Majaess et al, 2009) and, thus, we do not have a distance from T2Cs in this comparison case study; the study itself, however, still reveals the major points to be discussed in the later subsections.

Figure 33 shows independently determined distances to IC 1613 since the *HST* Key Project (Freedman et al, 2001) ordered from top to bottom as CC studies, RRL studies, and TRGB studies. The original distance moduli ( $\mu_0$ ) are plotted with open gray symbols with the CC distances as boxes, RRL distances as circles and TRGB distances as diamonds. As is detailed explicitly by Hatt et al (2017, their table 4), the studies vary considerably in their absolute calibration: for the



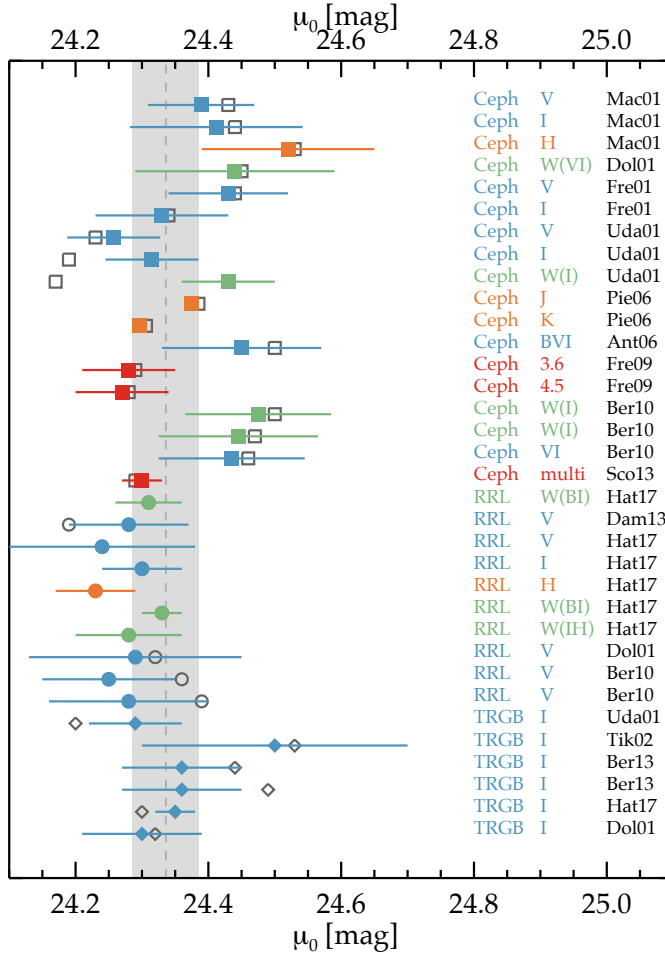


**Fig. 33** Comparison of distances to IC 1613 since the *HST* Key Project using the compendium of Hatt et al (2017, their fig. 9, their table 4). The original measurements are shown as open gray symbols, with Leavitt Law studies as squares, RRL as circles, and TRGB as diamonds. Each study has assumed slightly different zero points and foreground/internal extinctions. The filled symbols display homogenized distance moduli for each study, with the symbols colored by the wavelength range; optical studies in blue, NIR studies in orange, MIR studies in red, and reddening-free Wesenheit studies in green. The consensus distance modulus from de Grijs et al (2014) of  $24.336 \pm 0.049_{stat}$  mag is shown by the dashed line with a region of width  $\pm 0.05$  mag represents representative uncertainties for the absolute scales. Overall this figure demonstrates agreement for the Pop I and Pop II scales and between RRL and TRGB. The distance moduli are homogenized to an LMC distance modulus of 18.49 mag, a total  $E(B - V) = 0.08$  mag for Cepheids) and  $E(B - V) = 0.02$  mag for RRL and TRGB,  $M_I^{TRGB} = 4.00$  mag, and  $M_V^{RRL} = 0.63$  mag; original uncertainties are plotted.

CCs the distance modulus to the LMC varies from 18.25 to 18.54 mag (10% in distance), for RRLs the RRL zp varies from  $M_V^{RRL}=0.52$  to 0.72 (10% in distance), and the TRGB varies from  $M_I^{TRGB}=-3.91$  to -4.13 mag (10% in distance). Similar variations also occur in the Milky Way foreground extinction and the internal extinction for the CCs. Thus, in attempting to address if these Pop II distance indicators set comparable distance scales, we must homogenize for these systematics to prevent the dispersion between studies dominating the comparison.

Following Hatt et al (2017), we normalize to  $\mu_{LMC}=18.49$  mag for the CCs,  $M_V^{RRL}=0.63$  mag and no foreground extinction ( $A_V \sim 0.0$  mag); we deviate from Hatt et al by assuming an mean extinction internal to IC 1613 of  $A_I=0.1$  mag (for the CCs) and  $M_I^{TRGB}=-4.0$  (see discussion in Hoyt et al, 2018; Hatt et al, 2018). The homogenized distance moduli are shown by the filled symbols in Figure 33 and these symbols are color coded by the wavelength regime of the study: blue for optical, orange for NIR, red for MIR, and green for reddening-free relations for the Cepheids and RRL. The overall dispersion within the standard candles and between the standard candles reduces. The mean distance determined from de Grijs and Bono (2014) of  $24.336 \pm 0.049_{stat}$  is shown by the dashed gray line with the filled gray region showing  $\pm 0.05$  mag, which is representative the typical systematic uncertainty on the zero points. The measurements shown here are all within  $2\text{-}\sigma$  of this ‘‘consensus distance,’’ from which we conclude that we see ‘‘overall’’ consistency between CCs, RRLs, and the TRGB in IC 1613. It is worth noting, however, that in terms of the systematic effects, IC 1613 is a simple case: it a metal-poor dwarf galaxy with low internal extinction and low source crowding even in ground-based imaging.

Before discussing these systematic effects in detail, it is worth noting that comparisons between RRL, CCs, T2Cs, and the TRGB are currently only possible for galaxies in the Local Group; only within the Local Group are populations of for all three distance indicators identified (e.g., only the TRGB has been used for distances outside of the Local Group). These four distance indicators can only really be compared in earnest with systems of stellar masses on order of relatively massive dwarf galaxies; Figure 1 demonstrates the difference in the numbers of CCs, T2Cs, and RRLs between the LMC and SMC.

Farther afield, Lee and Jang (2012) provide comparisons between CCs and the TRGB in M 101 (the closest host-galaxy for a modern SN Ia). Lee and Jang find both standard candles scatter over a large range of 0.7 mag (35% in distance) and 0.4 mag (20% in distance), respectively, despite each study quoting uncertainties at the  $\sim 0.1$  mag level (5% in distance) — Lee and Jang did not homogenize for zero points, but these will not fully account for the range. Recent high-precision TRGB studies such as Jang and Lee (2017a), Jang et al (2018), and Hatt et al (2018) compare CCs and the TRGB for SN Ia host galaxies, finding overall agreement, but the bulk of these galaxies have only a single measurement from a single team for each result. Previous work during and after the *HST* Key Project found similar agreement between scales, but the measurements at that time had larger uncertainties (e.g., Ferrarese et al, 2000; Sakai et al, 2004; Freedman and Madore, 2010, among others). With these examples in mind, we now proceed to discuss the systematics affecting the absolute scales and individual distance measurements.

## 5.2 Absolute Scale through Primary Calibration Techniques

Primary calibrations are produced by using individual stars to which distances are determined using geometric methods. These come in three types: (i) trigonometric parallax, (ii) statistical parallax, and, for RRLs and T2Cs, (iii) pulsational parallax. Spectroscopic parallax is another means of determining the distance to an individual star, but it requires a primary calibration from another means and will not be discussed here (e.g., Adams, 1916; Sandage et al, 2016). First, we describe these methods in Section 5.2.1 and then discuss their application to the RRLs in Section 5.2.2, T2Cs in Section 5.2.3, and TRGB in Section 5.2.4.

### 5.2.1 The Methods

#### I. Trigonometric Parallax

First measured by Bessel (1838), trigonometric parallax is the apparent displacement of an object, relative to its background, due having viewed the source from two distinct positions. The size of the displacement is proportional to the separation between the two viewing positions and for astronomical applications, the typical baseline is the Earth’s orbit, e.g., observations are taken  $\sim$ six months apart. From this setup, triangles can be constructed connecting the two viewpoint, the true location for object of interest, and its apparent displacement. Thus, once positions are robustly determined relative to a background frame, the distance is computed using simple geometry. Ground based parallaxes are feasible only for the most nearby stars, and thus, the resolution and stability of space-based observatories are required. A history of the technique and an assessment of ground-based methods is given in Vasilevskis (1966); van Altena (1983); Uppgren (1985).

Major space-based parallax-focused missions are *Hipparcos* (Lindegren et al, 1992; Perryman et al, 1997; ESA, 1997; van Leeuwen, 2007, and references therein) and, more recently, *Gaia* (Perryman et al, 2001; Gaia Collaboration et al, 2016, and references therein). The Fine Guidance Sensor (FGS) on *HST* was designed for astrometric applications (see e.g., Duncombe et al, 1991, and references therein) and been used for parallaxes (for a comprehensive compilation and review of these measurements see Benedict et al, 2017) and, very recently using a primary *HST* instrument, WFC3 (Brown et al, 2018).

#### II. Statistical Parallax

The method of statistical parallaxes is an old one, having been invented by Kapteyn and Kohlschütter in the early 20th century and first published in Adams and Kohlschütter (1914).<sup>10</sup> This technique determines a mean parallax to a group of stars whose proper motions, with the motion of the Sun removed, are analyzed. The observed proper motion, in angular units, is inversely proportional to the distance to the object, so from the analysis of an ensemble of proper motions, the parallax can be determined for the class. A discussion of the mathematics of such a determination is given in Popowski and Gould (1997, and references therein).

<sup>10</sup> A detailed history of these methodological discoveries from the source material is given in Sandage (2004) whereas a briefer summary is more accessible in Sandage et al (2016).

The method was employed often in the 20th century to obtain calibrations for the distance scale, but has fallen slightly out of use as more accurate and precise trigonometric parallaxes have become available.

### III. Pulsation Parallaxes

The method was proposed by Wesselink (1946) based upon earlier suggestions by Baade (1926) and, as a result, has been coined the Baade-Wesselink method. The method combines radius measurements from radial velocity curves with temperature and measurements from light curves to infer the surface brightness, and thereby, intrinsic luminosity of a pulsational variable. The method was founded upon the postulation that at points of equal color on the ascending and descending branches of the light curve, the temperature of the star should be the same, and in consequence, any difference in luminosity at these points is due to the fractional change in radius ( $\Delta R/R$ ). The  $B - V$  color–surface brightness relationship first provided in Wesselink (1969) completed the development phase. A limitation of the method is the need for a term  $p$  coined the “projection factor” that is used to translate between the observed radial velocity and the true pulsational velocity — the radial velocity measured is the motion of the atmospheric line projected along the line-of-sight and integrated across the stellar disk. Thus,  $p$  is a multiplicative factor that can come from theoretical inferences or can be measured directly with interferometric methods (see e.g., recent work for Cepheids see Pilecki et al, 2018; Kervella et al, 2017; Breiterfelder et al, 2016, among others).

#### 5.2.2 Primary Calibration of the RRLs

All three of the direct methods can be applied to RRLs and largely find agreement, albeit most methods produce absolute calibrations at the  $\sim 0.1$  mag level.

*Trigonometric Parallax:* A selection of the major results for calibration of the RRLs via trigonometric parallax are summarized below. It is important to note that *only* in the recent *Gaia* data releases have both the period and metallicity impacts, in addition to the zeropoint, been measurable directly from parallaxes to individual stars. Thus, the future is bright for larger samples of parallaxes to produce a precise and accurate calibration of both the zero-point and the slope of the PLs.

- **Hipparcos:** Most recently, Feast et al (2008) used 142 RRL included in the *Hipparcos* re-reduction (van Leeuwen, 2007) found  $M_V^{RRL} = 0.59 \pm 0.10$  mag (adjusted to  $[\text{Fe}/\text{H}] = -1.60$  dex). For the NIR, Feast et al found  $M_{K_s}^{RRL} = -0.63 \pm 0.10$  mag at a fiducial  $\log(P) = -0.252$  and assuming  $\text{PL}_{K_s}$  slope to be  $-2.41$ . Other studies using the original *hipparcos* reduction include: Fernley et al (1998), Feast (1998), Solano (1998), Luri et al (1998), Koen and Laney (1998), Groenewegen and Salaris (1999), and Reid (1999), among others.
- **HST-FGS:** Benedict et al (2011) presented *HST*-FGS parallaxes to 5 RRL (4 RRab and 1 RRc) to precisions of  $< 10\%$ . In Benedict et al (2011), itself, the zero point is  $M_V = 0.42$  at  $[\text{Fe}/\text{H}] = -1.58$ , which is systematically lower than other techniques. Considering, however, the small sample size, the zero-point could be biased by evolutionary effects, e.g., even a single egregious star could bias the result. While these parallaxes were the best for the RRL, most works

employed a dual theoretical-empirical procedure to determine zeropoints, which are described in the case studies in Section 2.3, and typically yield results more consistent with other techniques.

- ***Gaia* Data Release 1 (TGAS):** The first *Gaia* data release included parallaxes from the Tycho-Gaia Astrometric Solution (TGAS), which contained parallaxes for all 142 RRL in *Hipparcos* with some additional stars in the *Tycho* catalog. Neeley et al (2017) demonstrated use of 46 well characterized RRL in TGAS provided constraints on the zero point for the MIR PL at the same precision as the smaller, but more precise, sample from *HST*-FGS. Notably, Neeley et al (2017) argued that these data necessitated metallicity term to comply with theoretical predictions. Sesar et al (2017), found similar results, but using larger samples and a Bayesian inference method for the  $W1$  and  $W2$  bands fitting for slope, metallicity, and zero-point; this paper found both consistent and inconsistent results as compared to other studies, but also issued caution on the reliability of the abundances.
- ***Gaia* Data Release 2 (DR2):** The second *Gaia* data release included a  $< 10\%$  parallaxes for several thousands of RRL. Muraveva et al (2018a) exploited 401 of these RRL that had sufficient characterization in the literature to derive full PLs in a Bayesian framework for the  $V$ ,  $G$ ,  $K_s$  and  $W1$  bands; here the limiting factor on the sample is the existence of non-*Gaia* measurements including photometry, extinctions, abundances, and long-baseline periods. Muraveva et al (2018a) find:  $M_V = 0.66 \pm 0.06$  mag,  $M_G = 0.63 \pm 0.08$  mag,  $M_{K_s} = -0.37 \pm 0.11$  mag, and  $M_{W1} = -0.41 \pm 0.11$  mag for a fiducial  $P=0.5238$  days and  $[\text{Fe}/\text{H}]=-1.5$  dex. Despite the larger sample and better parallaxes, the uncertainties on the zeropoints remain at the 0.1 mag level. Additional work is likely forthcoming from other teams and employing other wavebands.

*Statistical Parallax:* Because RRLs have a small-to-negligible period dependence in the optical, the absolute magnitude can be approximated to a single value and statistical parallax can be applied. A summary of these efforts at that time is given in Smith (1995) and since that time less effort has been employed for this measurement. Popowski and Gould (1998a,b); Gould and Popowski (1998) employed a rigorous mathematical framework that incorporated observational biases directly to find  $M_V^{RRab} = 0.75 \pm 0.13$  mag at  $[\text{Fe}/\text{H}] = -1.61$  dex for the Layden et al (1996) sample and  $M_V^{RRab} = 0.77 \pm 0.13$  at  $[\text{Fe}/\text{H}] = -1.60$  dex for a sample of 147 kinematically-selected halo RRL. Using the larger ASAS all sky sample of variables, Kollmeier et al (2013) produced the first calibration of the  $M_V^{RRc}$  using statistical parallax, finding  $M_V^{RRc} = 0.59 \pm 0.10$  mag for a mean metallicity of  $[\text{Fe}/\text{H}] = 1.59$  dex. Such methods do not perform as well where there is a period dependence, because the statistical samples must be restricted to period ranges, which reduces precision.

*Pulsation Parallax:* As discussed in Smith (1995), the foundational assumption of the Baade-Wesselink method regarding equal colors implying equal temperatures fails for the RRL because, in part, of RRL shocks that perturb the color-curves in the optical. Longmore et al (1985) noted that  $K$  observations provided better results for the RRLs and after that time the NIR results were used for such analyses. Compilations of pulsation parallaxes can be found in Liu and Janes (1990), Cacciari et al (1992), and Skillen et al (1993). Muraveva et al (2015) used 23 pulsation parallaxes to derive the  $\text{PL}_{K_s}$  relationship and found the zero-point to agree well

with those determined from the LMC, but disagree with that determined from Benedict et al (2011).

There is only one star common to each of these means of measuring the parallax: SU Dra. The pulsation parallax of Liu and Janes (1990) finds a distance of 640 pc or  $\pi = 1.56$  mas with an uncertainty on the absolute magnitudes of 0.12 mag, that translates to a  $\sim 12\%$  uncertainty on the parallax of  $\sim 0.18$  mas. The *Hipparcos* re-reduction found  $\pi_{trig} = 0.20 \pm 1.13$  mas (van Leeuwen, 2007) compared to the initial result of  $\pi_{trig} = 1.11 \pm 1.15$  mas Perryman et al (1997). The *Gaia* DR2 value is  $1.4016 \pm 0.0308$  mas, whereas Benedict et al (2011) finds  $1.42 \pm 0.16$  mas. From comparison of a single star, there is overall agreement within the uncertainties as was demonstrated for the *body* of *HST*-FGS parallaxes against *Gaia* by Benedict et al (2017, 2018). Thus, interpreting differences between zero-points determined in different contexts may be better framed as comparisons between assumptions of the PL-form, sample size, and abundances, rather than the fidelity of the parallaxes themselves.

### 5.2.3 Primary Calibration of the T2Cs

The body of work on the primary calibration of the T2Cs is much smaller than that of RRL and they are discussed with respect to two key stars: VY Pyx and  $\kappa$  Pav that have parallax measurements from multiple techniques.

Feast et al (2008) used *Hipparcos* trigonometric parallaxes for VY Pyx (BL Her type with  $P = 1.24$  days) and  $\kappa$  Pav (W Vir type with  $P = 9.09$  days), as well as pulsation-based parallaxes for a few T2Cs to see if their absolute magnitudes based on the parallaxes were consistent with the PL relations derived by Matsunaga et al (2006) for T2Cs in GGCs. Their *Hipparcos* parallaxes led to the absolute infrared magnitudes more-or-less predicted by Matsunaga et al (2006), although the pulsation parallax of  $\kappa$  Pav had a significant offset for which the authors gave cautions for both the pulsation and trigonometric parallax (which still had a large uncertainty). Feast (2010) later suggested that  $\kappa$  Pav may be of peculiar W Vir type, which are, indeed, intrinsically brighter than expected by the PL relation for the W Vir type.

Benedict et al (2011) reported *HST*-FGS parallaxes for the same two T2Cs, VY Pyx and  $\kappa$  Pav, with significantly smaller parallax uncertainties than those from *Hipparcos*. Despite the lower uncertainties, these new measurements left the questions unresolved; using the *HST*-FGS parallaxes,  $\kappa$  Pav seems to follow the PL relation, but VY Pyx, in turn, is fainter than anticipated. Breitfelder et al (2015) found that the *HST* parallax of  $\kappa$  Pav leads to p-factor consistent with other Cepheids based on their interferometric and spectroscopic data. Breitfelder et al (2015) also found no evidence of binarity for this object, which would have been a strong clue that the star was of a peculiar type. These new results suggest that  $\kappa$  Pav is a normal W Vir, not a peculiar W Vir, and, thereby, should follow the PL relation of the W Vir type. The nature of VY Pyx, however, remained unclear.

*Gaia* DR2 offers more insight, finding for  $\kappa$  Pav,  $\pi = 5.1992 \pm 0.3094$  mas and for VY Pyx,  $\pi = 7.1173 \pm 0.0265$  mas. Figure 34 compares the parallax results from *Hipparcos*, *HST*-FGS, pulsation parallaxes, and *Gaia*-DR2 for these two T2Cs. The prediction from the PL of Matsunaga et al (2006) is plotted with the uncertainty

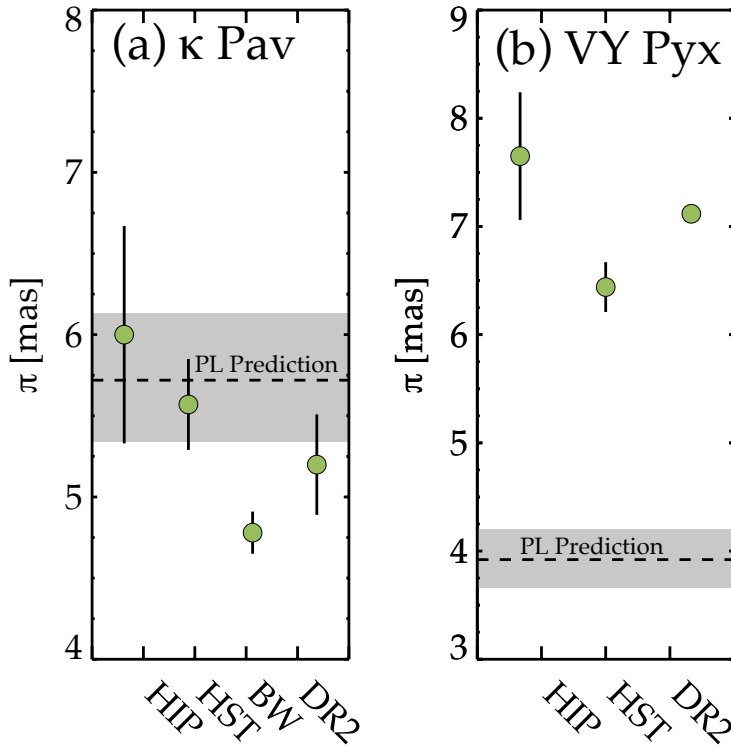


**Fig. 34** Comparison of geometric distance measurements to the T2Cs (a)  $\kappa$  Pav ( $P=9.09$  dy) and (b) VY Pyx ( $P=1.2$  dy) to the predicted parallax from the Matsunaga et al (2006)  $K_s$ -PL relation. The shaded region gives the scatter about the Matsunaga et al (2006) PL ( $\pm 0.15$  mag) from the GGCs. While  $\kappa$  Pav is largely consistent with the PL, VY Pyx is quite deviant.

of the zero-point in gray; the dashed line represents if the star is directly on the PL (e.g., no intrinsic dispersion). The trigonometric parallaxes for  $\kappa$ -Pav, Figure 34a, are all consistent with Matsunaga et al (2006), whereas the pulsation parallax is several sigma away. There is no pulsation parallax for VY Pyx, but the trigonometric parallaxes in Figure 34b are all inconsistent with the Matsunaga et al (2006)-PL. Thus, the nature and classification of VY Pyx likely requires further study. As with the RRL, this comparison highlights the need for parallaxes to a *representative* sample of stars to infer PLs instead of relying on individual stars as a prototype for a class, e.g., the *intrinsic dispersion within the class* may be large.

#### 5.2.4 Primary Calibration of the TRGB

At the time of writing, the authors are only aware of a single study to provide a primary calibration of the TRGB. Tabur et al (2009) combined *Hipparcos* and 2MASS data to provide a preliminary calibration of the TRGB absolute magnitude in  $K_s$ , finding  $M_K = -6.85 \pm 0.03$  mag. This study, however, has a number of caveats: (i) for the bright stars populating the tip, most of the magnitudes were derived from DIRBE because such stars in 2MASS had large (0.2 mag) uncertainties due to sat-

uration, (ii) the *Hipparcos* parallaxes have extremely large errors ( $\gg 20\%$ ), and (iii) the authors only fit for a single color bin. Moreover, the authors do not use a Bayesian approach to determining distances using parallaxes with large uncertainties as is recommended (see e.g., Bailer-Jones, 2015). As mentioned in Tabur et al (2009) with respect to *JHK*, the current limitation for direct measurement of the TRGB is the lack of homogeneous photometry for bright stars in the bands of interest for the TRGB – primarily, *I* and *JHK*. Such work is challenging because these stars cannot be identified a priori as tip stars and the nearby stars with the most precise parallaxes are saturated in most modern surveys. Thus, even with the wealth of parallaxes from *Gaia*-DR2, this measurement remains elusive.

### 5.3 The Absolute Scale via Secondary Calibration

Secondary calibration works in two steps: (i) establish the distance to an object, like a star cluster or nearby galaxy, using a geometric technique and (ii) determine the absolute magnitude of the standard candle using samples from that object. Thus, the absolute scale set has two components to the systematic uncertainty: (i) the total uncertainties from the geometric technique and (ii) the uncertainties from the standard candle. It is also possible to combine other standard candles to obtain a secondary calibration, which adds another layer of systematic uncertainty; for brevity, we will not include those results here though some discussion exist in the sections for each distance indicator.

In this volume, Thévenin et al (2017) describe “modern” geometric techniques, which includes a number of different methods – to which methods relying on gravitational waves can be added (e.g, Chen et al, 2017), which are also described in this volume by Czerny et al (2018). However, of those only two are applicable on the distance scales to directly calibrate the Pop II distance indicators described here, (i) eclipsing binaries and (ii) mega-masers (only for the TRGB). As for the primary calibration, we give the general sense of the methods in Section 5.3.1 before describe application to the RRLs in Section 5.3.2, T2Cs in Section 5.3.3, and TRGB in Section 5.3.4.

#### 5.3.1 Methods for Secondary Calibration

##### *I. Eclipsing Binaries:*

Eclipsing binaries (EBs) are a set of binary star systems where the binary orbit is sufficiently along the line-of-sight that the one star eclipses the other. Detached eclipsing binaries (DEBs) are a subset of EBs for which both stars are entirely within their respective Roche Lobes, meaning that the stars can be modeled as a simple two-body system. Using a combination of (i) light curve analyses for the inclination, relative radii, and relative luminosity and (ii) radial velocity curves, both masses and the separation of the binary can be determined in absolute units. The best DEBs for distances have two eclipses and one of the eclipses is “complete” or nearly so (see discussion in Kaluzny et al, 2005). From the absolute separation, the radii of the two stars can be solved for, which, using a surface brightness–radius relation (e.g., di Benedetto, 1998; Graczyk et al, 2017), can be converted



into a luminosity, and hence, a distance. The precision of the surface brightness–radius relation is a function of the stellar type and luminosity class, with late-type binaries being those with more well-defined relations. The surface brightness–radius relation can only be calibrated for stars in the Solar neighborhood, which could impart age or metallicity biases, but so far the relationship shows only mild sensitivity to metallicity (Houdashelt et al, 2000).

A summary of EB results in GGCs can be found in Kaluzny et al (2005). Since then EBs have been found in, monitored in, and distances derived to: NGC 6362 ( $14.74 \pm 0.04$  mag Kaluzny et al, 2015), M 4 (Kaluzny et al, 2013, see Section 2.3), 47 Tuc ( $13.35 \pm 0.08$  mag Thompson et al, 2010), NGC 6397 (11.65 mag Rozycka et al, 2014),  $\omega$  Centauri ( $14.05 \pm 0.11$  mag Thompson et al, 2001), and M 55 ( $13.94 \pm 0.05$  mag Kaluzny et al, 2014) within the context of the Clusters AgeS Experiment (CASE), which is also monitoring a number of other nearby GGCs.

An extragalactic census of EB results is given in Bonanos (2013) and includes sources detected in NGC 6822, IC 1613, LMC, SMC, M 31, and M 33; distances have been determined from the EBs in all but NGC 6822 and IC 1613. A 2% distance to the LMC using eight DEBs was published in Pietrzyński et al (2013), with modeling of an additional 12 systems recently published in Graczyk et al (2018) for a total of 20 DEBs in the LMC. A distance to M 33 with 1 DEB was given in Bonanos et al (2006). A distance modulus of  $\mu_{M33} = 24.92 \pm 0.12$  mag ( $964 \pm 54$  kpc) was found. A distance to M 31 using 2 DEBs was published in Vilardell et al (2010). Since then, several hundred EBs have been discovered in the M 31 field (e.g., 298 from Lee et al, 2014), of which only 11 are bright enough for radial-velocity follow-up (e.g.,  $V < 20.5$  mag for 8-10m class telescopes) and consistent with being in M 31. Eclipsing binaries provide an excellent means of calibrating zero points, but only in systems with well populated sequences and accompanying information on the metallicity effects.

## II. Megamasers in Accretion Disks:

The Local Volume galaxy, NGC 4258, hosts a megamaser in the accretion disk of its central black hole. The accretion disk is thought to be nearly edge-on and the emission from the megamaser traces the motion of the gas in the disk. Long-term monitoring of the megamaser emission produces a velocity field and with the assumption of Keplerian motion in the disk, a physical radius can be calculated and a geometric distance determined. Further methodological details can be found in this volume by Thévenin et al (2017).

Since its discovery, seven distances to NGC 4258 have been published:  $28.66 \pm 0.47$  mag (Greenhill et al, 1995),  $29.03 \pm 0.29$  mag (Miyoshi et al, 1995),  $29.29 \pm 0.08$  mag (Herrnstein et al, 1999),  $29.29 \pm 0.02$  mag (Humphreys et al, 2008), 29.31 mag (no uncertainty was given) (Riess et al, 2012),  $29.40 \pm 0.05$  mag (Humphreys et al, 2013),  $29.39 \pm 0.06$  mag (Riess et al, 2016). While early results had large uncertainties as the methodology was being developed, the last four publications cite  $< 2.5\%$  uncertainties distance, but differ at the 5% level. The physical distances span from 7.2 Mpc to 7.6 Mpc (Jang and Lee, 2017a).

### 5.3.2 Secondary Calibration of the RRLs

RRL calibration in globular clusters has been performed in M4 in the NIR and MIR. Reasonable agreement between EBs and RRL distances from trigonometric parallaxes were found for M4. Many of the clusters with EB distances also have samples of RRL (Clement et al, 2001a).<sup>11</sup> A benefit of the GGCs as calibration objects is their small age and metallicity ranges, which allows comparisons to be made for these parameters. At the same time, however, the use of mono-abundance and mono-age relations is not applicable to mixed populations; albeit  $\omega$  Centauri is one exception (for detailed discussion see Braga et al, 2018). Thus, so far use of geometric EB distances for direct calibration of RRL remain poorly utilized; whereas, non-geometric distances (isochrone fitting, mean HB magnitude, and others) are used more frequently.

Performing direct calibration of the RRLs in the LMC and SMC is challenging due their line-of-sight depth and lack of clear information on how to address internal extinction; moreover, the RRL have  $V \sim >18$  mag, which requires large telescopes for direct abundances. Nevertheless, Muraveva et al (2015) performed a calibration using 70 LMC RRL, finding it to agree well with pulsation parallaxes, but disagree with the *HST*-FGS parallax sample. There are reasonably large samples of RRLs in IC 1613, M33 and M31, typically detected via *HST*, but these are largely still used to determine the distance to these objects rather than to calibrate the RRL themselves (see e.g., Sarajedini et al, 2006, 2009; Bernard et al, 2010b, among others). Again, the RRL at the distance of M31 are at  $V > 25$  mag and are out of range for most spectroscopic facilities as well as being difficult to obtain sufficient sampling to apply photometric techniques for metallicity.

### 5.3.3 Secondary Calibration of the T2C

A tabulation of T2Cs in GGCs is given by Matsunaga et al (2006, their table 2) and it contains 46 individual T2Cs in 26 different clusters, of which only 12 clusters contain more than a single T2C. Unfortunately, the list of clusters *with* T2Cs and *with* geometric distances is disjoint; Matsunaga et al (2006) calibrated their relations to the magnitude of the horizontal branch. A large sample of T2Cs exist in the LMC and SMC and the geometric distances to these galaxies were the basis for relations derived in Section 3.4.

### 5.3.4 Secondary Calibration of the TRGB

GGCs are not ideal objects to calibrate the TRGB because their stellar mass is sufficiently small that it is not guaranteed that there will be a true TRGB star. The EBs in extragalactic systems, however, make good sources of calibration; the LMC EB distance is used routinely, both Górski et al (2016) and Hoyt et al (2018) use the LMC to calibrate the IR-TRGB and Jang and Lee (2017a) uses the LMC in the optical.

---

<sup>11</sup> An impressive and detailed tabulation of all known variables in clusters, which includes RRL, T2Cs, and EBs among other types, has been updated by Christine Clement regularly for many years and is available at this URL: <http://www.astro.utoronto.ca/~cclement/cat/listngc.html>

The TRGB can be independently calibrated with NGC 4258 using *HST*. The TRGB measurements are as follows:  $F814W^{TRGB} = 25.20 \pm 0.06$  mag (WFPC2),  $F814W^{TRGB} = 25.24 \pm 0.04$  mag (ACS) (Mager et al, 2008), 25.25 (with 90% confidence interval from 25.23 to 25.38) and  $25.22 \pm 0.09$  mag (Mouhcine et al, 2005),  $F814W^{TRGB} = 25.39 \pm 0.11$  mag (Madore et al, 2009), and  $F814W_0^{TRGB} = 25.357 \pm 0.031$  mag (Jang and Lee, 2017b). Thus, the individual TRGB measurements span from 25.20 to 25.357 mag, a span of 7% in distance. For this reason, Jang and Lee (2017a) perform a through comparison using different photometry packages and different techniques for determining the point-spread-function finding differences between studies at the 0.05 mag level, which agrees with earlier comparisons in NGC 4258 in Mager et al (2008). Taken in conjunction with the other measurement uncertainties discussed in Section 4.2, the difference in the TRGB magnitudes can largely be explained.

Given the variation in TRGB detections and the variation in the distances themselves, whether or not a TRGB calibration in NGC 4258 agrees with other techniques is largely dependent on which studies are compared. Rizzi et al (2007) note that the Humphreys et al (2005) distance to NGC 4258 calibrates the TRGB to be 2.3- $\sigma$  fainter than their determination from other sources. Beaton et al (2016) note the opposite effect via the distance from Humphreys et al (2013), finding  $M_I^{TRGB} = -4.16 \pm 0.06_{stat} \pm 0.04_{sys}$  mag, which is systematically more luminous. Jang and Lee (2017a) ultimately find  $M_{F814W}^{TRGB} = -4.03 \pm 0.07$  mag using Riess et al (2016), which is consistent with other ground-based calibrations.

#### 5.4 Metallicity

Theoretical and empirical investigations suggest that metallicity impacts the absolute magnitude for each of our Pop II standard candles. In many ways, age and metallicity are coupled. The impacts are two-fold: (i) metallicity impacts the physical structure of the star, which in turn, changes how it evolves and (ii) the metals in the atmosphere selectively absorb and thermally re-emit flux in specific bands. The impact of metallicity can be subdivided into two challenges: (i) difficulties in obtaining direct and/or independent measurements, and (ii) the use of distinct metallicity scales between calibration and application studies. The former point is distance indicator specific and will be discussed in subsections, whereas the latter is more general and will be discussed here.

The two common metallicity scales for Galactic work are those of (i) Carretta-Gratton (Carretta and Gratton, 1997) and (ii) Zinn-West (Zinn and West, 1984). The Zinn and West scale was established using a variety of “integrated parameters” in GGCs, including the integrated line index ( $Q_{39}$ ) and the infrared Calcium Triplet (CaT), to set a scale for [Fe/H]; this choice was motivated by the desire to establish a homogeneous scale that could work for both nearby and distant objects, but comes at the cost of these integrated techniques not being always correlated directly with the quantity [Fe/H], itself (e.g., see Hayden et al, 2015, for visualizations of how different elements do or do not correlate with Fe across the Galaxy). Carretta and Gratton used a smaller sample of objects (24 GGCs), but used higher resolution spectroscopy to produce metallicity measurements from Fe lines as well as other elements that contribute to integrated techniques.

A comparison between Zinn and West and Carretta and Gratton is given in Carretta and Gratton (1997, their figure 5) that shows a non-linear correlation between the two studies in addition to a zero-point offset due to adjustments to the solar Fe abundance, finding:

$$[Fe/H]_{CG97} = -0.618 - 0.097[Fe/H]_{ZW} - 0.352[Fe/H]_{ZW}^2 \quad (27)$$

with a scatter of  $\sigma=0.08$  dex and uncertainties on the coefficients of  $\pm 0.083$  for the zeropoint,  $\pm 0.0189$  for the linear term, and  $\pm 0.067$  for the quadratic term. As an example, a star with  $[Fe/H] = -1.8$  dex on the Zinn and West scale corresponds to  $[Fe/H] = -1.7$  dex on the Carretta and Gratton scale, with the differences being larger on the metal-poor and metal-rich ends of the scale. Thus, the impact of using different metallicity scales may be complex.

#### 5.4.1 Metallicity Impacts in RRL:

Solid theoretical (Marconi et al, 2015) and semi-empirical (Neeley et al, 2017) evidence show that the mean magnitudes of the RRLs in all the optical-NIR-MIR photometric bands are affected by their iron abundance—the more metal-poor the variable is, the brighter. The metallicity coefficient of the PL relations ranges from 0.14 to 0.19 mag dex<sup>-1</sup> (Marconi et al, 2015; Neeley et al, 2017) in the optical, NIR and MIR, showing no clear trend with wavelength. It is, however, important to note that the intrinsic dispersions for the long-wavelength PLs is smaller than the theoretical separation between  $\sim 0.5$  dex populations, implying the effect should be more easily distinguished for the longer-wavelength data (see discussions in Neeley et al, 2017). Thus, metallicity is fundamental for the distance determination using RRL.

Direct spectroscopic metallicity measurements in RRL are complicated due to the short timescales over which the atmospheres are changing. Typical radial velocity amplitudes are  $\sim 50$  km/s (see, e.g., Sesar, 2012, and references therein) such that even short observations ( $\sim 10$  min) can be impacted by line blurring. Thus, spectroscopic observations are either conducted at specific phases or use techniques employed at specific phases to infer the metallicity. Some common alternate techniques include:

- **$\Delta S$  method:** Preston (1959) developed a technique that infers metallicity using a combination hydrogen lines to infer the spectral type (e.g., temperature) and Ca II H and K lines to infer the metallicity known as the  $\Delta S$  method. The method is typically only applied at minimum light. Narrow-band filters can be used for the specific lines used in this technique (see Rey et al, 2000). The recalibration by Clementini et al (1995) using high resolution spectra, which was revisited by Carretta and Gratton (1997) to find (on their scale):

$$[Fe/H] = -0.187(\pm 0.011) \Delta S - 0.088(\pm 0.04) \quad (\sigma = 0.269) \quad (28)$$

- **Fourier coefficients:** Kovacs and Zsoldos (1995); Jurcsik and Kovacs (1996); Smolec (2005, and references therein) demonstrate a correlation between Fourier coefficients, in particular,  $\phi_{31}$ , and metallicity. The Smolec (2005) calibration is tied to the Zinn and West (1984) metallicity scale and is based on 28 stars:

$$[Fe/H]_{phot} = -3.142(\pm 0.646) - 4.902(\pm 0.375) + 0.824(\pm 0.104)\phi_{31} \quad (29)$$

- Wallerstein (2002) demonstrated a technique based on the Calcium triplet (CaT), which is commonly used in moderate resolution spectroscopy for red giants.

Direct measurements, however, can be performed if care is taken in the data acquisition and subsequent analysis. Of particular note is a series of papers that use high cadence spectroscopic datasets obtained for the full cycle of several RRL. For et al (2011b,a) use an iterative procedure to estimate the temperature for each spectrum and then perform direct spectral analyses for numerous chemical species. Both Govea et al (2014) and Sneden et al (2018) continue this work for RRc variables with continued success. These direct measurements show relative consistency for stellar parameters and abundances derived self-consistently from the spectrum at all phases. Comparison of these parameters to other, more common methods have not yet been produced, but are important.

#### 5.4.2 Metallicity Impacts in T2Cs:

The metallicity effects are less well constrained for T2Cs. A major concern, however, is the proposed shifting of  $P$ -boundaries between the sub-types apparent in the LMC and SMC. The shift in sub-population classification would be a major systematic given the differences in the PLs derived with different sub-samples.

The first chemical abundance analysis for BL Her and W Vir type T2Cs was presented in Maas et al (2007) for 19 field stars, finding anomalous chemical compositions similar to previous studies of RV Tau stars by Giridhar et al (2005). Subsequent analyses have focused on using spectral features and chemical abundances as means to cleanly separate the sub-populations; examples include, (i) Kovtyukh et al (2018a) see differences in the metal-poor populations for short period T2Cs ( $P < 3$  day), (ii) Kovtyukh et al (2018b) that compares W Vir abundances to those of the disk, suggesting the W Vir stars to be He-enhanced, and, (iii) Lemasle et al (2015b) that compare W Vir stars to CCs. On the whole, the spectroscopic studies are more focused on the revealing the evolutionary origin of these stars rather than their use as distance indicators. Along this line-of-thinking, Welch (2012) note that additional T2C spectroscopic studies, both for radial velocity monitoring and for chemical abundance measurements, could yield significant insight into binary evolution formation channels.

#### 5.4.3 Metallicity Impacts in TRGB:

The impact of metallicity on the TRGB was discussed in Section 4. While theoretical studies see the effects of metallicity cleanly for bolometric quantities, there are uncertainties when translating these effects into observable quantities. Empirical studies, on the other hand, can measure the color-magnitude behavior, but largely infer the metallicity dependence from the mean metallicity of the system determined from other means (e.g., as in Valenti et al, 2004; Dalcanton et al, 2012). However, the age and metallicity effects are difficult to disentangle. A benefit, however, is that the color-magnitude relationship for the TRGB can be constrained empirically from high signal-to-noise observations irregardless of the physical origin (e.g., as in Jang and Lee, 2017b; Madore et al, 2018). If the color-magnitude

relationship holds in systems comprised of different stellar populations and independently determined distances such that systematics can be estimated (e.g., as in Jang and Lee, 2017b), then impacts can be managed in application to distances.

### 5.5 Other Systematics

We list briefly other systematic terms and strategies used to compensate for them.

1. *Milky Way Extinction:* The foreground extinction needs to be determined. For extra-galactic objects, the Milky Way foreground is well-enough constrained by Schlegel et al (1998) maps (noting the recalibration by Schlafly and Finkbeiner, 2011). Internal to the Milky Way, the line-of-sight extinction is more difficult to constrain. Means of addressing this issue include: (i) RJCE method (Majewski et al, 2011), (ii) models (e.g., Drimmel et al, 2003), (iii) use of Wesenheit formulations (e.g., Madore, 1982), and (iv) using longer wavelengths where extinction has a lower total impact.
2. *Internal Extinction:* Tracers that are located inside external galaxies have an additional component from the extinction due to the external galaxy. This is difficult to constrain independently. Means of addressing this issue include: (i) use of Wesenheit magnitudes (Madore, 1982), (ii) using longer wavelengths where extinction has a lower impact, (iii) using multi-wavelength observations to fit for total extinction directly, (iv) avoiding galactic structures where extinction is likely to be a significant effect (e.g., stellar halos). These techniques has been employed extensively for CCs, with the volume of literature growing for the RRLs.
3. *Non Universality of the Extinction Law:* There is some evidence that “Cardelli’s Law” is not universal, in particular in regions of high gas density (see discussions regarding M4 in Sections 2.3.2 and 2.3.3). Wesenheit magnitudes are not useful in this situation because they have to assume a form of the extinction law. Thus, only observations at longer wavelengths or observations where dust is not anticipated (e.g., stellar halos) are robust to this systematic.
4. *Crowding or Blending:* Measurements undertaken in crowded fields have to contend with flux-contamination from neighboring sources. There are algorithms that can attempt to account for this effect. Photometry packages have been designed with measurement techniques, the following packages are notable: (i) the DAOPHOT family of routines does a particularly good job in crowded regions (Stetson, 1987, 1994), (ii) DOPHOT (Schechter et al, 1993), and (iii) DOLPHOT (Dolphin, 2000). Riess et al (2016, and references therein) use a modeling approach that uses higher resolution optical images to guide source isolation at lower resolutions (typically, longer wavelengths), but this assumes that the same sources are detected in both bands and, may, neglect the fact that different stellar populations dominate the light in optical and IR band-passes. Template fitting may help to identify variable stars that have abnormal shapes due to contamination. **A recent instance of crowding strongly biasing a distance measurement is discussed by van Dokkum et al (2018a), who demonstrates how blended stars may have led Trujillo et al (2018) to infer the wrong distance to the galaxy NGC1052DF2, a galaxy suspected of having a low dark matter mass (van Dokkum et al, 2018b).** Thus, the best means of avoiding crowding/blending is to avoid high-density

regions of galaxies to which Pop II distance indicators are particularly well suited.

5. *Evolutionary Effects:* These effects largely include mixing stars of the same type that are in different evolutionary states due to evolution within the class (e.g., first and second pass HB stars), evolution over time (changes to He abundance), and the possibility that some pulsators come from binary evolution formation paths. These types of effects can either add scatter to a population when their numbers are small or strongly bias a distance when their numbers are comparable to non-evolved sub-types. Sculptor (Section 2.3.1) and  $\omega$ -Centauri (Braga et al, 2018) with their wide metallicity and age spreads are good examples of where evolutionary effects may come into play to skew the means; in populations, however, these outliers can often be identified. Strong biases are more likely when working with individual field stars, where inferring evolutionary state is more complex and, indeed, this is cited for reasons why individual parallaxes might disagree with other forms of calibration (Section 5.2.1). Addressing systematics of this nature can only be accomplished by calibrating the standard candles with large statistical samples and in a variety of environments where various impacts are more or less likely to be a factor (e.g., comparison of calibrations determined using field stars, GGCs, and dwarf galaxies).
6. *Contamination:* Samples can be contaminated by non-standard candles. For the TRGB, contamination can come from AGB stars or from younger red, luminous populations. These effects are mitigated by applying the technique in Pop II dominated regions or by increasing uncertainties. Both RRL and T2C populations can be contaminated by variables with similar periods (indeed the T2Cs and RRL overlap with other variable types) or by unidentified atypical pulsators (e.g., pW VIr, multi-periodic RRLs, Blashko stars). Moreover, both period determination and variable classification are difficult with sparsely sampled data. It is not uncommon for variables to be reclassified with additional data (e.g., see notes in Clement et al, 2001b).

## 6 Summary and Future Prospects

We have developed complementary physical and empirical portraits of three Pop II standard candles: the RRLs, the T2Cs, and the TRGB. In particular, this chapter has put emphasis the history and evolution of these stars as distance indicators, with a particular focus on multi-wavelength use of these tracers. In the course of preparing this chapter, parallels between these Pop II distance indicators have become apparent. There are several “themes” that can be used to discuss our current understanding of these standard candles and these “themes”, in turn, relate directly into the future potential of these objects in the coming years. Thus, we will summarize the chapter and comment on the future prospects in tandem.

First, each of these distance indicators has a deep history dating back to the early days of stellar population research; indeed, often to before the term “stellar populations” had been coined (e.g., Baade, 1944, 1958a). As a consequence, empirical evidence and theoretical understanding have leap-frogged with each other over time. These Pop II standard candles have each played a significant role in our understanding of the structure of our Galaxy and of the Universe and have

had their role in refining the distance scale. Moving forward, it is vital to not forget the formation of the historical nomenclature and the drivers of the historical thinking that led exploration (or a lack of exploration) for these distance indicators. Stated differently, it is important to look back to understand when and why assumptions were made or not made as we work with ever better datasets in which previously “negligible” effects may be transformed into major hurdles. In our historical discussions, we hope to have illuminated some of these previously hidden effects.

Second, none of these Pop II standard candles have a robust geometric foundation. While the RRL and T2C have some parallaxes from targeted studies, these are few in number and cannot fully encompass the intrinsic star-to-star variance nor account for systematic differences (e.g., those due to metallicity or age). Moreover, without a large geometric parallax sample, it is impossible to measure all of the desired quantities for even the simplest calibration (e.g., slopes and zero points). Instead, it is typical to combine theoretical, empirical, and semi-empirical techniques to determine distances to take into account systematics; more specifically, making combinations of slopes and zero-points either measured in different objects or that are predicted from theoretical modeling. While these are incredibly logical to the experienced practitioners, it has the impact of being confusing and inelegant to the non-expert, while also potentially imparting systematic effects between studies.

With the pending data releases from *Gaia*, however, this theme has a bright future. The end-of-mission predictions for *Gaia* are 10% parallax uncertainties at a distance of 10 kpc (de Bruijne et al, 2014), which will provide an unprecedented sample of stars from which to establish a geometric foundation for each of our Pop II indicators. In addition, *Gaia* will provide precise spectro-photometry for all sources, variability information, and, for bright ( $G < 15$ ) sources, spectroscopic parameters (including, chemical abundances and temperatures). The enormity of the *Gaia* dataset is simply mind-boggling and has the potential to reveal not just the practical application of these tools, but also elucidate aspects of stellar theory. During the preparation of this manuscript, *Gaia* DR2 occurred and some of the early results have been included herein, which is undoubtedly only a small fraction of those to occur.

Third, the most pressing questions in both theory and in practice are related to the need to fundamentally understand the impact of metallicity, age, and evolutionary effects for using these stars as standard candles. Addressing these issues will come on two fronts: (i) observations of individual field stars and (ii) observations of populations in star clusters or nearby dwarf galaxies. Thus, addressing this issue will likely require more than just *Gaia* generated datasets.

For the field stars, diving into stellar parameters (temperature,  $\log(g)$ , and chemical abundances) will likely involve the full pantheon of large scale spectroscopic surveys, including but not limited to APOGEE (Majewski et al, 2017), RAVE (Steinmetz et al, 2006), LAMOST (Zhao et al, 2012), GALAH (Martell et al, 2017), and their numerous successors. These surveys, however, have to properly target and process data for stars whose fundamental parameters or observed radial velocity are changing on timescales as short as 10 minutes (for the RR Lyrae). Thus, standard processing may not be sufficient to provide high fidelity measurements. These types of data will fundamentally improve models, while also helping to push the precision of these standard candles to new ends. Moreover, fully



complementary insight can be gleaned from precision high cadence photometry, in particular asteroseismic analyses enabled from *Kepler* (Borucki et al, 2010), *K2* (Howell et al, 2014), and *TESS* (Ricker et al, 2015). These photometric datasets provide an alternate means of determining some stellar parameters via asteroseismology, while also providing short and long timescale variability information to better identify contaminating populations.

For clusters and satellites, many of these large scale programs do not always have sufficient sensitivity and resolution. Here the greatest insight is likely to be gained by leveraging insights from the field star analyses to larger aperture facilities, from *JWST* in space, to efficient multi-plexing on 5- to 10-meter class and high spatial and spectral resolution studies enabled on 30-meter class ground-based facilities. Moreover, continued long-term monitoring of variables, as with OGLE (e.g., Soszyński et al, 2008), Cluster AgeS Experiment (e.g., Kaluzny et al, 2005), and the homogeneous photometry series (e.g., Stetson et al, 2014b), provide additional characterization and classification diagnostics for these variables. With the ability to determine ages and star formation histories, clusters and nearby galaxies are ideal to study population-effects, while also being able to cleanly resolve individual stars.

Fourth, these standard candles are reaching to unprecedented precisions and accuracies that enable powerful scientific explorations, from the structure of our Galaxy, our galactic neighborhood, and ultimately to the measurement of fundamental cosmological parameters. By utilizing IR observations, the impact of extinction has been minimized, and, for all of the distance indicators described here, provide smaller intrinsic variations, which in turn make these distance indicators more powerful. While few percent distances are incredible (especially to individual RRL or T2C), it is also a realm where every *source of uncertainty matters*, from differences in the detailed definition of filter sets, to the unintentional inclusion of peculiar variables, to the potential for multiple formation channels, to the deviations from a standard extinction law. Stated differently, *every detail matters*. Moreover, an important consideration is the measure of the intrinsic dispersion in these relationships or for a given class of standard candle as a fundamental limit to their precision. For instance, *how stable is the TRGB magnitude?, how flat is the horizontal branch?, how standard are our standard candles?, and how homogeneous are our samples?* These are fundamental aspects to the measurement of distances, and quantities that can be estimated, but whose measure is nuanced and complex.

The stage for better exploiting the Pop II standard candles is set, in particular with the strong inter-relationship between the theory and observation. With the dominance of IR-focused observational facilities in the future, there is great potential for the RRL, T2Cs, and TRGB, all of which become more precise and more powerful in the IR regime. Coupled with the potential to probe nearly all galactic structures and galaxies of all Hubble types, and nearly all total luminosities, the Pop II standard candles stand to sharpen our view of the Universe.

**Acknowledgements** The authors warmly acknowledge the hospitality of ISSI-BJ for an engaging conference and the conference organizer Richard De Grijs for his leadership in completing these chapters. We further thank the anonymous referees for useful comments and perspectives that have improved and broadened this review. RLB acknowledges many insightful discussions with Barry Madore, Wendy Freedman, and the Carnegie-Chicago program team, as well as helpful conversations and data for figures from Mark Seibert, Erika Carlson, Andrew Monson, Victoria Scowcroft, Julianne Dalcanton, and Ben Williams. Support for this

---

work was provided by NASA through Hubble Fellowship grant #51386.01 awarded to RLB by the Space Telescope Science Institute, which is operated by the Association of Universities for Research in Astronomy, Inc., for NASA, under contract NAS 5-26555. GB thanks A Severo Ochoa research grant at the Instituto de Astrofísica de Canarias, where part of this manuscript was written. VFB warmly thank Prof. R.P. Kudritzski for many useful discussions concerning stellar atmospheres and non-LTE effects in giant stars and Dr. P.B. Stetson for his superb-quality photometric reduction work, which has been a key component of the work presented here. VFB acknowledges PRIN-INAF 2011 "Tracing the formation and evolution of the Galactic halo with VST" (P.I.: M. Marconi), PRIN-MIUR (2010LY5N2T) "Chemical and dynamical evolution of the Milky Way and Local Group galaxies" (P.I.: F. Matteucci). VFB thank the Japan Society for the Promotion of Science for a research grant (L15518) and the support from FIRB 2013 (grant: RBFR13J716). We also thank the Education and Science Ministry of Spain (grants AYA201016717). VFB finally acknowledge the financial support from the PO FSE Abruzzo 2007-2013 through the grant "Spectrophotometric characterization of stellar populations in Local Group dwarf galaxies", prot.89/2014/OACTe/D (PI: S. Cassisi). GF has been supported by the Futuro in Ricerca 2013 (grant RBFR13J716). CEMV and MM acknowledges support from the Spanish Ministry of Economy and Competitiveness (MINECO) under the grant (project reference AYA2014-56795-P) NM is grateful to Grant-in-Aid (KAKENHI No. 26287028) from the Japan Society for the Promotion of Science.

## References

- Adams WS (1916) Investigations in Stellar Spectroscopy. III. Application of a Spectroscopic Method of Determining Stellar Distances to Stars of Measured Parallax. *Proceedings of the National Academy of Science* 2:152–157, DOI 10.1073/pnas.2.3.152
- Adams WS, Kohlschütter A (1914) Some spectral criteria for the determination of absolute stellar magnitudes. *ApJ*40, DOI 10.1086/142132
- Alcock C, Allsman RA, Alves DR, Axelrod TS, Becker A, Bennett DP, Cook KH, Freeman KC, Griest K, Lawson WA, Lehner MJ, Marshall SL, Minniti D, Peterson BA, Pollard KR, Pratt MR, Quinn PJ, Rodgers AW, Sutherland W, Tomaney A, Welch DL (1998) The MACHO Project LMC Variable Star Inventory. VII. The Discovery of RV Tauri Stars and New Type II Cepheids in the Large Magellanic Cloud. *AJ*115:1921–1933, DOI 10.1086/300317, astro-ph/9708039
- Andrievsky S, Wallerstein G, Korotin S, Lyashko D, Kovtyukh V, Tsymbal V, Davis CE, Gomez T, Huang W, Farrell EM (2018) The Relationship of Sodium and Oxygen in Galactic Field RR Lyrae Stars. *PASP*130(2):024201, DOI 10.1088/1538-3873/aa9783
- Antonello E, Fossati L, Fugazza D, Mantegazza L, Gieren W (2006) Variable stars in nearby galaxies. VII. P-L relation in the BVRI bands of Cepheids in IC 1613. *A&A*445:901–906, DOI 10.1051/0004-6361:20053822
- Arp HC (1955) Color-magnitude diagrams for seven globular clusters. *AJ*60:317, DOI 10.1086/107232
- Baade W (1926) Über eine Möglichkeit, die Pulsationstheorie der  $\delta$  Cephei-Veränderlichen zu prüfen. *Astronomische Nachrichten* 228:359, DOI 10.1002/asna.19262282003
- Baade W (1944) The Resolution of Messier 32, NGC 205, and the Central Region of the Andromeda Nebula. *ApJ*100:137, DOI 10.1086/144650
- Baade W (1956) The Period-Luminosity Relation of the Cepheids. *PASP*68:5, DOI 10.1086/126870
- Baade W (1958a) Galaxies and their Stellar Populations. (A Review of the Present State of Affairs). *Ricerche Astronomiche* 5:3
- Baade W (1958b) Physical Variable Stars and Stellar Populations. *Ricerche Astronomiche* 5:165
- Baade W (1958c) The Population of the Galactic Nucleus and the Evidence for the Presence of an Old Population Pervading the Whole Disk of our Galaxy. *Ricerche Astronomiche* 5:303
- Baade W, Swope HH (1955) The Palomar survey of variables in M 31 (First results). *AJ*60:151–152, DOI 10.1086/107146
- Baade W, Swope HH (1961) The Draco system, a dwarf galaxy. *AJ*66:300–347, DOI 10.1086/108431
- Bailer-Jones CAL (2015) Estimating Distances from Parallaxes. *PASP*127:994, DOI 10.1086/683116, 1507.02105
- Bailey SI (1902) A discussion of variable stars in the cluster  $\omega$  Centauri. *Annals of Harvard College Observatory* 38
- Bailey SI, Leland EF, Woods IE, Pickering EC (1919) Variable stars in the cluster Messier 15. *Annals of Harvard College Observatory* 78:195–250
- Baker N, Kippenhahn R (1965) The Pulsations of Models of Delta Cephei Stars.

- II. ApJ142:868, DOI 10.1086/148359
- Barker MK, Sarajedini A, Harris J (2004) Variations in Star Formation History and the Red Giant Branch Tip. ApJ606:869–893, DOI 10.1086/383026, astro-ph/0401387
- Battaglia G, Irwin M, Tolstoy E, Hill V, Helmi A, Letarte B, Jablonka P (2008) Analysis and calibration of CaII triplet spectroscopy of red giant branch stars from VLT/FLAMES observations. MNRAS383:183–199, DOI 10.1111/j.1365-2966.2007.12532.x, 0710.0798
- Beaton RL, Freedman WL, Madore BF, Bono G, Carlson EK, Clementini G, Durbin MJ, Garofalo A, Hatt D, Jang IS, Kollmeier JA, Lee MG, Monson AJ, Rich JA, Scowcroft V, Seibert M, Sturch L, Yang SC (2016) The Carnegie-Chicago Hubble Program. I. An Independent Approach to the Extragalactic Distance Scale Using Only Population II Distance Indicators. ApJ832:210, DOI 10.3847/0004-637X/832/2/210, 1604.01788
- Bellazzini M (2008) The Tip of the Red Giant Branch. Mem. Soc. Astron. Italiana79:440, 0711.2016
- Bellazzini M, Ferraro FR, Pancino E (2001) A Step toward the Calibration of the Red Giant Branch Tip as a Standard Candle. ApJ556:635–640, DOI 10.1086/321613, astro-ph/0104114
- Bellazzini M, Ferraro FR, Sollima A, Pancino E, Origlia L (2004) The calibration of the RGB Tip as a Standard Candle. Extension to Near Infrared colors and higher metallicity. A&A424:199–211, DOI 10.1051/0004-6361:20035910, astro-ph/0404572
- Benedict GF, McArthur BE, Feast MW, Barnes TG, Harrison TE, Bean JL, Menzies JW, Chaboyer B, Fossati L, Nesvacil N, Smith HA, Kolenberg K, Laney CD, Kochukhov O, Nelan EP, Shulyak DV, Taylor D, Freedman WL (2011) Distance Scale Zero Points from Galactic RR Lyrae Star Parallaxes. AJ142:187, DOI 10.1088/0004-6256/142/6/187, 1109.5631
- Benedict GF, McArthur BE, Nelan EP, Harrison TE (2017) Astrometry with Hubble Space Telescope Fine Guidance Sensors—A Review. PASP129(1):012001, DOI 10.1088/1538-3873/129/971/012001, 1610.05176
- Benedict GF, McArthur BE, Harrison TE (2018) An Assessment of Gaia DR2 Parallaxes. Research Notes of the American Astronomical Society 2(2):22, URL <http://stacks.iop.org/2515-5172/2/i=2/a=22>
- Bernard EJ, Monelli M, Gallart C, Aparicio A, Cassisi S, Drozdovsky I, Hidalgo SL, Skillman ED, Stetson PB (2010a) The ACS LCID Project. II. Faint Variable Stars in the Isolated Dwarf Irregular Galaxy IC 1613. ApJ712:1259–1276, DOI 10.1088/0004-637X/712/2/1259, 1002.4178
- Bernard EJ, Monelli M, Gallart C, Aparicio A, Cassisi S, Drozdovsky I, Hidalgo SL, Skillman ED, Stetson PB (2010b) The ACS LCID Project. II. Faint Variable Stars in the Isolated Dwarf Irregular Galaxy IC 1613. ApJ712:1259–1276, DOI 10.1088/0004-637X/712/2/1259, 1002.4178
- Bersier D, Wood PR (2002) Variable Stars in the Fornax Dwarf Galaxy. AJ123:840–847, DOI 10.1086/338315, astro-ph/0110555
- Bessel FW (1838) On the parallax of 61 Cygni. MNRAS4:152–161, DOI 10.1093/mnras/4.17.152
- Bessel F (1871) Die beweis für die bewegung der erde.
- Bhardwaj A, Macri LM, Rejkuba M, Kanbur SM, Ngeow CC, Singh HP (2017a) Large Magellanic Cloud Near-infrared Synoptic Survey. IV. Leavitt Laws for

- Type II Cepheid Variables. *AJ*153:154, DOI 10.3847/1538-3881/aa5e4f, 1702.00967
- Bhardwaj A, Rejkuba M, Minniti D, Surot F, Valenti E, Zoccali M, Gonzalez OA, Romaniello M, Kanbur SM, Singh HP (2017b) Galactic bulge population II Cepheids in the VVV survey: period-luminosity relations and a distance to the Galactic centre. *A&A*605:A100, DOI 10.1051/0004-6361/201730841, 1707.03755
- Blažko S (1907) Mitteilung über veränderliche Sterne. *Astronomische Nachrichten* 175:325, DOI 10.1002/asna.19071752002
- Bonanos AZ (2013) Eclipsing binary distances to the edge of the Local Group. In: de Grijs R (ed) *Advancing the Physics of Cosmic Distances*, IAU Symposium, vol 289, pp 173–178, DOI 10.1017/S1743921312021321
- Bonanos AZ, Stanek KZ, Kudritzki RP, Macri LM, Sasselov DD, Kaluzny J, Stetson PB, Bersier D, Bresolin F, Matheson T, Mochejska BJ, Przybilla N, Szentgyorgyi AH, Tonry J, Torres G (2006) The First DIRECT Distance Determination to a Detached Eclipsing Binary in M33. *ApJ*652:313–322, DOI 10.1086/508140, astro-ph/0606279
- Bono G (2003) RR Lyrae Distance Scale: Theory and Observations. In: Alloin D, Gieren W (eds) *Stellar Candles for the Extragalactic Distance Scale*, Lecture Notes in Physics, Berlin Springer Verlag, vol 635, pp 85–104, DOI 10.1007/978-3-540-39882-0\_5, astro-ph/0305102
- Bono G, Marconi M (1999) On the Period-Luminosity-Color Relation of Classical Cepheids. In: Chu YH, Suntzeff N, Hesser J, Bohlender D (eds) *New Views of the Magellanic Clouds*, IAU Symposium, vol 190, p 527, astro-ph/9810460
- Bono G, Stellingwerf RF (1994) Pulsation and stability of RR Lyrae stars. I: Instability strip. *ApJS*93:233–269, DOI 10.1086/192054
- Bono G, Caputo F, Stellingwerf RF (1994) Oosterhoff dichotomy in the Galaxy and globular clusters in the Large Magellanic Cloud. *ApJ*423:294–304, DOI 10.1086/173806
- Bono G, Castellani V, degl’Innocenti S, Pulone L (1995) Advanced evolutionary phases of low-mass stars: The role of the original helium. *A&A*297:115–126
- Bono G, Incerpi R, Marconi M (1996) Metallicity Effects on RR Lyrae Variables. *ApJ*467:L97, DOI 10.1086/310207, astro-ph/9605143
- Bono G, Caputo F, Cassisi S, Castellani V, Marconi M (1997a) Metal-rich RR Lyrae Variables. I. The Evolutionary Scenario. *ApJ*479:279–289, DOI 10.1086/303872, astro-ph/9609153
- Bono G, Caputo F, Castellani V, Marconi M (1997b) Nonlinear investigation of the pulsational properties of RR Lyrae variables. *A&AS*121:327–342, DOI 10.1051/aas:1997289, astro-ph/9606030
- Bono G, Caputo F, Santolamazza P (1997c) Evolutionary scenario for metal-poor pulsating stars. I. Type II Cepheids. *A&A*317:171–177
- Bono G, Marconi M, Stellingwerf RF (1999) Classical Cepheid Pulsation Models. I. Physical Structure. *ApJS*122:167–205, DOI 10.1086/313207
- Bono G, Caputo F, Castellani V, Marconi M, Storm J (2001) Theoretical insights into the RR Lyrae K-band period-luminosity relation. *MNRAS*326:1183–1190, DOI 10.1046/j.1365-8711.2001.04655.x, astro-ph/0105481
- Bono G, Caputo F, Castellani V, Marconi M, Storm J, Degl’Innocenti S (2003) A pulsational approach to near-infrared and visual magnitudes of RR Lyr stars. *MNRAS*344:1097–1106, DOI 10.1046/j.1365-8711.2003.06878.x, astro-ph/0306142

- Bono G, Caputo F, Di Criscienzo M (2007) RR Lyrae stars in Galactic globular clusters. VI. The period-amplitude relation. *A&A*476:779–790, DOI 10.1051/0004-6361:20078206, 0709.3177
- Bono G, Dall’Ora M, Caputo F, Coppola G, Genovali K, Marconi M, Piersimoni AM, Stellingwerf RF (2011) RR Lyrae the Stellar Beacons of the Galactic Structure. In: McWilliam A (ed) RR Lyrae Stars, Metal-Poor Stars, and the Galaxy, vol 5, p 1, 1108.5372
- Bono G, Pietrinferni A, Marconi M, Braga VF, Fiorentino G, Stetson PB, Buonanno R, Castellani M, Dall’Ora M, Fabrizio M, Ferraro I, Giuffrida G, Iannicola G, Marengo M, Magurno D, Martinez-Vazquez CE, Matsunaga N, Monelli M, Neeley J, Rastello S, Salaris M, Short L, Stellingwerf RF (2016) On the pulsation and evolutionary properties of helium burning radially pulsating variables. *Communications of the Konkoly Observatory Hungary* 105:149–159
- Bono G, Braga VF, Ferraro I, Fiorentino G, Gilmozzi R, Iannicola G, Magurno D, Matsunaga N, Monelli M, Rastello S (2017) Massive stellar systems: observational challenges and perspectives in the E-ELT era. In: Charbonnel C, Nota A (eds) Formation, Evolution, and Survival of Massive Star Clusters, IAU Symposium, vol 316, pp 36–43, DOI 10.1017/S1743921315010856
- Borucki WJ, Koch D, Basri G, Batalha N, Brown T, Caldwell D, Caldwell J, Christensen-Dalsgaard J, Cochran WD, DeVore E, Dunham EW, Dupree AK, Gautier TN, Geary JC, Gilliland R, Gould A, Howell SB, Jenkins JM, Kondo Y, Latham DW, Marcy GW, Meibom S, Kjeldsen H, Lissauer JJ, Monet DG, Morrison D, Sasselov D, Tarter J, Boss A, Brownlee D, Owen T, Buzasi D, Charbonneau D, Doyle L, Fortney J, Ford EB, Holman MJ, Seager S, Steffen JH, Welsh WF, Rowe J, Anderson H, Buchhave L, Ciardi D, Walkowicz L, Sherry W, Horch E, Isaacson H, Everett ME, Fischer D, Torres G, Johnson JA, Endl M, MacQueen P, Bryson ST, Dotson J, Haas M, Kolodziejczak J, Van Cleve J, Chandrasekaran H, Twicken JD, Quintana EV, Clarke BD, Allen C, Li J, Wu H, Tenenbaum P, Verner E, Bruhweiler F, Barnes J, Prsa A (2010) Kepler Planet-Detection Mission: Introduction and First Results. *Science* 327:977, DOI 10.1126/science.1185402
- Boyer ML, McQuinn KBW, Barmby P, Bonanos AZ, Gehrz RD, Gordon KD, Groenewegen MAT, Lagadec E, Lennon D, Marengo M, McDonald I, Meixner M, Skillman E, Sloan GC, Sonneborn G, van Loon JT, Zijlstra A (2015a) An Infrared Census of DUST in Nearby Galaxies with Spitzer (DUSTiNGS). II. Discovery of Metal-poor Dusty AGB Stars. *ApJ*800:51, DOI 10.1088/0004-637X/800/1/51, 1412.0695
- Boyer ML, McQuinn KBW, Barmby P, Bonanos AZ, Gehrz RD, Gordon KD, Groenewegen MAT, Lagadec E, Lennon D, Marengo M, Meixner M, Skillman E, Sloan GC, Sonneborn G, van Loon JT, Zijlstra A (2015b) An Infrared Census of Dust in nearby Galaxies with Spitzer (DUSTiNGS). I. Overview. *ApJS*216:10, DOI 10.1088/0067-0049/216/1/10, 1411.4053
- Braga VF, Dall’Ora M, Bono G, Stetson PB, Ferraro I, Iannicola G, Marengo M, Neeley J, Persson SE, Buonanno R, Coppola G, Freedman W, Madore BF, Marconi ea (2015) On the Distance of the Globular Cluster M4 (NGC 6121) Using RR Lyrae Stars. I. Optical and Near-infrared Period-Luminosity and Period-Wesenheit Relations. *ApJ*799:165, DOI 10.1088/0004-637X/799/2/165, 1411.6826
- Braga VF, Stetson PB, Bono G, Dall’Ora M, Ferraro I, Fiorentino G, Freyhammer

- LM, Iannicola G, Marengo M, Neeley J, Valenti E, Buonanno R, Calamida A, Castellani M, da Silva R, Degl'Innocenti S, Di Cecco A, Fabrizio M, Freedman WL, Giuffrida G, Lub J, Madore BF, Marconi M, Marinoni S, Matsunaga N, Monelli M, Persson SE, Piersimoni AM, Pietrinferni A, Prada-Moroni P, Pulone L, Stellingwerf R, Tognelli E, Walker AR (2016) On the RR Lyrae Stars in Globulars. IV. omega Centauri Optical UBVR Photometry. *AJ*152:170, DOI 10.3847/0004-6256/152/6/170, 1609.04916
- Braga VF, Stetson PB, Bono G, Dall'Orta M, Ferraro I, Fiorentino G, Iannicola G, Marconi M, Marengo M, Monson AJ, Neeley J, Persson SE, Beaton RL, Buonanno R, Calamida A, Castellani M, Di Carlo E, Fabrizio M, Freedman WL, Inno L, Madore BF, Magurno D, Marchetti E, Marinoni S, Marrese P, Matsunaga N, Minniti D, Monelli M, Nonino M, Piersimoni AM, Pietrinferni A, Prada-Moroni P, Pulone L, Stellingwerf R, Tognelli E, Walker AR, Valenti E, Zoccali M (2018) On the RR Lyrae Stars in Globulars. V. The Complete Near-infrared (JHKs) Census of omega Centauri RR Lyrae Variables. *AJ*155:137, DOI 10.3847/1538-3881/aaadab, 1802.03578
- Breitfelder J, Kervella P, Mérand A, Gallenne A, Szabados L, Anderson RI, Willson M, Le Bouquin JB (2015) Observational calibration of the projection factor of Cepheids. I. The type II Cepheid  $\kappa$  Pavonis. *A&A*576:A64, DOI 10.1051/0004-6361/201425171, 1503.05176
- Breitfelder J, Mérand A, Kervella P, Gallenne A, Szabados L, Anderson RI, Le Bouquin JB (2016) Observational calibration of the projection factor of Cepheids. II. Application to nine Cepheids with HST/FGS parallax measurements. *A&A*587:A117, DOI 10.1051/0004-6361/201527030, 1601.04727
- Brown TM, Casertano S, Strader J, Riess A, VandenBerg DA, Soderblom DR, Kalirai J, Salinas R (2018) A High-precision Trigonometric Parallax to an Ancient Metal-poor Globular Cluster. *ApJ*856:L6, DOI 10.3847/2041-8213/aab55a, 1803.02927
- Burki G, Meylan G (1986) Rr-Lyrae Delta-Scuti Sx-Phoenicis Stars and Baade-Wesselink Method - Part Four - Physical Parameters and Distances of Bs-Aquarii and Dy-Pegasi and the Period / Radius Relations for Pulsating Stars. *A&A*159:261
- Cacciari C, Clementini G, Fernley JA (1992) On the absolute magnitude of RR Lyrae stars - UU Ceti, RV Phoenicis, and W Tucanae. *ApJ*396:219–237, DOI 10.1086/171711
- Caputo F (1997) The period-magnitude diagram of RR Lyrae stars - I. The controversy about the distance scale. *MNRAS*284:994–1000, DOI 10.1093/mnras/284.4.994
- Caputo F, Castellani V, Marconi M, Ripepi V (2000) Pulsational  $M_V$  versus [Fe/H] relation(s) for globular cluster RR Lyrae variables. *MNRAS*316:819–826, DOI 10.1046/j.1365-8711.2000.03591.x, astro-ph/0003473
- Cardelli JA, Clayton GC, Mathis JS (1989) The relationship between infrared, optical, and ultraviolet extinction. *ApJ*345:245–256, DOI 10.1086/167900
- Carney BW, Storm J, Jones RV (1992) The Baade-Wesselink method and the distances to RR Lyrae Stars. VIII - Comparisons with other techniques and implications for globular cluster distances and ages. *ApJ*386:663–684, DOI 10.1086/171047
- Carretta E, Gratton RG (1997) Abundances for globular cluster giants. I. Homogeneous metallicities for 24 clusters. *A&AS*121:95–112, DOI 10.1051/aas:1997116,

- [astro-ph/9607078](#)
- Cassisi S, Salaris M (2013) Old Stellar Populations: How to Study the Fossil Record of Galaxy Formation
- Cassisi S, Castellani M, Caputo F, Castellani V (2004) RR Lyrae variables in Galactic globular clusters. IV. Synthetic HB and RR Lyrae predictions. *A&A*426:641–650, DOI 10.1051/0004-6361:20041048, [astro-ph/0407256](#)
- Cassisi S, Potekhin AY, Pietrinferni A, Catelan M, Salaris M (2007) Updated Electron-Conduction Opacities: The Impact on Low-Mass Stellar Models. *ApJ*661:1094–1104, DOI 10.1086/516819, [astro-ph/0703011](#)
- Catelan M (2009) Horizontal branch stars: the interplay between observations and theory, and insights into the formation of the Galaxy. *Ap&SS*320:261–309, DOI 10.1007/s10509-009-9987-8, [astro-ph/0507464](#)
- Catelan M, Smith HA (2015) Pulsating Stars
- Catelan M, Pritzl BJ, Smith HA (2004) The RR Lyrae Period-Luminosity Relation. I. Theoretical Calibration. *ApJS*154:633–649, DOI 10.1086/422916, [astro-ph/0406067](#)
- Chadid M, Vernin J, Preston G, Zalian C, Pouzenc C, Abe L, Agabi A, Aristidi E, Liu LY, Mékarnia D, Tringet H (2014) First Detection of Multi-shocks in RR Lyrae Stars from Antarctica: A Possible Explanation of the Blazhko Effect. *AJ*148:88, DOI 10.1088/0004-6256/148/5/88
- Chen HY, Holz DE, Miller J, Evans M, Vitale S, Creighton J (2017) Distance measures in gravitational-wave astrophysics and cosmology. *ArXiv e-prints* 1709.08079
- Christy RF (1966) A Study of Pulsation in RR Lyrae Models. *ApJ*144:108, DOI 10.1086/148593
- Ciechanowska A, Pietrzyński G, Szcwycyk O, Gieren W, Soszyński I (2010) The Araucaria Project: The Distance to the Small Magellanic Cloud from Near Infrared Photometry of Type II Cepheids. *Acta Astron.*60:233–243, 1007.4217
- Cioni MRL, van der Marel RP, Loup C, Habing HJ (2000) The tip of the red giant branch and distance of the Magellanic Clouds: results from the DENIS survey. *A&A*359:601–614, [astro-ph/0003223](#)
- Clement CM, Muzzin A, Dufton Q, Ponnampalam T, Wang J, Burford J, Richardson A, Rosebery T, Rowe J, Hogg HS (2001a) Variable Stars in Galactic Globular Clusters. *AJ*122:2587–2599, DOI 10.1086/323719, [astro-ph/0108024](#)
- Clement CM, Muzzin A, Dufton Q, Ponnampalam T, Wang J, Burford J, Richardson A, Rosebery T, Rowe J, Hogg HS (2001b) Variable Stars in Galactic Globular Clusters. *AJ*122:2587–2599, DOI 10.1086/323719, [astro-ph/0108024](#)
- Clementini G, Carretta E, Gratton R, Merighi R, Mould JR, McCarthy JK (1995) The Composition of HB Stars: RR Lyrae Variables. *AJ*110:2319, DOI 10.1086/117692, [astro-ph/9507056](#)
- Clementini G, Gratton R, Bragaglia A, Carretta E, Di Fabrizio L, Maio M (2003) Distance to the Large Magellanic Cloud: The RR Lyrae Stars. *AJ*125:1309–1329, DOI 10.1086/367773
- Clementini G, Ripepi V, Bragaglia A, Martinez Fiorenzano AF, Held EV, Gratton RG (2005) The metal abundance distribution of the oldest stellar component in the Sculptor dwarf spheroidal galaxy\*. *MNRAS*363:734–748, DOI 10.1111/j.1365-2966.2005.09478.x, [astro-ph/0506206](#)
- Conn AR, Lewis GF, Ibata RA, Parker QA, Zucker DB, McConnachie AW, Martin NF, Irwin MJ, Tanvir N, Fardal MA, Ferguson AMN (2011) A Bayesian



- Approach to Locating the Red Giant Branch Tip Magnitude. I. *ApJ*740:69, DOI 10.1088/0004-637X/740/2/69, 1107.3206
- Coppola G, Dall’Ora M, Ripepi V, Marconi M, Musella I, Bono G, Piersimoni AM, Stetson PB, Storm J (2011) Distance to Galactic globulars using the near-infrared magnitudes of RR Lyrae stars - IV. The case of M5 (NGC 5904). *MNRAS*416:1056–1066, DOI 10.1111/j.1365-2966.2011.19102.x, 1105.4031
- Coppola G, Marconi M, Stetson PB, Bono G, Braga VF, Ripepi V, Dall’Ora M, Musella I, Buonanno R, Fabrizio M, Ferraro I, Fiorentino G, Iannicola G, Monelli M, Nonino M, Thévenin F, Walker AR (2015) The Carina Project IX: On Hydrogen and Helium Burning Variables. *ApJ*814:71, DOI 10.1088/0004-637X/814/1/71, 1509.02687
- Cox JP (1958) Non-Adiabatic Stellar Pulsation. I. *ApJ*127:194, DOI 10.1086/146451
- Cox JP (1963) On Second Helium Ionization as a Cause of Pulsational Instability in Stars. *ApJ*138:487, DOI 10.1086/147661
- Czerny B, Beaton R, Bejger M, Cackett E, Dall’Ora M, Holanda RFL, Jensen JB, Jha SW, Lusso E, Minezaki T, Risaliti G, Salaris M, Toonen S, Yoshii Y (2018) Astronomical Distance Determination in the Space Age. Secondary Distance Indicators. *Space Sci. Rev.*214:32, DOI 10.1007/s11214-018-0466-9, 1801.00598
- Da Costa GS (1984) The age(s?) of the sculptor dwarf galaxy. *ApJ*285:483–494, DOI 10.1086/162523
- Da Costa GS, Armandroff TE (1990) Standard globular cluster giant branches in the ( $M_{I,V-I_{sub}O}$ ) plane. *AJ*100:162–181, DOI 10.1086/115500
- Dalcanton JJ, Williams BF, Melbourne JL, Girardi L, Dolphin A, Rosenfield PA, Boyer ML, de Jong RS, Gilbert K, Marigo P, Olsen K, Seth AC, Skillman E (2012) Resolved Near-infrared Stellar Populations in Nearby Galaxies. *ApJS*198:6, DOI 10.1088/0067-0049/198/1/6, 1109.6893
- Dall’Ora M, Storm J, Bono G, Ripepi V, Monelli M, Testa V, Andreuzzi G, Buonanno R, Caputo F, Castellani V, Corsi CE, Marconi G, Marconi M, Pulone L, Stetson PB (2004) The Distance to the Large Magellanic Cloud Cluster Reticulum from the K-Band Period-Luminosity-Metallicity Relation of RR Lyrae Stars. *ApJ*610:269–274, DOI 10.1086/421513, astro-ph/0404098
- Dambis AK, Berdnikov LN, Kniazev AY, Kravtsov VV, Rastorguev AS, Sefako R, Vozyakova OV (2013) RR Lyrae variables: visual and infrared luminosities, intrinsic colours and kinematics. *MNRAS*435:3206–3220, DOI 10.1093/mnras/stt1514, 1308.4727
- Dambis AK, Rastorguev AS, Zabolotskikh MV (2014) Mid-infrared period-luminosity relations for globular cluster RR Lyrae. *MNRAS*439:3765–3774, DOI 10.1093/mnras/stu226, 1401.5523
- de Boer TJJ, Tolstoy E, Hill V, Saha A, Olsen K, Starkenburg E, Lemasle B, Irwin MJ, Battaglia G (2012) The star formation and chemical evolution history of the sculptor dwarf spheroidal galaxy. *A&A*539:A103, DOI 10.1051/0004-6361/201118378, 1201.2408
- de Bruijne JHJ, Rygl KLJ, Antoja T (2014) Gaia Astrometric Science Performance - Post-Launch Predictions. In: *EAS Publications Series, EAS Publications Series*, vol 67, pp 23–29, DOI 10.1051/eas/1567004, 1502.00791
- de Grijs R, Bono G (2014) Clustering of Local Group Distances: Publication Bias or Correlated Measurements? II. M31 and Beyond. *AJ*148:17, DOI 10.1088/0004-6256/148/1/17, 1405.2124

- de Grijs R, Bono G (2015) Clustering of Local Group Distances: Publication Bias or Correlated Measurements? III. The Small Magellanic Cloud. *AJ*149:179, DOI 10.1088/0004-6256/149/6/179, 1504.00417
- de Grijs R, Wicker JE, Bono G (2014) Clustering of Local Group Distances: Publication Bias or Correlated Measurements? I. The Large Magellanic Cloud. *AJ*147:122, DOI 10.1088/0004-6256/147/5/122, 1403.3141
- de Grijs R, Courbin F, Martínez-Vázquez CE, Monelli M, Oguri M, Suyu SH (2017) Toward an Internally Consistent Astronomical Distance Scale. *Space Sci. Rev.*212:1743–1785, DOI 10.1007/s11214-017-0395-z, 1706.07933
- Deep A, Fiorentino G, Tolstoy E, Diolaiti E, Bellazzini M, Ciliegi P, Davies RI, Conan JM (2011) An E-ELT case study: colour-magnitude diagrams of an old galaxy in the Virgo cluster. *A&A*531:A151, DOI 10.1051/0004-6361/201116603, 1105.3455
- Del Principe M, Piersimoni AM, Bono G, Di Paola A, Dolci M, Marconi M (2005) Near-Infrared Observations of RR Lyrae Variables in Galactic Globular Clusters. I. The Case of M92. *AJ*129:2714–2724, DOI 10.1086/430148, astro-ph/0503140
- Del Principe M, Piersimoni AM, Storm J, Caputo F, Bono G, Stetson PB, Castellani M, Buonanno R, Calamida A, Corsi CE, Dall’Ora M, Ferraro I, Freyhammer LM, Iannicola G, Monelli M, Nonino M, Pulone L, Ripepi V (2006) A Pulsational Distance to  $\omega$  Centauri Based on Near-Infrared Period-Luminosity Relations of RR Lyrae Stars. *ApJ*652:362–369, DOI 10.1086/508136, astro-ph/0608052
- Deupree RG (1977a) The theoretical red edge of the RR Lyrae gap. I - Dependence of convection on pulsation phase. *ApJ*211:509–526, DOI 10.1086/154958
- Deupree RG (1977b) The theoretical red edge of the RR Lyrae gap. IV - Convective steady-state models. *ApJ*215:620–623, DOI 10.1086/155396
- di Benedetto GP (1998) Towards a fundamental calibration of stellar parameters of A, F, G, K dwarfs and giants. *A&A*339:858–871
- Di Criscienzo M, Marconi M, Caputo F (2004) RR Lyrae Stars in Galactic Globular Clusters. III. Pulsational Predictions for Metal Content  $Z=0.0001$  to  $Z=0.006$ . *ApJ*612:1092–1106, DOI 10.1086/422742, astro-ph/0405415
- Di Criscienzo M, Caputo F, Marconi M, Cassisi S (2007) Synthetic properties of bright metal-poor variables. II. BL Hercules stars. *A&A*471:893–900, DOI 10.1051/0004-6361:20066541, 0705.2679
- Diethelm R (1990) Physical parameters of pulsating variables with periods between one and three days. II - Fundamental parameters. *A&A*239:186–192
- Diethelm R (1996) Period changes of AHB1 variables. *A&A*307:803–806
- Dolphin AE (2000) WFPC2 Stellar Photometry with HSTPHOT. *PASP*112:1383–1396, DOI 10.1086/316630, astro-ph/0006217
- Dolphin AE, Saha A, Skillman ED, Tolstoy E, Cole AA, Dohm-Palmer RC, Gallagher JS, Mateo M, Hoessel JG (2001) Deep Hubble Space Telescope Imaging of IC 1613. I. Variable Stars and Distance. *ApJ*550:554–569, DOI 10.1086/319809, astro-ph/0012150
- Drimmel R, Cabrera-Lavers A, López-Corredoira M (2003) A three-dimensional Galactic extinction model. *A&A*409:205–215, DOI 10.1051/0004-6361:20031070, astro-ph/0307273
- Duncombe RL, Jefferys WH, Shelus PJ, Hemenway PD, Benedict GF (1991) Astrometry using the Hubble Space Telescope fine guidance sensors. *Advances in Space Research* 11:87–96, DOI 10.1016/0273-1177(91)90475-Y
- Eddington AS (1918) Stars, Gaseous, On the pulsations of a gaseous star.

MNRAS79:2–22

- Eddington AS (1926) Theories of Cepheid variation. *The Observatory* 49:88–88
- ESA (ed) (1997) The HIPPARCOS and TYCHO catalogues. Astrometric and photometric star catalogues derived from the ESA HIPPARCOS Space Astrometry Mission, ESA Special Publication, vol 1200
- Fadeev IA, Fokin AB (1985) Hydrodynamic models for population-II cepheids. *Ap&SS*111:355–374, DOI 10.1007/BF00649975
- Feast M (2011) RR Lyraes and Type II Cepheids in the Magellanic Clouds: Distance Scales and Population Gradients. In: McWilliam A (ed) *RR Lyrae Stars, Metal-Poor Stars, and the Galaxy*, vol 5, p 170, 1106.1449
- Feast MW (1998) Distance Scales After HIPPARCOS. *Ap&SS*263:209–214, DOI 10.1023/A:1002110327632
- Feast MW (2010) The Luminosities of Type II Cepheids and RR Lyrae Variables. In: Sterken C, Samus N, Szabados L (eds) *Variable Stars, the Galactic halo and Galaxy Formation*, 0912.4159
- Feast MW (2013) Galactic Distance Scales, p 829. DOI 10.1007/978-94-007-5612-0\_16
- Feast MW, Laney CD, Kinman TD, van Leeuwen F, Whitelock PA (2008) The luminosities and distance scales of type II Cepheid and RR Lyrae variables. *MNRAS*386:2115–2134, DOI 10.1111/j.1365-2966.2008.13181.x, 0803.0466
- Fernie JD (1969) The Period-Luminosity Relation: A Historical Review. *PASP*81:707, DOI 10.1086/128847
- Fernley J, Barnes TG, Skillen I, Hawley SL, Hanley CJ, Evans DW, Solano E, Garrido R (1998) The absolute magnitudes of RR Lyraes from HIPPARCOS parallaxes and proper motions. *A&A*330:515–520
- Ferrarese L, Mould JR, Kennicutt RC Jr, Huchra J, Ford HC, Freedman WL, Stetson PB, Madore BF, Sakai S, Gibson BK, Graham JA, Hughes SM, Illingworth GD, Kelson DD, Macri L, Sebo K, Silbermann NA (2000) The Hubble Space Telescope Key Project on the Extragalactic Distance Scale. XXVI. The Calibration of Population II Secondary Distance Indicators and the Value of the Hubble Constant. *ApJ*529:745–767, DOI 10.1086/308309, astro-ph/9908192
- Feuchtinger MU, Dorfi EA, Hofner S (1993) Radiation hydrodynamics in atmospheres of long-period variables. *A&A*273:513
- Fiorentino G, Monelli M (2012) Anomalous Cepheids in the Large Magellanic Cloud. Insight into their origin and connection with the star formation history. *A&A*540:A102, DOI 10.1051/0004-6361/201118621, 1202.2752
- Fiorentino G, Marconi M, Musella I, Caputo F (2007) Classical Cepheid pulsation models. XI. Effects of convection and chemical composition on the period-luminosity and period-Wesenheit relations. *A&A*476:863–879, DOI 10.1051/0004-6361:20077587, 0707.0959
- Fiorentino G, Monachesi A, Trager SC, Lauer TR, Saha A, Mighell KJ, Freedman W, Dressler A, Grillmair C, Tolstoy E (2010) RR Lyrae Variables in M32 and the Disk of M31. *ApJ*708:817–833, DOI 10.1088/0004-637X/708/1/817, 0911.0355
- Fiorentino G, Bono G, Monelli M, Stetson PB, Tolstoy E, Gallart C, Salaris M, Martínez-Vázquez CE, Bernard EJ (2015) Weak Galactic Halo-Dwarf Spheroidal Connection from RR Lyrae Stars. *ApJ*798:L12, DOI 10.1088/2041-8205/798/1/L12, 1411.7300
- Fiorentino G, Monelli M, Stetson PB, Bono G, Gallart C, Martínez-Vázquez CE, Bernard EJ, Massari D, Braga VF, Dall’Ora M (2017) Weak Galactic halo-

- Fornax dSph connection from RR Lyrae stars. *A&A*599:A125, DOI 10.1051/0004-6361/201629501, 1612.02991
- For BQ, Preston GW, Sneden C (2011a) Radial Velocities and Pulsation Ephemerides of 11 Field RR Lyrae Stars. *ApJS*194:38, DOI 10.1088/0067-0049/194/2/38, 1104.2668
- For BQ, Sneden C, Preston GW (2011b) The Chemical Compositions of Variable Field Horizontal-branch Stars: RR Lyrae Stars. *ApJS*197:29, DOI 10.1088/0067-0049/197/2/29, 1110.0548
- Freedman WL (1988) Stellar content of nearby galaxies. I - BVRI CCD photometry for IC 1613. *AJ*96:1248–1306, DOI 10.1086/114878
- Freedman WL, Madore BF (2010) The Hubble Constant. *ARA&A*48:673–710, DOI 10.1146/annurev-astro-082708-101829, 1004.1856
- Freedman WL, Madore BF, Gibson BK, Ferrarese L, Kelson DD, Sakai S, Mould JR, Kennicutt RC Jr, Ford HC, Graham JA, Huchra JP, Hughes SMG, Illingworth GD, Macri LM, Stetson PB (2001) Final Results from the Hubble Space Telescope Key Project to Measure the Hubble Constant. *ApJ*553:47–72, DOI 10.1086/320638, astro-ph/0012376
- Freedman WL, Rigby J, Madore BF, Persson SE, Sturch L, Mager V (2009) The Cepheid Period-Luminosity Relation (The Leavitt Law) at Mid-Infrared Wavelengths. IV. Cepheids in IC 1613. *ApJ*695:996–998, DOI 10.1088/0004-637X/695/2/996, 0901.2907
- Gaia Collaboration, Prusti T, de Bruijne JHJ, Brown AGA, Vallenari A, Babusi-  
aux C, Bailer-Jones CAL, Bastian U, Biermann M, Evans DW, et al (2016) The Gaia mission. *A&A*595:A1, DOI 10.1051/0004-6361/201629272, 1609.04153
- Geha M, Weisz D, Grocholski A, Dolphin A, van der Marel RP, Guhathakurta P (2015) HST/ACS Direct Ages of the Dwarf Elliptical Galaxies NGC 147 and NGC 185. *ApJ*811:114, DOI 10.1088/0004-637X/811/2/114, 1503.06526
- Gingold RA (1976) The evolutionary status of Population II Cepheids. *ApJ*204:116–130, DOI 10.1086/154156
- Gingold RA (1977) Evolutionary models of metal-rich horizontal branch stars. *MNRAS*178:533–537, DOI 10.1093/mnras/178.4.533
- Giridhar S, Lambert DL, Reddy BE, Gonzalez G, Yong D (2005) Abundance Analyses of Field RV Tauri Stars. VI. An Extended Sample. *ApJ*627:432–445, DOI 10.1086/430265, astro-ph/0503344
- Górski M, Pietrzyński G, Gieren W, Catelan M, Pilecki B, Karczmarek P, Suchomska K, Graczyk D, Konorski P, Zgirski B, Wielgórski P (2016) The Araucaria Project: On the Tip of the Red Giant Branch Distance Determination to the Magellanic Clouds. *AJ*151:167, DOI 10.3847/0004-6256/151/6/167, 1605.06210
- Gould A, Popowski P (1998) Systematics of RR Lyrae Statistical Parallax. III. Apparent Magnitudes and Extinctions. *ApJ*508:844–853, DOI 10.1086/306448, astro-ph/9805176
- Govea J, Gomez T, Preston GW, Sneden C (2014) The Chemical Compositions of RR Lyrae Type C Variable Stars. *ApJ*782:59, DOI 10.1088/0004-637X/782/2/59
- Graczyk D, Konorski P, Pietrzyński G, Gieren W, Storm J, Nardetto N, Gallenne A, Maxted PFL, Kervella P, Kołaczowski Z (2017) The Surface Brightness-color Relations Based on Eclipsing Binary Stars: Toward Precision Better than 1% in Angular Diameter Predictions. *ApJ*837:7, DOI 10.3847/1538-4357/aa5d56, 1611.09976
- Graczyk D, Pietrzyński G, Thompson IB, Gieren W, Pilecki B, Konorski P, Vil-

- lanova S, Górski M, Suchomska K, Karczmarek P, Stepień K, Storm J, Taormina M, Kołaczkowski Z, Wielgórski P, Narloch W, Zgirski B, Gallenne A, Ostrowski J, Smolec R, Udalski A, Soszyński I, Kervella P, Nardetto N, Szymański MK, Wyrzykowski L, Ulaczyk K, Poleski R, Pietrukowicz P, Kozłowski S, Skowron J, Mróz P (2018) The Late-type Eclipsing Binaries in the Large Magellanic Cloud: Catalog of Fundamental Physical Parameters. *ApJ*860:1, DOI 10.3847/1538-4357/aac2bf, 1805.04952
- Green EM, Demarque P, King CR (1987) The revised Yale isochrones and luminosity functions
- Greenhill LJ, Jiang DR, Moran JM, Reid MJ, Lo KY, Claussen MJ (1995) Detection of a Subparsec Diameter Disk in the Nucleus of NGC 4258. *ApJ*440:619, DOI 10.1086/175301
- Grocholski AJ, Cole AA, Sarajedini A, Geisler D, Smith VV (2006) Ca II Triplet Spectroscopy of Large Magellanic Cloud Red Giants. I. Abundances and Velocities for a Sample of Populous Clusters. *AJ*132:1630–1644, DOI 10.1086/507303, astro-ph/0607052
- Groenewegen MAT, Jurkovic MI (2017a) Luminosities and infrared excess in Type II and anomalous Cepheids in the Large and Small Magellanic Clouds. *A&A*603:A70, DOI 10.1051/0004-6361/201730687, 1705.00886
- Groenewegen MAT, Jurkovic MI (2017b) The period-luminosity and period-radius relations of Type II and anomalous Cepheids in the Large and Small Magellanic Clouds. *A&A*604:A29, DOI 10.1051/0004-6361/201730946, 1705.04487
- Groenewegen MAT, Salaris M (1999) The absolute magnitudes of RR Lyrae stars from BT HIPPARCOS parallaxes. *A&A*348:L33–L36, astro-ph/9907207
- Gustafsson B, Edvardsson B, Eriksson K, Jørgensen UG, Nordlund Å, Plez B (2008) A grid of MARCS model atmospheres for late-type stars. I. Methods and general properties. *A&A*486:951–970, DOI 10.1051/0004-6361:200809724, 0805.0554
- Habing HJ, Olofsson H (eds) (2003) Asymptotic giant branch stars
- Hajdu G, Dékány I, Catelan M, Grebel EK, Jurcsik J (2018) A Data-driven Study of RR Lyrae Near-IR Light Curves: Principal Component Analysis, Robust Fits, and Metallicity Estimates. *ApJ*857:55, DOI 10.3847/1538-4357/aab4fd, 1804.01456
- Harris HC (1985) Population II Cepheids. In: Madore BF (ed) *IAU Colloq. 82: Cepheids: Theory and Observation*, pp 232–245
- Hatt D, Beaton RL, Freedman WL, Madore BF, Jang IS, Hoyt TJ, Lee MG, Monson AJ, Rich JA, Scowcroft V, Seibert M (2017) The Carnegie-Chicago Hubble Program. II. The Distance to IC 1613: The Tip of the Red Giant Branch and RR Lyrae Period-luminosity Relations. *ApJ*845:146, DOI 10.3847/1538-4357/aa7f73, 1703.06468
- Hatt D, Freedman WL, Madore BF, Beaton RL, Hoyt TJ, Jang IS, Lee MG, Monson AJ, Rich JA, Scowcroft V, Seibert M (2018) The Carnegie-Chicago Hubble Program. IV. The Distance to NGC 4424, NGC 4526, and NGC 4356 via the Tip of the Red Giant Branch. *ApJ*861:104, DOI 10.3847/1538-4357/aac9cc, 1806.02900
- Hayden MR, Bovy J, Holtzman JA, Nidever DL, Bird JC, Weinberg DH, Andrews BH, Majewski SR, Allende Prieto C, Anders F, Beers TC, Bizyaev D, Chiappini C, Cunha K, Frinchaboy P, García-Herández DA, García Pérez

- AE, Girardi L, Harding P, Hearty FR, Johnson JA, Mészáros S, Minchev I, O’Connell R, Pan K, Robin AC, Schiavon RP, Schneider DP, Schultheis M, Shetrone M, Skrutskie M, Steinmetz M, Smith V, Wilson JC, Zamora O, Zaslowski G (2015) Chemical Cartography with APOGEE: Metallicity Distribution Functions and the Chemical Structure of the Milky Way Disk. *ApJ*808:132, DOI 10.1088/0004-637X/808/2/132, 1503.02110
- Hendel D, Scowcroft V, Johnston KV, Fardal MA, van der Marel RP, Sohn ST, Price-Whelan AM, Beaton RL, Besla G, Bono G, Cioni MRL, Clementini G, Cohen JG, Fabrizio M, Freedman WL, Garofalo A, Grillmair CJ, Kallivayalil N, Kollmeier JA, Law DR, Madore BF, Majewski SR, Marengo M, Monson AJ, Neeley JR, Nidever DL, Pietrzyński G, Seibert M, Sesar B, Smith HA, Soszyński I, Udalski A (2018) SMHASH: anatomy of the Orphan Stream using RR Lyrae stars. *MNRAS*479:570–587, DOI 10.1093/mnras/sty1455, 1711.04663
- Hendricks B, Stetson PB, VandenBerg DA, Dall’Ora M (2012) A New Reddening Law for M4. *AJ*144:25, DOI 10.1088/0004-6256/144/1/25, 1204.5719
- Herrnstein JR, Moran JM, Greenhill LJ, Diamond PJ, Inoue M, Nakai N, Miyoshi M, Henkel C, Riess A (1999) A geometric distance to the galaxy NGC4258 from orbital motions in a nuclear gas disk. *Nature*400:539–541, DOI 10.1038/22972, astro-ph/9907013
- Ho N, Geha M, Tollerud EJ, Zinn R, Guhathakurta P, Vargas LC (2015) Metallicity Evolution of the Six Most Luminous M31 Dwarf Satellites. *ApJ*798:77, DOI 10.1088/0004-637X/798/2/77, 1405.4424
- Houdashelt ML, Bell RA, Sweigart AV (2000) Improved Color-Temperature Relations and Bolometric Corrections for Cool Stars. *AJ*119:1448–1469, DOI 10.1086/301243, astro-ph/9911367
- Howell SB, Sobeck C, Haas M, Still M, Barclay T, Mullally F, Troeltzsch J, Aigrain S, Bryson ST, Caldwell D, Chaplin WJ, Cochran WD, Huber D, Marcy GW, Miglio A, Najita JR, Smith M, Twicken JD, Fortney JJ (2014) The K2 Mission: Characterization and Early Results. *PASP*126:398, DOI 10.1086/676406, 1402.5163
- Hoyt TJ, Freedman WL, Madore BF, Seibert M, Beaton RL, Hatt D, Jang IS, Lee MG, Monson AJ, Rich JA (2018) The Near-infrared Tip of the Red Giant Branch. II. An Absolute Calibration in the Large Magellanic Cloud. *ApJ*858:12, DOI 10.3847/1538-4357/aab7ed, 1803.01277
- Humphreys EML, Argon AL, Greenhill LJ, Moran JM, Reid MJ (2005) Recent Progress on a New Distance to NGC 4258. In: Romney J, Reid M (eds) *Future Directions in High Resolution Astronomy*, Astronomical Society of the Pacific Conference Series, vol 340, p 466
- Humphreys EML, Reid MJ, Greenhill LJ, Moran JM, Argon AL (2008) Toward a New Geometric Distance to the Active Galaxy NGC 4258. II. Centripetal Accelerations and Investigation of Spiral Structure. *ApJ*672:800–816, DOI 10.1086/523637, 0709.0925
- Humphreys EML, Reid MJ, Moran JM, Greenhill LJ, Argon AL (2013) Toward a New Geometric Distance to the Active Galaxy NGC 4258. III. Final Results and the Hubble Constant. *ApJ*775:13, DOI 10.1088/0004-637X/775/1/13, 1307.6031
- Hurley-Keller D, Mateo M, Grebel EK (1999) A New Culprit in the Second-Parameter Problem in the Sculptor Dwarf Spheroidal Galaxy? *ApJ*523:L25–L28, DOI 10.1086/312248, astro-ph/9907156
- Iben I Jr (1971) On the Specification of the Blue Edge of the RR Lyrae Instability

- Strip. *ApJ*166:131, DOI 10.1086/150946
- Inno L, Matsunaga N, Bono G, Caputo F, Buonanno R, Genovali K, Laney CD, Marconi M, Piersimoni AM, Primas F, Romaniello M (2013) On the Distance of the Magellanic Clouds Using Cepheid NIR and Optical-NIR Period-Wesenheit Relations. *ApJ*764:84, DOI 10.1088/0004-637X/764/1/84, 1212.4376
- Inno L, Bono G, Matsunaga N, Fiorentino G, Marconi M, Lemasle B, da Silva R, Soszyński I, Udalski A, Romaniello M, Rix HW (2016) The Panchromatic View of the Magellanic Clouds from Classical Cepheids. I. Distance, Reddening, and Geometry of the Large Magellanic Cloud Disk. *ApJ*832:176, DOI 10.3847/0004-637X/832/2/176, 1609.03554
- Janes KA, Liu T (1992) K-band photometry of globular cluster RR Lyraes and other horizontal branch studies. *Mem. Soc. Astron. Italiana*63:445–450
- Jang IS, Lee MG (2015) The Tip of the Red Giant Branch Distances to Type Ia Supernova Host Galaxies. III. NGC 4038/39 and NGC 5584. *ApJ*807:133, DOI 10.1088/0004-637X/807/2/133, 1506.03089
- Jang IS, Lee MG (2017a) The Tip of the Red Giant Branch Distances to Type Ia Supernova Host Galaxies. V. NGC 3021, NGC 3370, and NGC 1309 and the Value of the Hubble Constant. *ApJ*836:74, DOI 10.3847/1538-4357/836/1/74
- Jang IS, Lee MG (2017b) The Tip of the Red Giant Branch Distances to Type Ia Supernova Host Galaxies. IV. Color Dependence and Zero-point Calibration. *ApJ*835:28, DOI 10.3847/1538-4357/835/1/28, 1611.05040
- Jang IS, Hatt D, Beaton RL, Lee MG, Freedman WL, Madore BF, Hoyt TJ, Monson AJ, Rich JA, Scowcroft V, Seibert M (2018) The Carnegie-Chicago Hubble Program. III. The Distance to NGC 1365 via the Tip of the Red Giant Branch. *ApJ*852:60, DOI 10.3847/1538-4357/aa9d92, 1703.10616
- Jones RV, Carney BW, Fulbright JP (1996) Template K Light Curves for RR Lyrae Stars. *PASP*108:877, DOI 10.1086/133809
- Joy AH (1949) Spectra of the Brighter Variables in Globular Clusters. *ApJ*110:105, DOI 10.1086/145190
- Jurcsik J, Kovacs G (1996) Determination of [Fe/H] from the light curves of RR Lyrae stars. *A&A*312:111–120
- Jurcsik J, Hajdu G, Dékány I, Nuspl J, Catelan M, Grebel EK (2018) Blazhko modulation in the infrared. *ArXiv e-prints* 1801.03436
- Jurkovic MI, Stojanovic M, Ninkovic S (2016) Galactic membership of BL Her type variable stars. *Communications of the Konkoly Observatory Hungary* 105:175–178, 1604.06871
- Kaluzny J, Thompson IB, Krzeminski W, Preston GW, Pych W, Rucinski SM, Schwarzenberg-Czerny A, Szechtman SA, Stachowski G (2005) Eclipsing binaries in globular clusters as age and distance indicators. In: Mikolajewska J, Olech A (eds) *Stellar Astrophysics with the World's Largest Telescopes*, American Institute of Physics Conference Series, vol 752, pp 70–83, DOI 10.1063/1.1893337
- Kaluzny J, Thompson IB, Rozycka M, Dotter A, Krzeminski W, Pych W, Rucinski SM, Burley GS, Szechtman SA (2013) The Cluster AgeS Experiment (CASE). V. Analysis of Three Eclipsing Binaries in the Globular Cluster M4. *AJ*145:43, DOI 10.1088/0004-6256/145/2/43, 1301.2946
- Kaluzny J, Thompson IB, Dotter A, Rozycka M, Pych W, Rucinski SM, Burley GS (2014) The Clusters AgeS Experiment (CASE). VI. Analysis of Two Detached Eclipsing Binaries in the Globular Cluster M55. *Acta Astron.*64:11–26, 1403.6325

- Kaluzny J, Thompson IB, Dotter A, Rozyczka M, Schwarzenberg-Czerny A, Burley GS, Mazur B, Rucinski SM (2015) The Cluster Ages Experiment (CASE). VII. Analysis of Two Eclipsing Binaries in the Globular Cluster NGC 6362. *AJ*150:155, DOI 10.1088/0004-6256/150/5/155, 1508.04894
- Karczmarek P, Pietrzyński G, Gieren W, Suchomska K, Konorski P, Górski M, Pilecki B, Graczyk D, Wielgóski P (2015) The Araucaria Project: The Distance to the Carina Dwarf Galaxy from Infrared Photometry of RR Lyrae Stars. *AJ*150:90, DOI 10.1088/0004-6256/150/3/90, 1507.07713
- Karczmarek P, Pietrzyński G, Belczyński K, Stępień K, Wiktorowicz G, Ilkiewicz K (2016) Contamination of RR Lyrae stars from Binary Evolution Pulsators. In: Rozanska A, Bejger M (eds) 37th Meeting of the Polish Astronomical Society, vol 3, pp 45–48
- Karczmarek P, Pietrzyński G, Górski M, Gieren W, Bersier D (2017a) The Araucaria Project: The Distance to the Fornax Dwarf Galaxy from Near-infrared Photometry of RR Lyrae Stars. *AJ*154:263, DOI 10.3847/1538-3881/aa9574, 1710.10934
- Karczmarek P, Wiktorowicz G, Ilkiewicz K, Smolec R, Stępień K, Pietrzyński G, Gieren W, Belczynski K (2017b) The occurrence of binary evolution pulsators in classical instability strip of RR Lyrae and Cepheid variables. *MNRAS*466:2842–2854, DOI 10.1093/mnras/stw3286, 1612.00465
- Kervella P, Trahin B, Bond HE, Gallenne A, Szabados L, Mérand A, Breiterfelder J, Dailloux J, Anderson RI, Fouqué P, Gieren W, Nardetto N, Pietrzyński G (2017) Observational calibration of the projection factor of Cepheids. III. The long-period Galactic Cepheid RS Puppis. *A&A*600:A127, DOI 10.1051/0004-6361/201630202, 1701.05192
- Kirby EN, Guhathakurta P, Bolte M, Sneden C, Geha MC (2009) Multi-element Abundance Measurements from Medium-resolution Spectra. I. The Sculptor Dwarf Spheroidal Galaxy. *ApJ*705:328–346, DOI 10.1088/0004-637X/705/1/328, 0909.3092
- Klein CR, Richards JW, Butler NR, Bloom JS (2011) Mid-infrared Period-luminosity Relations of RR Lyrae Stars Derived from the WISE Preliminary Data Release. *ApJ*738:185, DOI 10.1088/0004-637X/738/2/185, 1105.0055
- Klein CR, Richards JW, Butler NR, Bloom JS (2012) A Bayesian approach to calibrating period-luminosity relations of RR Lyrae stars in the mid-infrared. *Ap&SS*341:83–87, DOI 10.1007/s10509-012-1035-4, 1202.3990
- Klein CR, Richards JW, Butler NR, Bloom JS (2014) Mid-infrared period-luminosity relations of RR Lyrae stars derived from the AllWISE Data Release. *MNRAS*440:L96–L100, DOI 10.1093/mnras/slu031, 1402.4449
- Koen C, Laney D (1998) On the determination of absolute magnitude zero-points from HIPPARCOS parallaxes. *MNRAS*301:582–584, DOI 10.1046/j.1365-8711.1998.02066.x
- Kollmeier JA, Szczygieł DM, Burns CR, Gould A, Thompson IB, Preston GW, Sneden C, Crane JD, Dong S, Madore BF, Morrell N, Prieto JL, Sheckman S, Simon JD, Villanueva E (2013) The Absolute Magnitude of RRc Variables from Statistical Parallax. *ApJ*775:57, DOI 10.1088/0004-637X/775/1/57, 1208.2689
- Kovacs G, Buchler JR (1988) Regular and irregular nonlinear pulsation in population II Cepheid models. *ApJ*334:971–994, DOI 10.1086/166890
- Kovacs G, Zsoldos E (1995) A new method for the determination of [Fe/H] in RR Lyrae stars. *A&A*293



- Kovtyukh V, Wallerstein G, Yegorova I, Andrievsky S, Korotin S, Saviane I, Belik S, Davis CE, Farrell EM (2018a) Metal-poor Type II Cepheids with Periods Less Than Three Days. *PASP*130(5):054201, DOI 10.1088/1538-3873/aaacf7, 1803.05041
- Kovtyukh V, Yegorova I, Andrievsky S, Korotin S, Saviane I, Lemasle B, Chekhonadskikh F, Belik S (2018b) Type II Cepheids: evidence for Na-O anticorrelation for BL Her type stars? *MNRAS*477:2276–2285, DOI 10.1093/mnras/sty671
- Kudritzki RP, Urbaneja MA (2012) Distances to galaxies from the brightest stars in the Universe. *Ap&SS*341:131–142, DOI 10.1007/s10509-012-1016-7, 1112.3935
- Kuehn CA, Dame K, Smith HA, Catelan M, Jeon YB, Nemeč JM, Walker AR, Kunder A, Pritzl BJ, De Lee N, Borissova J (2013) Variable Stars in Large Magellanic Cloud Globular Clusters. III. Reticulum. *AJ*145:160, DOI 10.1088/0004-6256/145/6/160, 1307.6644
- Kunder A, Chaboyer B (2009) Distance to the Sagittarius Dwarf Galaxy Using Macho Project RR Lyrae Stars. *AJ*137:4478–4486, DOI 10.1088/0004-6256/137/5/4478, 0903.3040
- Kunder A, Valenti E, Dall’Ora M, Pietrukowicz P, Sneden C, Bono G, Braga VF, Ferraro I, Fiorentino G, Iannicola G, Marconi M, Martínez-Vázquez CE, Monelli M, Musella I, Ripepi V, Salaris M, Stetson PB (2018) Impact of Distance Determinations on Galactic Structure. II. Old Tracers. *Space Sci. Rev.*214:90, DOI 10.1007/s11214-018-0519-0, 1806.07487
- Layden AC, Hanson RB, Hawley SL, Klemola AR, Hanley CJ (1996) The Absolute Magnitude and Kinematics of RR Lyrae Stars Via Statistical Parallax. *AJ*112:2110, DOI 10.1086/118167, astro-ph/9608108
- Leaman R, Venn KA, Brooks AM, Battaglia G, Cole AA, Ibata RA, Irwin MJ, McConnachie AW, Mendel JT, Starkenburg E, Tolstoy E (2013) The Comparative Chemical Evolution of an Isolated Dwarf Galaxy: A VLT and Keck Spectroscopic Survey of WLM. *ApJ*767:131, DOI 10.1088/0004-637X/767/2/131, 1302.1879
- Leavitt HS (1908) 1777 variables in the Magellanic Clouds. *Annals of Harvard College Observatory* 60:87–108.3
- Leavitt HS, Pickering EC (1912) Periods of 25 Variable Stars in the Small Magellanic Cloud. *Harvard College Observatory Circular* 173:1–3
- Lee CH, Koppenhoefer J, Seitz S, Bender R, Riffeser A, Kodric M, Hopp U, Snigula J, Gössl C, Kudritzki RP, Burgett W, Chambers K, Hodapp K, Kaiser N, Waters C (2014) Properties of M31. V. 298 Eclipsing Binaries from PAndromeda. *ApJ*797:22, DOI 10.1088/0004-637X/797/1/22, 1411.1115
- Lee MG, Jang IS (2012) The Distance to M101 Hosting Type Ia Supernova 2011fe Based on the Tip of the Red Giant Branch. *ApJ*760:L14, DOI 10.1088/2041-8205/760/1/L14, 1210.6040
- Lee MG, Freedman WL, Madore BF (1993) The Tip of the Red Giant Branch as a Distance Indicator for Resolved Galaxies. *ApJ*417:553, DOI 10.1086/173334
- Lemasle B, Kovtyukh V, Bono G, François P, Saviane I, Yegorova I, Genovali K, Inno L, Galazutdinov G, da Silva R (2015a) Type II Cepheids in the Milky Way disc. Chemical composition of two new W Virginis stars: DD Vel and HQ Car. *A&A*579:A47, DOI 10.1051/0004-6361/201425541, 1505.02789
- Lemasle B, Kovtyukh V, Bono G, François P, Saviane I, Yegorova I, Genovali K, Inno L, Galazutdinov G, da Silva R (2015b) Type II Cepheids in the Milky Way

- disc. Chemical composition of two new W Virginis stars: DD Vel and HQ Car. *A&A*579:A47, DOI 10.1051/0004-6361/201425541, 1505.02789
- Lindegren L, Hog E, van Leeuwen F, Murray CA, Evans DW, Penston MJ, Perryman MAC, Petersen C, Ramamani N, Sniijders MAJ (1992) The NDAC HIPPARCOS data analysis consortium - Overview of the reduction methods. *A&A*258:18–30
- Lindegren L, Lammers U, Bastian U, Hernández J, Klioner S, Hobbs D, Bombrun A, Michalik D, Ramos-Lerate M, Butkevich A, Comoretto G, Joliet E, Holl B, Hutton A, Parsons P, Steidelmüller H, Abbas U, Altmann M, Andrei A, Anton S, Bach N, Barache C, Becciani U, Berthier J, Bianchi L, Biermann M, Bouquillon S, Bourda G, Brüsemeister T, Bucciarelli B, Busonero D, Carlucci T, Castañeda J, Charlot P, Clotet M, Crosta M, Davidson M, de Felice F, Drimmel R, Fabricius C, Fienga A, Figueras F, Fraile E, Gai M, Garralda N, Geyer R, González-Vidal JJ, Guerra R, Hambly NC, Hauser M, Jordan S, Lattanzi MG, Lenhardt H, Liao S, Löffler W, McMillan PJ, Mignard F, Mora A, Morbidelli R, Portell J, Riva A, Sarasso M, Serraller I, Siddiqui H, Smart R, Spagna A, Stampa U, Steele I, Taris F, Torra J, van Reeve W, Vecchiato A, Zschocke S, de Bruijne J, Gracia G, Raison F, Lister T, Marchant J, Messineo R, Soffel M, Osorio J, de Torres A, O’Mullane W (2016) Gaia Data Release 1. Astrometry: one billion positions, two million proper motions and parallaxes. *A&A*595:A4, DOI 10.1051/0004-6361/201628714, 1609.04303
- Liu T, Janes KA (1990) The luminosity scale of RR Lyrae stars with the Baade-Wesselink method. III - The absolute magnitudes of four RR Lyrae stars in the globular cluster M4. *ApJ*360:561–576, DOI 10.1086/169145
- Longmore AJ, Fernley JA, Jameson RF, Sherrington MR, Frank J (1985) VJHK observations of the RR Lyrae star VY Serpentis. *MNRAS*216:873–882, DOI 10.1093/mnras/216.4.873
- Longmore AJ, Fernley JA, Jameson RF (1986) RR Lyrae stars in globular clusters - Better distances from infrared measurements? *MNRAS*220:279–287, DOI 10.1093/mnras/220.2.279
- Luri X, Gomez AE, Torra J, Figueras F, Mennessier MO (1998) The LMC distance modulus from HIPPARCOS RR Lyrae and classical Cepheid data. *A&A*335:L81–L84, [astro-ph/9805215](#)
- Maas T, Van Winckel H, Waelkens C (2002) RU Cen and SX Cen: Two strongly depleted RV Tauri stars in binary systems. The RV Tauri photometric b phenomenon and binarity. *A&A*386:504–516, DOI 10.1051/0004-6361:20020209
- Maas T, Giridhar S, Lambert DL (2007) The Chemical Compositions of the Type II Cepheids-The BL Herculis and W Virginis Variables. *ApJ*666:378–392, DOI 10.1086/520081, 0706.2029
- Mackey AD, Gilmore GF (2004) Photometry of Magellanic Cloud clusters with the Advanced Camera for Surveys - I. The old Large Magellanic Cloud clusters NGC 1928, 1939 and Reticulum. *MNRAS*352:153–167, DOI 10.1111/j.1365-2966.2004.07908.x, [astro-ph/0404247](#)
- Macri LM, Calzetti D, Freedman WL, Gibson BK, Graham JA, Huchra JP, Hughes SMG, Madore BF, Mould JR, Persson SE, Stetson PB (2001) NICMOS Observations of Extragalactic Cepheids. I. Photometry Database and a Test of the Standard Extinction Law. *ApJ*549:721–744, DOI 10.1086/319465, [astro-ph/0102125](#)
- Madore BF (1982) The period-luminosity relation. IV - Intrinsic relations and reddenings for the Large Magellanic Cloud Cepheids. *ApJ*253:575–579, DOI

- 10.1086/159659
- Madore BF, Freedman WL (1995) The tip of the red giant branch as a distance indicator for resolved galaxies. 2: Computer simulations. *AJ*109:1645–1652, DOI 10.1086/117391
- Madore BF, Mager V, Freedman WL (2009) Sharpening the Tip of the Red Giant Branch. *ApJ*690:389–393, DOI 10.1088/0004-637X/690/1/389, 0809.2598
- Madore BF, Hoffman D, Freedman WL, Kollmeier JA, Monson A, Persson SE, Rich JA Jr, Scowcroft V, Seibert M (2013) A Preliminary Calibration of the RR Lyrae Period-Luminosity Relation at Mid-infrared Wavelengths: WISE Data. *ApJ*776:135, DOI 10.1088/0004-637X/776/2/135, 1308.3160
- Madore BF, Freedman WL, Hatt D, Hoyt TJ, Monson AJ, Beaton RL, Rich JA, Jang IS, Lee MG, Scowcroft V, Seibert M (2018) The Near-infrared Tip of the Red Giant Branch. I. A Calibration in the Isolated Dwarf Galaxy IC 1613. *ApJ*858:11, DOI 10.3847/1538-4357/aab7f4, 1803.01278
- Mager VA, Madore BF, Freedman WL (2008) Metallicity-corrected Tip of the Red Giant Branch Distance to NGC 4258. *ApJ*689:721-731, DOI 10.1086/592563, 0808.2180
- Majaess D, Turner D, Lane D (2009) Type II Cepheids as Extragalactic Distance Candles. *Acta Astron.*59:403–418, 0909.0181
- Majewski SR, Siegel MH, Patterson RJ, Rood RT (1999) An Internal Second-Parameter Problem in the Sculptor Dwarf Spheroidal Galaxy. *ApJ*520:L33–L36, DOI 10.1086/312133, astro-ph/9905238
- Majewski SR, Zasowski G, Nidever DL (2011) Lifting the Dusty Veil with Near- and Mid-infrared Photometry. I. Description and Applications of the Rayleigh-Jeans Color Excess Method. *ApJ*739:25, DOI 10.1088/0004-637X/739/1/25, 1106.2542
- Majewski SR, Schiavon RP, Frinchaboy PM, Allende Prieto C, Barkhouser R, Bizyaev D, Blank B, Brunner S, Burton A, Carrera R, Chojnowski SD, Cunha K, Epstein C, Fitzgerald G, García Pérez AE, Hearty FR, Henderson C, Holtzman JA, Johnson JA, Lam CR, Lawler JE, Maseman P, Mészáros S, Nelson M, Nguyen DC, Nidever DL, Pinsonneault M, Shetrone M, Smee S, Smith VV, Stolberg T, Skrutskie MF, Walker E, Wilson JC, Zasowski G, Anders F, Basu S, Beland S, Blanton MR, Bovy J, Brownstein JR, Carlberg J, Chaplin W, Chappini C, Eisenstein DJ, Elsworth Y, Feuillet D, Fleming SW, Galbraith-Frew J, García RA, García-Hernández DA, Gillespie BA, Girardi L, Gunn JE, Hesselquist S, Hayden MR, Hekker S, Ivans I, Kinemuchi K, Klaene M, Mahadevan S, Mathur S, Mosser B, Muna D, Munn JA, Nichol RC, O’Connell RW, Parejko JK, Robin AC, Rocha-Pinto H, Schultheis M, Serenelli AM, Shane N, Silva Aguirre V, Sobek JS, Thompson B, Troup NW, Weinberg DH, Zamora O (2017) The Apache Point Observatory Galactic Evolution Experiment (APOGEE). *AJ*154:94, DOI 10.3847/1538-3881/aa784d, 1509.05420
- Makarov D, Makarova L, Rizzi L, Tully RB, Dolphin AE, Sakai S, Shaya EJ (2006) Tip of the Red Giant Branch Distances. I. Optimization of a Maximum Likelihood Algorithm. *AJ*132:2729–2742, DOI 10.1086/508925, astro-ph/0603073
- Malavolta L, Sneden C, Piotto G, Milone AP, Bedin LR, Nascimbeni V (2014) Atmospheric Parameters and Metallicities for 2191 Stars in the Globular Cluster M4. *AJ*147:25, DOI 10.1088/0004-6256/147/2/25, 1311.2592
- Marconi M, Di Criscienzo M (2007) Updated pulsation models for BL Herculis stars. *A&A*467:223–227, DOI 10.1051/0004-6361:20066646, astro-ph/0701256

- Marconi M, Caputo F, Di Criscienzo M, Castellani M (2003) RR Lyrae Stars in Galactic Globular Clusters. II. A Theoretical Approach to Variables in M3. *ApJ*596:299–313, DOI 10.1086/377641, [astro-ph/0306356](#)
- Marconi M, Musella I, Fiorentino G (2005a) Cepheid Pulsation Models at Varying Metallicity and  $\Delta Y/\Delta Z$ . *ApJ*632:590–610, DOI 10.1086/432790, [astro-ph/0506207](#)
- Marconi M, Nordgren T, Bono G, Schnider G, Caputo F (2005b) Predicted and Empirical Radii of RR Lyrae Stars. *ApJ*623:L133–L136, DOI 10.1086/430273, [astro-ph/0503382](#)
- Marconi M, Bono G, Caputo F, Piersimoni AM, Pietrinferni A, Stellingwerf RF (2011) On the Period Distribution of Cluster RR Lyrae Stars to Constrain Their Helium Content: The Case of  $\omega$  Centauri. *ApJ*738:111, DOI 10.1088/0004-637X/738/1/111, 1106.4931
- Marconi M, Coppola G, Bono G, Braga V, Pietrinferni A, Buonanno R, Castellani M, Musella I, Ripepi V, Stellingwerf RF (2015) On a New Theoretical Framework for RR Lyrae Stars. I. The Metallicity Dependence. *ApJ*808:50, DOI 10.1088/0004-637X/808/1/50, 1505.02531
- Marconi M, Coppola G, Bono G, Braga V, Pietrinferni A (2016) Helium abundance effects on RR Lyrae pulsation properties. *Communications of the Konkoly Observatory Hungary* 105:125–a128
- Marino AF, Villanova S, Piotto G, Milone AP, Momany Y, Bedin LR, Medling AM (2008) Spectroscopic and photometric evidence of two stellar populations in the Galactic globular cluster NGC 6121 (M 4). *A&A*490:625–640, DOI 10.1051/0004-6361:200810389, 0808.1414
- Martell SL, Sharma S, Buder S, Duong L, Schlesinger KJ, Simpson J, Lind K, Ness M, Marshall JP, Asplund M, Bland-Hawthorn J, Casey AR, De Silva G, Freeman KC, Kos J, Lin J, Zucker DB, Zwitter T, Anguiano B, Bacigalupo C, Carollo D, Casagrande L, Da Costa GS, Horner J, Huber D, Hyde EA, Kafle PR, Lewis GF, Nataf D, Navin CA, Stello D, Tinney CG, Watson FG, Wittenmyer R (2017) The GALAH survey: observational overview and Gaia DR1 companion. *MNRAS*465:3203–3219, DOI 10.1093/mnras/stw2835, 1609.02822
- Martínez-Vázquez CE, Monelli M, Bono G, Stetson PB, Ferraro I, Bernard EJ, Gallart C, Fiorentino G, Iannicola G, Udalski A (2015) Variable stars in Local Group Galaxies - I. Tracing the early chemical enrichment and radial gradients in the Sculptor dSph with RR Lyrae stars. *MNRAS*454:1509–1516, DOI 10.1093/mnras/stv2014, 1508.06942
- Martínez-Vázquez CE, Monelli M, Gallart C, Bono G, Bernard EJ, Stetson PB, Ferraro I, Walker AR, Dall’Ora M, Fiorentino G, Iannicola G (2016a) Probing the early chemical evolution of the Sculptor dSph with purely old stellar tracers. *MNRAS*461:L41–L45, DOI 10.1093/mnrasl/slw093, 1605.02768
- Martínez-Vázquez CE, Stetson PB, Monelli M, Bernard EJ, Fiorentino G, Gallart C, Bono G, Cassisi S, Dall’Ora M, Ferraro I, Iannicola G, Walker AR (2016b) Variable stars in Local Group Galaxies - II. Sculptor dSph. *MNRAS*462:4349–4370, DOI 10.1093/mnras/stw1895, 1607.08518
- Martínez-Vázquez CE, Monelli M, Bernard EJ, Gallart C, Stetson PB, Skillman ED, Bono G, Cassisi S, Fiorentino G, McQuinn KBW, Cole AA, McConnachie AW, Martin NF, Dolphin AE, Boylan-Kolchin M, Aparicio A, Hidalgo SL, Weisz DR (2017) The ISLANDS Project. III. Variable Stars in Six Andromeda Dwarf Spheroidal Galaxies. *ApJ*850:137, DOI 10.3847/1538-4357/aa9381, 1710.09038

- Matsunaga N, Fukushi H, Nakada Y, Tanabé T, Feast MW, Menzies JW, Ita Y, Nishiyama S, Baba D, Naoi T, Nakaya H, Kawadu T, Ishihara A, Kato D (2006) The period-luminosity relation for type II Cepheids in globular clusters. *MNRAS*370:1979–1990, DOI 10.1111/j.1365-2966.2006.10620.x, [astro-ph/0606609](#)
- Matsunaga N, Feast MW, Kawadu T, Nishiyama S, Nagayama T, Nagata T, Tamura M, Bono G, Kobayashi N (2013) Cepheids and other short-period variables near the Galactic Centre. *MNRAS*429:385–397, DOI 10.1093/mnras/sts343, 1211.0151
- McGonegal R, McAlary CW, Madore BF, McLaren RA (1982) The Cepheid distance scale - A new application for infrared photometry. *ApJ*257:L33–L36, DOI 10.1086/183803
- McNamara DH (1995) Period-Luminosity Relations of Population II Cepheids. *AJ*109:2134, DOI 10.1086/117438
- McNamara DH (1997) The Absolute Magnitudes of the RR Lyrae Stars. *PASP*109:857–867, DOI 10.1086/133956
- McWilliam A (ed) (2011) RR Lyrae Stars, Metal-Poor Stars, and the Galaxy, vol 5, 1109.1324
- Méndez B, Davis M, Moustakas J, Newman J, Madore BF, Freedman WL (2002) Deviations from the Local Hubble Flow. I. The Tip of the Red Giant Branch as a Distance Indicator. *AJ*124:213–233, DOI 10.1086/341168, [astro-ph/0204192](#)
- Michalik D, Lindegren L, Hobbs D (2015) The Tycho-Gaia astrometric solution . How to get 2.5 million parallaxes with less than one year of Gaia data. *A&A*574:A115, DOI 10.1051/0004-6361/201425310, 1412.8770
- Miyoshi M, Moran J, Herrnstein J, Greenhill L, Nakai N, Diamond P, Inoue M (1995) Evidence for a black hole from high rotation velocities in a sub-parsec region of NGC4258. *Nature*373:127–129, DOI 10.1038/373127a0
- Monson AJ, Beaton RL, Scowcroft V, Freedman WL, Madore BF, Rich JA, Seibert M, Kollmeier JA, Clementini G (2017) Standard Galactic Field RR Lyrae. I. Optical to Mid-infrared Phased Photometry. *AJ*153:96, DOI 10.3847/1538-3881/153/3/96, 1703.01520
- Moretti MI, Clementini G, Muraveva T, Ripepi V, Marquette JB, Cioni MRL, Marconi M, Girardi L, Rubele S, Tisserand P, de Grijs R, Groenewegen MAT, Guandalini R, Ivanov VD, van Loon JT (2014) The VMC Survey - X. Cepheids, RR Lyrae stars and binaries as probes of the Magellanic System's structure. *MNRAS*437:2702–2719, DOI 10.1093/mnras/stt2081, 1310.6849
- Mouhcine M, Ferguson HC, Rich RM, Brown TM, Smith TE (2005) Halos of Spiral Galaxies. I. The Tip of the Red Giant Branch as a Distance Indicator. *ApJ*633:810–820, DOI 10.1086/468177, [astro-ph/0510253](#)
- Mould J, Sakai S (2008) The Extragalactic Distance Scale without Cepheids. *ApJ*686:L75, DOI 10.1086/592964
- Muraveva T, Palmer M, Clementini G, Luri X, Cioni MRL, Moretti MI, Marconi M, Ripepi V, Rubele S (2015) New Near-infrared Period-Luminosity-Metallicity Relations for RR Lyrae Stars and the Outlook for Gaia. *ApJ*807:127, DOI 10.1088/0004-637X/807/2/127, 1505.06001
- Muraveva T, Delgado HE, Clementini G, Sarro LM, Garofalo A (2018a) RR Lyrae stars as standard candles in the Gaia Data Release 2 Era. *ArXiv e-prints* 1805.08742
- Muraveva T, Garofalo A, Scowcroft V, Clementini G, Freedman WL, Madore BF,

- Monson AJ (2018b) The Carnegie RR Lyrae Program: Mid-infrared Period-Luminosity relations of RR Lyrae stars in Reticulum. MNRASDOI 10.1093/mnras/sty1959, 1807.07493
- Muraveva T, Subramanian S, Clementini G, Cioni MRL, Palmer M, van Loon JT, Moretti MI, de Grijs R, Molinaro R, Ripepi V, Marconi M, Emerson J, Ivanov VD (2018c) The VMC survey - XXVI. Structure of the Small Magellanic Cloud from RR Lyrae stars. MNRAS473:3131–3146, DOI 10.1093/mnras/stx2514, 1709.09064
- Neeley JR, Marengo M, Bono G, Braga VF, Dall’Ora M, Stetson PB, Buonanno R, Ferraro I, Freedman WL, Iannicola G, Madore BF, Matsunaga N, Monson A, Persson SE, Scowcroft V, Seibert M (2015) On the Distance of the Globular Cluster M4 (NGC 6121) Using RR Lyrae Stars. II. Mid-infrared Period-luminosity Relations. ApJ808:11, DOI 10.1088/0004-637X/808/1/11, 1505.07858
- Neeley JR, Marengo M, Bono G, Braga VF, Dall’Ora M, Magurno D, Marconi M, Trueba N, Tognelli E, Prada Moroni PG, Beaton RL, Freedman WL, Madore BF, Monson AJ, Scowcroft V, Seibert M, Stetson PB (2017) On a New Theoretical Framework for RR Lyrae Stars. II. Mid-infrared Period-Luminosity-Metallicity Relations. ApJ841:84, DOI 10.3847/1538-4357/aa713d, 1705.01970
- Ngeow CC, Kanbur SM, Nikolaev S, Buonaccorsi J, Cook KH, Welch DL (2005) Further empirical evidence for the non-linearity of the period-luminosity relations as seen in the Large Magellanic Cloud Cepheids. MNRAS363:831–846, DOI 10.1111/j.1365-2966.2005.09477.x, astro-ph/0507601
- Oosterhoff PT (1939) Some remarks on the variable stars in globular clusters. The Observatory 62:104–109
- Peimbert A, Peimbert M (2010) On the O/H, Mg/H, Si/H, and Fe/H Gas and Dust Abundance Ratios in Galactic and Extragalactic H II Regions. ApJ724:791–798, DOI 10.1088/0004-637X/724/1/791, 1006.0692
- Perryman MAC, Lindegren L, Kovalevsky J, Hoeg E, Bastian U, Bernacca PL, Crézé M, Donati F, Grenon M, Grewing M, van Leeuwen F, van der Marel H, Mignard F, Murray CA, Le Poole RS, Schrijver H, Turon C, Arenou F, Froeschlé M, Petersen CS (1997) The HIPPARCOS Catalogue. A&A323:L49–L52
- Perryman MAC, de Boer KS, Gilmore G, Høg E, Lattanzi MG, Lindegren L, Luri X, Mignard F, Pace O, de Zeeuw PT (2001) GAIA: Composition, formation and evolution of the Galaxy. A&A369:339–363, DOI 10.1051/0004-6361:20010085, astro-ph/0101235
- Pickering EC (1889) Variable Star in Cluster G.C. 3636. Astronomische Nachrichten 123:207, DOI 10.1002/asna.18901231306
- Pickering EC, Colson HR, Fleming WP, Wells LD (1901) Sixty-four new variable stars. ApJ13, DOI 10.1086/140808
- Pietrinferni A, Cassisi S, Salaris M, Castelli F (2004) A Large Stellar Evolution Database for Population Synthesis Studies. I. Scaled Solar Models and Isochrones. ApJ612:168–190, DOI 10.1086/422498, astro-ph/0405193
- Pietrzyński G, Gieren W, Soszyński I, Bresolin F, Kudritzki RP, Dall’Ora M, Storm J, Bono G (2006) The Araucaria Project: The Distance to the Local Group Galaxy IC 1613 from Near-Infrared Photometry of Cepheid Variables. ApJ642:216–224, DOI 10.1086/500926, astro-ph/0601309
- Pietrzyński G, Gieren W, Szewczyk O, Walker A, Rizzi L, Bresolin F, Kudritzki RP, Nalewajko K, Storm J, Dall’Ora M, Ivanov V (2008) The Araucaria Project:

- the Distance to the Sculptor Dwarf Spheroidal Galaxy from Infrared Photometry of RR Lyrae Stars. *AJ*135:1993–1997, DOI 10.1088/0004-6256/135/6/1993, 0804.0347
- Pietrzyński G, Górski M, Gieren W, Laney D, Udalski A, Ciechanowska A (2010) The Araucaria Project. Population Effects on the V- and I-band Magnitudes of Red Clump Stars. *AJ*140:1038–1042, DOI 10.1088/0004-6256/140/4/1038, 1008.1259
- Pietrzyński G, Graczyk D, Gieren W, Thompson IB, Pilecki B, Udalski A, Soszyński I, Kozłowski S, Konorski P, Suchomska K, Bono G, Moroni PGP, Villanova S, Nardetto N, Bresolin F, Kudritzki RP, Storm J, Gallenne A, Smolec R, Minniti D, Kubiak M, Szymański MK, Poleski R, Wyrzykowski L, Ulaczyk K, Pietrukowicz P, Górski M, Karczmarek P (2013) An eclipsing-binary distance to the Large Magellanic Cloud accurate to two per cent. *Nature*495:76–79, DOI 10.1038/nature11878, 1303.2063
- Pilecki B, Gieren W, Smolec R, Pietrzyński G, Thompson IB, Anderson RI, Bono G, Soszyński I, Kervella P, Nardetto N, Taormina M, Stępień K, Wielgórski P (2017) Mass and p-factor of the Type II Cepheid OGLE-LMC-T2CEP-098 in a Binary System. *ApJ*842:110, DOI 10.3847/1538-4357/aa6ff7, 1704.07782
- Pilecki B, Gieren W, Pietrzyński G, Thompson IB, Smolec R, Graczyk D, Taormina M, Udalski A, Storm J, Nardetto N, Gallenne A, Kervella P, Soszyński I, Górski M, Wielgórski P, Suchomska K, Karczmarek P, Zgirski B (2018) The Araucaria Project: High-precision Cepheid Astrophysics from the Analysis of Variables in Double-lined Eclipsing Binaries. *ApJ*862:43, DOI 10.3847/1538-4357/aacb32, 1806.01391
- Popowski P, Gould A (1997) Mathematics of Statistical Parallax and the Local Distance Scale. ArXiv Astrophysics e-prints [astro-ph/9703140](https://arxiv.org/abs/astro-ph/9703140)
- Popowski P, Gould A (1998a) Systematics of RR Lyrae Statistical Parallax. I. Mathematics. *ApJ*506:259–270, DOI 10.1086/306216
- Popowski P, Gould A (1998b) Systematics of RR Lyrae Statistical Parallax. II. Proper Motions and Radial Velocities. *ApJ*506:271–280, DOI 10.1086/306239
- Preston GW (1959) A Spectroscopic Study of the RR Lyrae Stars. *ApJ*130:507, DOI 10.1086/146743
- Pritzl BJ, Smith HA, Stetson PB, Catelan M, Sweigart AV, Layden AC, Rich RM (2003) Hubble Space Telescope Snapshot Study of Variable Stars in Globular Clusters: The Inner Region of NGC 6441. *AJ*126:1381–1401, DOI 10.1086/377024, [astro-ph/0305339](https://arxiv.org/abs/astro-ph/0305339)
- Rabidoux K, Smith HA, Pritzl BJ, Osborn W, Kuehn C, Randall J, Lustig R, Wells K, Taylor L, De Lee N, Kinemuchi K, LaCluyzé A, Hartley D, Greenwood C, Ingber M, Ireland M, Pellegrini E, Anderson M, Purdum G, Lacy J, Curtis M, Smolinski J, Danford S (2010) Light Curves and Period Changes of Type II Cepheids in the Globular Clusters M3 and M5. *AJ*139:2300–2307, DOI 10.1088/0004-6256/139/6/2300, 1003.5924
- Reid IN (1999) The HR Diagram and the Galactic Distance Scale After HIPPARCOS. *ARA&A*37:191–237, DOI 10.1146/annurev.astro.37.1.191
- Rey SC, Lee YW, Joo JM, Walker A, Baird S (2000) CCD Photometry of the Globular Cluster  $\omega$  Centauri. I. Metallicity of RR Lyrae Stars from CABY Photometry. *AJ*119:1824–1838, DOI 10.1086/301304, [astro-ph/0001101](https://arxiv.org/abs/astro-ph/0001101)
- Rich JA, Persson SE, Freedman WL, Madore BF, Monson AJ, Scowcroft V, Seibert M (2014) A New Cepheid Distance Measurement and Method for NGC 6822.

- ApJ794:107, DOI 10.1088/0004-637X/794/2/107, 1409.6830
- Ricker GR, Winn JN, Vanderspek R, Latham DW, Bakos GÁ, Bean JL, Bert-Thompson ZK, Brown TM, Buchhave L, Butler NR, Butler RP, Chaplin WJ, Charbonneau D, Christensen-Dalsgaard J, Clampin M, Deming D, Doty J, De Lee N, Dressing C, Dunham EW, Endl M, Fressin F, Ge J, Henning T, Holman MJ, Howard AW, Ida S, Jenkins JM, Jernigan G, Johnson JA, Kaltenegger L, Kawai N, Kjeldsen H, Laughlin G, Levine AM, Lin D, Lissauer JJ, MacQueen P, Marcy G, McCullough PR, Morton TD, Narita N, Paegert M, Palte E, Pepe F, Pepper J, Quirrenbach A, Rinehart SA, Sasselov D, Sato B, Seager S, Sozzetti A, Stassun KG, Sullivan P, Szentgyorgyi A, Torres G, Udry S, Villaseñor J (2015) Transiting Exoplanet Survey Satellite (TESS). *Journal of Astronomical Telescopes, Instruments, and Systems* 1(1):014003, DOI 10.1117/1.JATIS.1.1.014003
- Riess AG (2011) An Independent Determination of WFC3-IR Zeropoints and Count Rate Non-Linearity from 2MASS Asterisms. Tech. rep.
- Riess AG, Macri L, Casertano S, Lampeitl H, Ferguson HC, Filippenko AV, Jha SW, Li W, Chornock R (2011) A 3% Solution: Determination of the Hubble Constant with the Hubble Space Telescope and Wide Field Camera 3. *ApJ*730:119, DOI 10.1088/0004-637X/730/2/119, 1103.2976
- Riess AG, Macri L, Casertano S, Lampeitl H, Ferguson HC, Filippenko AV, Jha SW, Li W, Chornock R, Silverman JM (2012) Erratum: "A 3% Solution: Determination of the Hubble Constant with the Hubble Space Telescope and Wide Field Camera 3" [iA href="/abs/2011ApJ...730..119R" i\(2011, ApJ, 730, 119\);/A i. ApJ752:76, DOI 10.1088/0004-637X/752/1/76](#)
- Riess AG, Macri LM, Hoffmann SL, Scolnic D, Casertano S, Filippenko AV, Tucker BE, Reid MJ, Jones DO, Silverman JM, Chornock R, Challis P, Yuan W, Brown PJ, Foley RJ (2016) A 2.4% Determination of the Local Value of the Hubble Constant. *ApJ*826:56, DOI 10.3847/0004-637X/826/1/56
- Ripepi V, Moretti MI, Clementini G, Marconi M, Cioni MR, Marquette JB, Tisserand P (2012a) Preliminary results for RR Lyrae stars and Classical Cepheids from the Vista Magellanic Cloud (VMC) survey. *Ap&SS*341:51–56, DOI 10.1007/s10509-012-1021-x, 1202.5863
- Ripepi V, Moretti MI, Marconi M, Clementini G, Cioni MRL, Marquette JB, Girardi L, Rubele S, Groenewegen MAT, de Grijs R, Gibson BK, Oliveira JM, van Loon JT, Emerson JP (2012b) The VMC survey - V. First results for classical Cepheids. *MNRAS*424:1807–1816, DOI 10.1111/j.1365-2966.2012.21274.x, 1204.2273
- Ripepi V, Moretti MI, Marconi M, Clementini G, Cioni MRL, de Grijs R, Emerson JP, Groenewegen MAT, Ivanov VD, Muraveva T, Piatti AE, Subramanian S (2015) The VMC Survey - XIII. Type II Cepheids in the Large Magellanic Cloud. *MNRAS*446:3034–3061, DOI 10.1093/mnras/stu2260, 1410.7817
- Ritter A (1879) Untersuchungen über die Höhe der Atmosphäre und die Constitution gasförmiger Weltkörper. *Annalen der Physik* 244:157–183, DOI 10.1002/andp.18792440910
- Rizzi L (2002) . PhD thesis, University of Padova, Italy
- Rizzi L, Tully RB, Makarov D, Makarova L, Dolphin AE, Sakai S, Shaya EJ (2007) Tip of the Red Giant Branch Distances. II. Zero-Point Calibration. *ApJ*661:815–829, DOI 10.1086/516566, astro-ph/0701518
- Rosenfield P, Marigo P, Girardi L, Dalcanton JJ, Bressan A, Gullieuszik M, Weisz



- D, Williams BF, Dolphin A, Aringer B (2014) Evolution of Thermally Pulsing Asymptotic Giant Branch Stars. IV. Constraining Mass loss and Lifetimes of Low Mass, Low Metallicity AGB Stars. *ApJ*790:22, DOI 10.1088/0004-637X/790/1/22, 1406.0676
- Rosenfield P, Marigo P, Girardi L, Dalcanton JJ, Bressan A, Williams BF, Dolphin A (2016) Evolution of Thermally Pulsing Asymptotic Giant Branch Stars. V. Constraining the Mass Loss and Lifetimes of Intermediate-mass, Low-metallicity AGB Stars. *ApJ*822:73, DOI 10.3847/0004-637X/822/2/73, 1603.05283
- Rozyczka M, Kaluzny J, Thompson IB, Dotter A, Pych W, Narloch W (2014) The Clusters AgeS Experiment (CASE). Analysis of the Detached Eclipsing Binary V15 in the Metal-Rich Open Cluster NGC 6253. *Acta Astron.*64:233–246, 1410.1324
- Russell SC (1998) RV Tau Variables in Globular Clusters: Clues on Their Nature? *PASA*15:189–193, DOI 10.1071/AS98189
- Sakai S, Madore BF, Freedman WL (1996) Tip of the Red Giant Branch Distances to Galaxies. III. The Dwarf Galaxy Sextans A. *ApJ*461:713, DOI 10.1086/177096
- Sakai S, Ferrarese L, Kennicutt RC Jr, Saha A (2004) The Effect of Metallicity on Cepheid-based Distances. *ApJ*608:42–61, DOI 10.1086/386540, astro-ph/0402499
- Salaris M, Cassisi S (1997) The ‘tip’ of the red giant branch as a distance indicator: results from evolutionary models. *MNRAS*289:406–414, DOI 10.1093/mnras/289.2.406, astro-ph/9703186
- Salaris M, Cassisi S (1998) A new analysis of the red giant branch ‘tip’ distance scale and the value of the Hubble constant. *MNRAS*298:166–178, DOI 10.1046/j.1365-8711.1998.01598.x, astro-ph/9803103
- Salaris M, Cassisi S (2005) Evolution of Stars and Stellar Populations
- Salaris M, Girardi L (2005) Tip of the Red Giant Branch distances to galaxies with composite stellar populations. *MNRAS*357:669–678, DOI 10.1111/j.1365-2966.2005.08689.x, astro-ph/0412156
- Salaris M, Cassisi S, Weiss A (2002) Red Giant Branch Stars: The Theoretical Framework. *PASP*114:375–402, DOI 10.1086/342498, astro-ph/0201387
- Salaris M, de Boer T, Tolstoy E, Fiorentino G, Cassisi S (2013) The horizontal branch of the Sculptor dwarf galaxy. *A&A*559:A57, DOI 10.1051/0004-6361/201322501, 1309.4353
- Samus NN, Kazarovets EV, Durlevich OV, Kireeva NN, Pastukhova EN (2017) General catalogue of variable stars: Version GCVS 5.1. *Astronomy Reports* 61:80–88, DOI 10.1134/S1063772917010085
- Sandage A (1958) The Color-Magnitude Diagrams of Galactic and Globular Clusters and their Interpretation as Age Groups. *Ricerche Astronomiche* 5:41
- Sandage A (1971) The Distance of the Local-Group Galaxy IC 1613 Obtained from Baade’s Work on its Stellar Content. *ApJ*166:13, DOI 10.1086/150939
- Sandage A (1982) The Oosterhoff period groups and the age of globular clusters. III - The age of the globular cluster system. *ApJ*252:553–581, DOI 10.1086/159582
- Sandage A (2004) The Mount Wilson Observatory
- Sandage A (2006) On the Predicted and Observed Color Boundaries of the RR Lyrae Instability Strip as a Function of Metallicity. *AJ*131:1750–1765, DOI 10.1086/500012, astro-ph/0508057
- Sandage A, Katem B (1982) On the intrinsic widths of the subgiant and horizontal branch sequences in the globular cluster M3. *AJ*87:537–554, DOI

- 10.1086/113127
- Sandage A, Tammann GA (2006) Absolute Magnitude Calibrations of Population I and II Cepheids and Other Pulsating Variables in the Instability Strip of the Hertzsprung-Russell Diagram. *ARA&A*44:93–140, DOI 10.1146/annurev.astro.43.072103.150612
- Sandage A, Wallerstein G (1960) Color-Magnitude Diagram for Disk Globular Cluster NGC 6356 Compared with Halo Clusters. *ApJ*131:598, DOI 10.1086/146872
- Sandage A, Beaton RL, Majewski SR (2016) Comparison of Hipparcos Trigonometric and Mount Wilson Spectroscopic Parallaxes for 90 Subgiants that Defined the Class in 1935. *PASP*128(6):064202, DOI 10.1088/1538-3873/128/964/064202, 1511.05930
- Sarajedini A, Barker MK, Geisler D, Harding P, Schommer R (2006) RR Lyrae Variables in M33. I. Evidence for a Field Halo Population. *AJ*132:1361–1371, DOI 10.1086/506152, astro-ph/0605580
- Sarajedini A, Mancone CL, Lauer TR, Dressler A, Freedman W, Trager SC, Grillmair C, Mighell KJ (2009) RR Lyrae Variables in Two Fields in the Spheroid of M31. *AJ*138:184–195, DOI 10.1088/0004-6256/138/1/184, 0904.4290
- Saviane I, Hibbard JE, Rich RM (2004) The Stellar Content of the Southern Tail of NGC 4038/4039 and a Revised Distance. *AJ*127:660–678, DOI 10.1086/381059, astro-ph/0311200
- Saviane I, Momany Y, da Costa GS, Rich RM, Hibbard JE (2008) A New Red Giant-based Distance Modulus of 13.3 Mpc to the Antennae Galaxies and Its Consequences. *ApJ*678:179–186, DOI 10.1086/533408, 0802.1045
- Schechter PL, Mateo M, Saha A (1993) DOPHOT, a CCD photometry program: Description and tests. *PASP*105:1342–1353, DOI 10.1086/133316
- Schlafly EF, Finkbeiner DP (2011) Measuring Reddening with Sloan Digital Sky Survey Stellar Spectra and Recalibrating SFD. *ApJ*737:103, DOI 10.1088/0004-637X/737/2/103, 1012.4804
- Schlegel DJ, Finkbeiner DP, Davis M (1998) Maps of Dust Infrared Emission for Use in Estimation of Reddening and Cosmic Microwave Background Radiation Foregrounds. *ApJ*500:525–553, DOI 10.1086/305772, astro-ph/9710327
- Schwarzschild M (1940) On the variables in Messier 3. *Harvard College Observatory Circular* 437:1–12
- Schwarzschild M, Härm R (1970) On the Evolutionary Phase of Cepheids in Globular Clusters. *ApJ*160:341, DOI 10.1086/150433
- Schweizer F, Burns CR, Madore BF, Mager VA, Phillips MM, Freedman WL, Boldt L, Contreras C, Folatelli G, González S, Hamuy M, Krzeminski W, Morrell NI, Persson SE, Roth MR, Stritzinger MD (2008) A New Distance to the Antennae Galaxies (NGC 4038/39) Based on the Type Ia Supernova 2007sr. *AJ*136:1482–1489, DOI 10.1088/0004-6256/136/4/1482, 0807.3955
- Scowcroft V, Freedman WL, Madore BF, Monson AJ, Persson SE, Seibert M, Rigby JR, Melbourne J (2013) The Carnegie Hubble Program: The Infrared Leavitt Law in IC 1613. *ApJ*773:106, DOI 10.1088/0004-637X/773/2/106, 1306.5802
- Serenelli A, Weiss A, Cassisi S, Salaris M, Pietrinferni A (2017) The brightness of the red giant branch tip. Theoretical framework, a set of reference models, and predicted observables. *A&A*606:A33, DOI 10.1051/0004-6361/201731004, 1706.09910

- Sesar B (2012) Template RR Lyrae  $H\alpha$ ,  $H\beta$ , and  $H\gamma$  Velocity Curves. *AJ*144:114, DOI 10.1088/0004-6256/144/4/114, 1208.1997
- Sesar B, Fousneau M, Price-Whelan AM, Bailer-Jones CAL, Gould A, Rix HW (2017) A Probabilistic Approach to Fitting Period-luminosity Relations and Validating Gaia Parallaxes. *ApJ*838:107, DOI 10.3847/1538-4357/aa643b, 1611.07035
- Shapley H (1914) On the Nature and Cause of Cepheid Variation. *ApJ*40:448, DOI 10.1086/142137
- Skarka M (2014) Bright Blazhko RRab Lyrae stars observed by ASAS and the SuperWASP surveys. *A&A*562:A90, DOI 10.1051/0004-6361/201322491, 1402.3111
- Skillen I, Fernley JA, Stobie RS, Jameson RF (1993) The Absolute Magnitudes of RR-Lyrae Stars - Part Five - Wy-Antliae W-Crateris Rv-Octantis Bb-Puppis. *MNRAS*265:301, DOI 10.1093/mnras/265.2.301
- Smeyers P, van Hoolst T (eds) (2010) Linear Isentropic Oscillations of Stars: Theoretical Foundations, Astrophysics and Space Science Library, vol 371, DOI 10.1007/978-3-642-13030-4
- Smith GH, Dopita MA (1983) The chemical inhomogeneity of the Sculptor dwarf spheroidal galaxy. *ApJ*271:113–122, DOI 10.1086/161180
- Smith HA (1995) RR Lyrae stars. Cambridge Astrophysics Series 27
- Smolec R (2005) Metallicity Dependence of the Blazhko Effect. *Acta Astron.*55:59–84, [astro-ph/0503614](https://arxiv.org/abs/astro-ph/0503614)
- Smolec R (2016) Survey of non-linear hydrodynamic models of type-II Cepheids. *MNRAS*456:3475–3493, DOI 10.1093/mnras/stv2868, 1512.01550
- Snedden C, Preston GW, Kollmeier JA, Crane JD, Morrell N, Prieto JL, Sheckman SA, Skowron DM, Thompson IB (2018) Metal-rich RRc Stars in the Carnegie RR Lyrae Survey. *AJ*155:45, DOI 10.3847/1538-3881/aa9f16, 1712.00159
- Sobel D (2016) The Glass Universe: How the Ladies of the Harvard Observatory Took the Measure of the Stars. Penguin Publishing Group, URL <https://books.google.com/books?id=wcq-CwAAQBAJ>
- Solano E (1998) The Absolute Magnitude of RR Lyraes: from HIPPARCOS Parallaxes and Proper Motions. *Ap&SS*263:219–222, DOI 10.1023/A:1002114428541
- Sollima A, Cacciari C, Valenti E (2006) The RR Lyrae period-K-luminosity relation for globular clusters: an observational approach. *MNRAS*372:1675–1680, DOI 10.1111/j.1365-2966.2006.10962.x, [astro-ph/0608397](https://arxiv.org/abs/astro-ph/0608397)
- Sollima A, Cacciari C, Arkharov AAH, Larionov VM, Gorshanov DL, Efimova NV, Piersimoni A (2008) The infrared JHK light curves of RR Lyr. *MNRAS*384:1583–1587, DOI 10.1111/j.1365-2966.2007.12804.x, 0712.0578
- Soszyński I, Udalski A, Szymański MK, Kubiak M, Pietrzyński G, Wyrzykowski L, Szewczyk O, Ulaczyk K, Poleski R (2008) The Optical Gravitational Lensing Experiment. The OGLE-III Catalog of Variable Stars. II. Type II Cepheids and Anomalous Cepheids in the Large Magellanic Cloud. *Acta Astron.*58:293, 0811.3636
- Soszyński I, Udalski A, Szymański MK, Kubiak M, Pietrzyński G, Wyrzykowski L, Ulaczyk K, Poleski R (2010) The Optical Gravitational Lensing Experiment. The OGLE-III Catalog of Variable Stars. VIII. Type II Cepheids in the Small Magellanic Cloud. *Acta Astron.*60:91–107, 1005.3544
- Soszyński I, Udalski A, Szymański MK, Skowron D, Pietrzyński G, Poleski R, Pietrukowicz P, Skowron J, Mróz P, Kozłowski S, Wyrzykowski L, Ulaczyk K,

- Pawlak M (2015) The OGLE Collection of Variable Stars. Classical Cepheids in the Magellanic System. *Acta Astron.*65:297–312, 1601.01318
- Soszyński I, Smolec R, Dziembowski WA, Udalski A, Szymański MK, Wyrzykowski L, Ulaczyk K, Poleski R, Pietrukowicz P, Kozłowski S, Skowron D, Skowron J, Mróz P, Pawlak M (2016a) Anomalous double-mode RR Lyrae stars in the Magellanic Clouds. *MNRAS*463:1332–1341, DOI 10.1093/mnras/stw1933, 1608.00576
- Soszyński I, Udalski A, Szymański MK, Wyrzykowski L, Ulaczyk K, Poleski R, Pietrukowicz P, Kozłowski S, Skowron DM, Skowron J, Mróz P, Pawlak M (2016b) The OGLE Collection of Variable Stars. Over 45 000 RR Lyrae Stars in the Magellanic System. *Acta Astron.*66:131–147, 1606.02727
- Soszyński I, Udalski A, Szymański MK, Wyrzykowski L, Ulaczyk K, Poleski R, Pietrukowicz P, Kozłowski S, Skowron DM, Skowron J, Mróz P, Pawlak M, Rybicki K, Jacyszyn-Dobrzeńska A (2017) The OGLE Collection of Variable Stars. Classical, Type II, and Anomalous Cepheids toward the Galactic Center. *Acta Astron.*67:297–316, 1712.01307
- Soszyński I, Udalski A, Szymański MK, Wyrzykowski L, Ulaczyk K, Poleski R, Pietrukowicz P, Kozłowski S, Skowron D, Skowron J, Mróz P, Rybicki K, Iwanek P (2018) The OGLE Collection of Variable Stars. Type II Cepheids in the Magellanic System. *Acta Astron.*68:89–109, 1807.00008
- Starkenburger E, Hill V, Tolstoy E, François P, Irwin MJ, Boschman L, Venn KA, de Boer TJJ, Lemasle B, Jablonka P, Battaglia G, Groot P, Kaper L (2013) The extremely low-metallicity tail of the Sculptor dwarf spheroidal galaxy. *A&A*549:A88, DOI 10.1051/0004-6361/201220349, 1211.4592
- Steinmetz M, Zwitter T, Siebert A, Watson FG, Freeman KC, Munari U, Campbell R, Williams M, Seabroke GM, Wyse RFG, Parker QA, Bienaymé O, Roeser S, Gibson BK, Gilmore G, Grebel EK, Helmi A, Navarro JF, Burton D, Cass CJP, Dawe JA, Fiegert K, Hartley M, Russell KS, Saunders W, Enke H, Bailin J, Binney J, Bland-Hawthorn J, Boeche C, Dehnen W, Eisenstein DJ, Evans NW, Fiorucci M, Fulbright JP, Gerhard O, Jauregi U, Kelz A, Mijović L, Minchev I, Parmentier G, Peñarrubia J, Quillen AC, Read MA, Ruchti G, Scholz RD, Siviero A, Smith MC, Sordo R, Veltz L, Vidrih S, von Berlepsch R, Boyle BJ, Schilbach E (2006) The Radial Velocity Experiment (RAVE): First Data Release. *AJ*132:1645–1668, DOI 10.1086/506564, astro-ph/0606211
- Stellingwerf RF (1974) The Calculation of Periodic Pulsations of Stellar Models. *ApJ*192:139–146, DOI 10.1086/153043
- Stellingwerf RF (1979) Pulsation in the lower Cepheid strip. I - Linear survey. *ApJ*227:935–942, DOI 10.1086/156802
- Stellingwerf RF (1982) Convection in pulsating stars. I - Nonlinear hydrodynamics. II - RR Lyrae convection and stability. *ApJ*262:330–343, DOI 10.1086/160425
- Stellingwerf RF (1983) Hydra - an Implicit Partial Differential Equation Relaxation Stability Analysis Package. *ApJ*271:876, DOI 10.1086/161253
- Stetson PB (1987) DAOPHOT - A computer program for crowded-field stellar photometry. *PASP*99:191–222, DOI 10.1086/131977
- Stetson PB (1994) The center of the core-cusp globular cluster M15: CFHT and HST Observations, ALLFRAME reductions. *PASP*106:250–280, DOI 10.1086/133378
- Stetson PB, Hesser JE, Smecker-Hane TA (1998) Homogeneous Photometry for Star Clusters and Resolved Galaxies. I. A Survey of Bright Stars in the Fornax

- Dwarf Spheroidal Galaxy. *PASP*110:533–552, DOI 10.1086/316164
- Stetson PB, Braga VF, Dall’Ora M, Bono G, Buonanno R, Ferraro I, Iannicola G, Marengo M, Neeley J (2014a) Optical and Near-Infrared UBVRIJHK Photometry for the RR Lyrae Stars in the Nearby Globular Cluster M4 (NGC 6121). *PASP*126:521, DOI 10.1086/677195, 1406.7531
- Stetson PB, Fiorentino G, Bono G, Bernard EJ, Monelli M, Iannicola G, Gallart C, Ferraro I (2014b) Homogeneous Photometry VI: Variable Stars in the Leo I Dwarf Spheroidal Galaxy. *PASP*126:616–641, DOI 10.1086/677352, 1406.6704
- Storm J (2004) The distance to  $j$ ASTROBJ $_{\lambda}$ IC 4499 $_{j}$ /ASTROBJ $_{\lambda}$  from K-band photometry of 32 RR Lyrae stars. *A&A*15:987–991, DOI 10.1051/0004-6361:20034287, astro-ph/0401237
- Storm J, Gieren W, Fouqué P, Barnes TG, Soszyński I, Pietrzyński G, Nardetto N, Quetz D (2011) Calibrating the Cepheid period-luminosity relation from the infrared surface brightness technique. II. The effect of metallicity and the distance to the LMC. *A&A*534:A95, DOI 10.1051/0004-6361/201117154, 1109.2016
- Subramanian S, Marengo M, Bhardwaj A, Huang Y, Inno L, Nakagawa A, Storm J (2017) Young and Intermediate-Age Distance Indicators. *Space Sci. Rev.*212:1817–1869, DOI 10.1007/s11214-017-0427-8, 1709.07265
- Szabó R, Kolláth Z, Buchler JR (2004) Automated nonlinear stellar pulsation calculations: Applications to RR Lyrae stars. The slope of the fundamental blue edge and the first RRd model survey. *A&A*425:627–639, DOI 10.1051/0004-6361:20035698, astro-ph/0406373
- Szabó R, Benkő JM, Páparó M, Chapellier E, Poretti E, Baglin A, Weiss WW, Kolenberg K, Guggenberger E, Le Borgne JF (2014) Revisiting CoRoT RR Lyrae stars: detection of period doubling and temporal variation of additional frequencies. *A&A*570:A100, DOI 10.1051/0004-6361/201424522, 1408.0653
- Szewczyk O, Pietrzyński G, Gieren W, Ciechanowska A, Bresolin F, Kudritzki RP (2009) The Araucaria Project: The Distance to the Small Magellanic Cloud from Near-Infrared Photometry of RR Lyrae Variables. *AJ*138:1661–1666, DOI 10.1088/0004-6256/138/6/1661, 0910.3885
- Tabur V, Kiss LL, Bedding TR (2009) Hipparcos Calibration of the Tip of the Red Giant Branch. *ApJ*703:L72–L75, DOI 10.1088/0004-637X/703/1/L72, 0908.2873
- Tammann GA, Reindl B (2013) The luminosity of supernovae of type Ia from tip of the red-giant branch distances and the value of  $H_0$ . *A&A*549:A136, DOI 10.1051/0004-6361/201219671, 1208.5054
- Tammann GA, Sandage A, Reindl B (2008) Comparison of Distances from RR Lyrae Stars, the Tip of the Red Giant Branch, and Classical Cepheids. *ApJ*679:52–70, DOI 10.1086/529508, 0712.2346
- Thévenin F, Falanga M, Kuo CY, Pietrzyński G, Yamaguchi M (2017) Modern Geometric Methods of Distance Determination. *Space Sci. Rev.*212:1787–1815, DOI 10.1007/s11214-017-0418-9
- Thompson IB, Kaluzny J, Pych W, Burley G, Krzeminski W, Paczyński B, Persson SE, Preston GW (2001) Cluster AgeS Experiment: The Age and Distance of the Globular Cluster  $\omega$  Centauri Determined from Observations of the Eclipsing Binary OGLEGC 17. *AJ*121:3089–3099, DOI 10.1086/321084, astro-ph/0012493
- Thompson IB, Kaluzny J, Rucinski SM, Krzeminski W, Pych W, Dotter A, Burley GS (2010) The Cluster AgeS Experiment (CASE). IV. Analysis of the

- Eclipsing Binary V69 in the Globular Cluster 47 Tuc. *AJ*139:329–341, DOI 10.1088/0004-6256/139/2/329, 0910.4262
- Tikhonov NA, Galazutdinova OA (2002) Photometry of red giants in the disk of IC 1613. *A&A*394:33–38, DOI 10.1051/0004-6361:20021016
- Tolstoy E, Irwin MJ, Helmi A, Battaglia G, Jablonka P, Hill V, Venn KA, Shetrone MD, Letarte B, Cole AA, Primas F, Francois P, Arimoto N, Sadakane K, Kaufer A, Szeifert T, Abel T (2004) Two Distinct Ancient Components in the Sculptor Dwarf Spheroidal Galaxy: First Results from the Dwarf Abundances and Radial Velocities Team. *ApJ*617:L119–L122, DOI 10.1086/427388, [astro-ph/0411029](#)
- Trujillo I, Beasley MA, Borlaff A, Carrasco ER, Di Cintio A, Filho M, Monelli M, Montes M, Roman J, Ruiz-Lara T, Sanchez Almeida J, Valls-Gabaud D, Vazdekis A (2018) A distance of 13 Mpc resolves the claimed anomalies of the galaxy lacking dark matter. *ArXiv e-prints* 1806.10141
- Tully R (2011) The Geometry and Kinematics of the Local Volume. HST Proposal
- Tully RB, Courtois HM, Sorce JG (2016) Cosmicflows-3. *AJ*152:50, DOI 10.3847/0004-6256/152/2/50, 1605.01765
- Udalski A, Wyrzykowski L, Pietrzynski G, Szezyk O, Szymanski M, Kubiak M, Soszynski I, Zebrun K (2001) The Optical Gravitational Lensing Experiment. Cepheids in the Galaxy IC1613: No Dependence of the Period-Luminosity Relation on Metallicity. *Acta Astron.*51:221–245, [astro-ph/0109446](#)
- Uppgren AR (1985) Trigonometric parallaxes and their calibration. In: Hayes DS, Pasinetti LE, Philip AGD (eds) *Calibration of Fundamental Stellar Quantities*, IAU Symposium, vol 111, pp 31–49
- Valenti E, Ferraro FR, Origlia L (2004) Red giant branch in near-infrared colour-magnitude diagrams - II. The luminosity of the bump and the tip. *MNRAS*354:815–820, DOI 10.1111/j.1365-2966.2004.08249.x, [astro-ph/0404403](#)
- van Albada TS, Baker N (1971) On the Masses, Luminosities, and Compositions of Horizontal-Branch Stars. *ApJ*169:311, DOI 10.1086/151144
- van Albada TS, Baker N (1973) On the Two Oosterhoff Groups of Globular Clusters. *ApJ*185:477–498, DOI 10.1086/152434
- van Altena WF (1983) Astrometry. *ARA&A*21:131–164, DOI 10.1146/annurev.aa.21.090183.001023
- van den Bergh S (1975) *The Extragalactic Distance Scale*, the University of Chicago Press, p 509
- van Dokkum P, Danieli S, Cohen Y, Conroy C (2018a) The Distance of the Dark Matter Deficient Galaxy NGC1052-DF2. *ArXiv e-prints* 1807.06025
- van Dokkum P, Danieli S, Cohen Y, Merritt A, Romanowsky AJ, Abraham R, Brodie J, Conroy C, Lokhorst D, Mowla L, O’Sullivan E, Zhang J (2018b) A galaxy lacking dark matter. *Nature*555:629–632, DOI 10.1038/nature25767, 1803.10237
- van Leeuwen F (ed) (2007) *Hipparcos, the New Reduction of the Raw Data*, Astrophysics and Space Science Library, vol 350, DOI 10.1007/978-1-4020-6342-8
- Vasilevskis S (1966) The Accuracy of Trigonometric Parallaxes of Stars. *ARA&A*4:57, DOI 10.1146/annurev.aa.04.090166.000421
- Vilardell F, Ribas I, Jordi C, Fitzpatrick EL, Guinan EF (2010) The distance to the Andromeda galaxy from eclipsing binaries. *A&A*509:A70, DOI 10.1051/0004-6361/200913299, 0911.3391
- Walker AR (1998) CCD Photometry of Galactic Globular Clusters. IV. The NGC 1851 RR Lyrae Variables. *AJ*116:220–236, DOI 10.1086/300432, [astro-ph/](#)

9804339

- Walker MG, Mateo M, Olszewski EW, Gnedin OY, Wang X, Sen B, Woodroffe M (2007) Velocity Dispersion Profiles of Seven Dwarf Spheroidal Galaxies. *ApJ*667:L53–L56, DOI 10.1086/521998, 0708.0010
- Walker MG, Mateo M, Olszewski EW, Sen B, Woodroffe M (2009) Clean Kinematic Samples in Dwarf Spheroidals: An Algorithm for Evaluating Membership and Estimating Distribution Parameters When Contamination is Present. *AJ*137:3109–3138, DOI 10.1088/0004-6256/137/2/3109, 0811.1990
- Wallerstein G (1970) On the Incidence of Cepheids in Globular Clusters. *ApJ*160:345, DOI 10.1086/150434
- Wallerstein G (2002) The Cepheids of Population II and Related Stars. *PASP*114:689–699, DOI 10.1086/341698
- Wallerstein G, Cox AN (1984) The Population II Cepheids. *PASP*96:677–691, DOI 10.1086/131406
- Welch DL (2012) Type 2 Cepheids in the Milky Way Galaxy and the Magellanic Clouds. *Journal of the American Association of Variable Star Observers (JAAVSO)* 40:492
- Welch DL, Stetson PB (1993) Robust variable star detection techniques suitable for automated searches - New results for NGC 1866. *AJ*105:1813–1821, DOI 10.1086/116556
- Wesselink AJ (1946) The colour index of a black body with infinite temperature. *Bull. Astron. Inst. Netherlands*10:99
- Wesselink AJ (1969) Surface brightnesses in the U, B, V system with applications of  $M_v$  and dimensions of stars. *MNRAS*144:297, DOI 10.1093/mnras/144.3.297
- Worthey G, Lee Hc (2011) An Empirical UBV RI JHK Color-Temperature Calibration for Stars. *ApJS*193:1, DOI 10.1088/0067-0049/193/1/1, astro-ph/0604590
- Wu PF, Tully RB, Rizzi L, Dolphin AE, Jacobs BA, Karachentsev ID (2014) Infrared Tip of the Red Giant Branch and Distances to the Maffei/IC 342 Group. *AJ*148:7, DOI 10.1088/0004-6256/148/1/7, 1404.2987
- Zaritsky D, Harris J, Thompson IB, Grebel EK, Massey P (2002) The Magellanic Clouds Photometric Survey: The Small Magellanic Cloud Stellar Catalog and Extinction Map. *AJ*123:855–872, DOI 10.1086/338437, astro-ph/0110665
- Zaritsky D, Harris J, Thompson IB, Grebel EK (2004) The Magellanic Clouds Photometric Survey: The Large Magellanic Cloud Stellar Catalog and Extinction Map. *AJ*128:1606–1614, DOI 10.1086/423910, astro-ph/0407006
- Zhao G, Zhao YH, Chu YQ, Jing YP, Deng LC (2012) LAMOST spectral survey: An overview. *Research in Astronomy and Astrophysics* 12:723–734, DOI 10.1088/1674-4527/12/7/002
- Zhevakin SA (1959) On the Pulsational Theory of Stellar Variability. VI. (A Unified Interpretation of Various Types of Variability). *Soviet Ast.*3:913
- Zinn R, West MJ (1984) The globular cluster system of the galaxy. III - Measurements of radial velocity and metallicity for 60 clusters and a compilation of metallicities for 121 clusters. *ApJS*55:45–66, DOI 10.1086/190947
- Zsoldos E (1998) No RV Tauri Stars in Globular Clusters? *Acta Astron.*48:775–788